# THE ABSOLUTE DOSIMETRY OF NEGATIVE PIONS

by

KENNETH ROBERT SHORTT

B.Sc., McMaster University, 1970

M.Sc., The University of Western Ontario, 1972

A THESIS SUBMITTED IN PARTIAL FULFILMENT OF

THE REQUIREMENTS FOR THE DEGREE OF

DOCTOR OF PHILOSOPHY

in

THE FACULTY OF GRADUATE STUDIES

(Department of Physics)

We accept this thesis as conforming

to the required standard

THE UNIVERSITY OF BRITISH COLUMBIA

November 1979

© Kenneth Robert Shortt, 1979

In presenting this thesis in partial fulfilment of the requirements for an advanced degree at the University of British Columbia, I agree that the Library shall make it freely available for reference and study. I further agree that permission for extensive copying of this thesis for scholarly purposes may be granted by the Head of my Department or by his representatives. It is understood that copying or publication of this thesis for financial gain shall not be allowed without my written permission.

Department of Physics

The University of British Columbia
2075 Wesbrook Place
Vancouver, Canada
V6T 1W5

Date October 22, 1979

E-6 BP 75-511E

## ABSTRACT

### THE ABSOLUTE DOSIMETRY OF NEGATIVE PIONS

Soon three centres will be treating cancer with beams of negative pions: LAMPF, Los Alamos, U.S.A.; SIN, Villigen, Switzerland; and TRIUMF, Vancouver, Canada. In order to understand this new modality, it will be necessary to compare the results of pion therapy to those achieved with conventional means and to compare results among the three centres. Absolute dosimetry is the basis of this comparison.

An absolute dose determination has been made for the negative pion beam at TRIUMF using an ionization chamber. The relationship required to convert the ionization per unit mass, J/M, measured by the chamber to dose in tissue is

$$D = \frac{J}{M} \quad W \quad r \quad F$$

where W, r and F are calculated quantities.

W is the average energy expended in the gas per ion pair produced. Since the W-value for a secondary liberated during pion capture depends upon its energy, it was necessary to average over the energy spectra for the various secondaries.

r is the ratio of dose in the wall material, carbon, to dose in the gas, either methane or carbon dioxide. Since the pion secondaries have ranges which are of the same size as the cavity of the ion chamber, it was necessary to explicitly consider those secondaries which emerge from the

wall with insufficient energy to cross the cavity and those pions which form stars inside the cavity. Thus, r was found to be pressure dependent. The pressure dependence for carbon dioxide arises as follows:- as the pressure is increased, there are more pion captures in the gas, but since there is less energy released to charged secondaries per pion capture on oxygen than carbon, the dose in the gas decreases. Therefore, the calculation predicted that, as pressure is increased, J/M would remain unchanged for methane, but would decrease rather dramatically for carbon dioxide.

F is the ratio of dose in tissue to dose in wall material, carbon in this case. F is the product of two factors: P, which accounts for the difference in the stopping pion density for tissue compared to carbon, and K, which accounts for the difference in energy released per pion capture in tissue compared to carbon.

Experimentally, the ionization per unit mass was measured in a parallel plate chamber as a function of pressure for various gases with carbon, aluminum and TE-A150 electrodes. The pressure dependence of J/M measured for methane and carbon dioxide with carbon electrodes was compared to the behavior predicted by the calculation. Qualitatively, the prediction was confirmed: the ionization per unit mass for $CO_2$ decreases more dramatically with increased pressure than for $CH_4$. Therefore pion capture in the gas is significant and the energy released to charged secondaries per pion capture on oxygen is less than for carbon. Quantitatively, the percentage change is larger than predicted.

The value of J/M extrapolated to zero pressure and the appropriate values calculated for W and r enabled a determination of the absolute dose in carbon with an estimated accuracy of ± 5%. The ionization created with

aluminum electrodes was compared to that for carbon in order to estimate the dose in aluminum. After considering the dose contribution from beam contaminants, the value of F required to convert dose in carbon to dose in tissue was estimated to be 0.93 ± 0.05. Therefore, the absolute dose in tissue was determined to an accuracy of ± 7%. In order to increase the accuracy, it is necessary to improve the data available as input to the calculation.

TABLE OF CONTENTS

Page

ABSTRACT . . . . . ii

TABLE OF CONTENTS . . . . . v

LIST OF TABLES . . . . . viii

LIST OF FIGURES . . . . . x

ACKNOWLEDGEMENT . . . . . xiii

CHAPTER 1 INTRODUCTION . . . . . 1

1.1 PION RADIOTHERAPY . . . . . 1

1.1.1 Goal of Radiotherapy . . . . . 1

1.1.2 The Advantages of Pion Therapy . . . . . 3

1.2 PION DOSIMETRY . . . . . 10

1.2.1 Significance of Absolute Dosimetry . . . . . 10

1.2.2 Ionization Chamber Dosimetry . . . . . 12

1.2.3 The Approach to Absolute Pion Dosimetry . . . . . 16

CHAPTER 2 CALCULATION . . . . . 17

2.1 INTRODUCTION . . . . . 17

2.2 THEORY . . . . . 19

2.3 INPUT DATA . . . . . 25

2.3.1 Pion Star Data . . . . . 25

2.3.1.1 Secondary spectra for carbon and oxygen . . . 25

2.3.1.2 Fermi-Teller Z-law . . . . . 33

2.3.1.3 Pion Stopping Density . . . . . 35

TABLE OF CONTENTS (Cont'd)

Page

2.3.2 Stopping Power Data . . . . . 38

2.3.2.1 Stopping power for H and He ions in the elements H, C and O . . . . . 38

2.3.2.2 Bragg additivity rule . . . . . 44

2.3.2.3 Stopping power for lithium . . . . . 53

2.3.3 W-Value Data . . . . . 61

2.4 RESULTS OF THE CALCULATION . . . . . 65

2.4.1 Partitioning of the Dose Between the Various Event Types . . . . . 65

2.4.2 W and r for $CH_4$ and $CO_2$ in Carbon Walls . . . . . 69

2.5 DOSE DEPOSITED BY OTHER PARTICLES . . . . . 75

2.5.1 Electrons and Muons . . . . . 75

2.5.2 Directly Ionizing Pions . . . . . 77

2.5.3 Neutrons and Gamma-Rays . . . . . 79

2.6 SUMMARY . . . . . 80

CHAPTER 3 EXPERIMENT . . . . . 81

3.1 INTRODUCTION . . . . . 81

3.2 APPARATUS . . . . . 82

3.2.1 Beam Delivery System . . . . . 82

3.2.2 Beam Tune and Dose Profiles . . . . . 82

3.2.3 Monitor Chamber . . . . . 89

3.2.3.1 Construction . . . . . 90

3.2.3.2 Operation . . . . . 92

3.2.3.3 Calibration versus particle flux . . . . . 93

TABLE OF CONTENTS (Cont'd)

Page

3.2.4 Parallel Plate Ionization Chamber . . . . . 96

3.2.4.1 Construction . . . . . 96

3.2.4.2 Gas delivery system . . . . . 100

3.2.4.3 Temperature monitor . . . . . 102

3.2.5 Electronics . . . . . 103

3.3 RESULTS . . . . . 106

3.3.1 Saturation Characteristics . . . . . 106

3.3.1.1 Theoretical . . . . . 106

3.3.1.2 Experimental . . . . . 108

3.3.2 Polarity Effect . . . . . 113

3.3.3 J/M Versus Pressure . . . . . 115

3.4 DISCUSSION . . . . . 127

3.4.1 Comparison Between Calculation and Experiment . . . . 127

3.4.2 Absolute Dose in Carbon . . . . . 133

3.4.3 Kerma Factor . . . . . 139

CHAPTER 4 CONCLUSION . . . . . 149

REFERENCES . . . . . 152

APPENDIX A A CHARGE COLLECTOR TO DETERMINE THE STOPPING DISTRIBUTION OF A PION BEAM . . . . . 162

APPENDIX B DEFINITIONS, EQUATIONS AND CONSISTENCY CHECKS . . . . . 166

APPENDIX C OXYGEN SPECTRA EXTRACTION . . . . . 169

APPENDIX D STERNHEIMER DENSITY CORRECTION FOR ELECTRON STOPPING POWERS . . . . . 171

BIOGRAPHICAL INFORMATION

# LIST OF TABLES


| Table | | Page |
|---|---|---|
| 1.1 | Improved Survival When Treated with Megavoltage Radiotherapy | 2 |
| 2.1 | Particle and Energy Balance Sheet for Carbon | 30 |
| 2.2 | Particle and Energy Balance Sheet for Oxygen | 31 |
| 2.3 | Comparison of Carbon and Oxygen Energy Distributions | 32 |
| 2.4 | Constants Used in the Dennis Formula for W-Values | 62 |
| 2.5 | Average Energy and Kerma According to Particle Type (Carbon) | 66 |
| 2.6 | Values of W and r for C-$CH_4$ (sphere) | 69 |
| 2.7 | Values of W and r for C-$CO_2$ (sphere) | 71 |
| 3.1 | Percentage of the Dose by Particle Type | 89 |
| 3.2 | Electrode Materials and Configuration | 99 |
| 3.3 | Gas Density and Purity | 102 |
| 3.4 | Lineal Energy at Various Depths | 113 |
| 3.5 | J/M Extrapolated to Zero Pressure for Carbon Electrodes | 134 |
| 3.6 | Values Required to Calculate the Dose for $CH_4$ | 135 |
| 3.7 | Values Required to Calculate the Dose for $CO_2$ | 135 |
| 3.8 | Dose in Carbon | 136 |
| 3.9 | Evaluation of $\overline{\frac{W}{W_\beta} \times r}$ for Carbon Electrodes | 138 |
| 3.10 | J/M Extrapolated to Zero Pressure for Aluminum Electrodes | 139 |
| 3.11 | Evaluation of $\overline{\frac{W}{W_\beta} \times r}$ for Aluminum Electrodes | 144 |
| 3.12 | J/M Extrapolated to Zero Pressure for TE-A150 Electrodes | 146 |

LIST OF TABLES (Cont'd)


| Table | | Page |
|---|---|---|
| 4.1 | Dose in Carbon and Aluminum . . . . . | 150 |
| B.1 | Checks of Internal Consistency . . . . . | 168 |
| D.1 | Parameters Required to Calculate the Density Correction . . . | 172 |
| D.2 | Electron Stopping Powers . . . . . | 173 |

# LIST OF FIGURES


| Figure | | Page |
|---|---|---|
| 1.1 | Dependence of RBE and OER upon LET | 6 |
| 1.2 | Comparison of Depth Dose Curves for $\gamma$-Rays and Pions | 8 |
| 1.3 | Superposition of Parallel Opposing Fields for $\gamma$-Rays and Pions | 9 |
| 2.1 | Secondary Spectra for Pion Absorption on Carbon | 27 |
| 2.2 | Secondary Spectra for Pion Absorption on Oxygen | 28 |
| 2.3 | Range Ratio for Carbon/Methane and Carbon/Carbon Dioxide | 37 |
| 2.4 | Stopping Cross Section for Protons in Carbon | 40 |
| 2.5 | Stopping Cross Section for Alphas in Carbon | 42 |
| 2.6 | Stopping Cross Section for Protons in $CO_2$ | 46 |
| 2.7 | Stopping Cross Section for Protons in $CH_4$ | 48 |
| 2.8 | Stopping Cross Section for Alphas in $CO_2$ | 50 |
| 2.9 | Stopping Cross Section for Alphas in $CH_4$ | 52 |
| 2.10 | Square of the Effective Charge for Lithium Ions | 54 |
| 2.11 | Stopping Cross Section for Li Ions in Carbon | 56 |
| 2.12 | Stopping Cross Section for Li Ions in $CO_2$ | 58 |
| 2.13 | Stopping Cross Section for Li Ions in $CH_4$ | 60 |
| 2.14 | W-Value for Alpha Particles in $CH_4$ | 64 |
| 2.15 | Partitioning the Dose Among the Event Types for Li Ions | 67 |
| 2.16 | Partitioning the Dose Among the Event Types for All Secondaries | 68 |
| 2.17 | $\frac{W_\beta}{\bar{W}_g\ r}$ for C-$CH_4$ in the Parallel Plate Chamber | 73 |

LIST OF FIGURES (Cont'd)


| Figure | | Page |
|---|---|---|
| 2.18 | $\frac{W_\beta}{\overline{W}_g\ r}$ for C-$CO_2$ in the Parallel Plate Chamber | 74 |
| 2.19 | Electron Stopping Power Ratio Versus Pressure | 76 |
| 3.1 | Block Diagram of Apparatus | 83 |
| 3.2 | Ionization Versus Depth Profile | 84 |
| 3.3 | Cross Scans at the Peak | 86 |
| 3.4 | Dose by Particle Type | 87 |
| 3.5 | Schematic Diagram of the Monitor Chamber | 91 |
| 3.6 | Transmission Chamber Response Versus Momentum | 94 |
| 3.7 | Transmission Chamber Response Versus Separation | 95 |
| 3.8 | Parallel Plate Ionization Chamber Construction | 98 |
| 3.9 | Gas Delivery System | 101 |
| 3.10 | Timing Sequence for Reading the Electrometer | 104 |
| 3.11 | Saturation Curves for Carbon Dioxide | 109 |
| 3.12 | k Versus Mass Curves at Different Depths for Methane | 110 |
| 3.13 | k Versus Mass at the Peak | 111 |
| 3.14 | k Versus Mass at the Plateau | 112 |
| 3.15 | Polarity Difference Versus Mass | 114 |
| 3.16 | J/M Versus Pressure for Methane | 116 |
| 3.17 | J/M Versus Pressure for Carbon Dioxide | 117 |
| 3.18 | J/M Versus Pressure for All the Gases at the Peak with Carbon Electrodes | 118 |
| 3.19 | J/M Versus Pressure for All the Gases at the Plateau with Carbon Electrodes | 119 |
| 3.20 | Peak to Plateau Ratio Versus Pressure with Carbon Electrodes | 122 |

LIST OF FIGURES (Cont'd)


| Figure | | Page |
|---|---|---|
| 3.21 | J/M Versus Pressure for All the Gases at the Peak with Aluminum Electrodes | 123 |
| 3.22 | J/M Versus Pressure for All the Gases at the Plateau with Aluminum Electrodes | 124 |
| 3.23 | Peak to Plateau Ratio Versus Pressure with Aluminum Electrodes | 125 |
| 3.24 | J/M Versus Pressure for Air and TE gas with TE-A150 Electrodes | 126 |
| 3.25 | Factor U(P) Versus Pressure | 129 |
| 3.26 | Comparison of Calculated and Observed Pressure Dependence for J/M | 131 |

# ACKNOWLEDGEMENTS

I am indebted to Dr. Mark Henkelman, my thesis supervisor, for his advice and encouragement throughout this investigation. I am thankful to other members of the Biophysics staff: Dr. Gabriel Lam for helpful suggestions concerning the experiment and careful reading of this thesis; Dr. Jan Nordin for thought-provoking conversations; Mr. Bob Harrison for writing the data acquisition programs; Mr. Bruno Jaggi for maintaining the channel and electronics. I am also grateful for the help provided by each staff member with the data acquisition. I enjoyed the comradeship of fellow graduate students Larry Watts, Michael Poon and Juliet Brosing. I am grateful to Pat Bell for carefully typing this manuscript. During this work, I greatly appreciated the moral and spiritual support of members of the group.

I acknowledge with thanks the recommendations of my advisory committee: Dr. J. Warren, Dr. L.D. Skarsgard, Dr. R.O. Kornelsen, Dr. R.R. Johnson and Dr. G. Hoffmann, who took the place of Dr. Johnson while he was on sabbatical leave.

I am grateful to Dr. H. Bichsel for initially pointing out to me the shortcomings of Bragg-Gray cavity theory and to his graduate student, Ms. A. Rubach, for giving me a copy of the fortran code which she used to perform calculations for neutron beams similar to those I have done for pion beams. I am also grateful to Dr. W. Kluge for providing me with the charged particle spectra due to pion capture in oxygen containing compounds

before publication.

The financial support of the National Cancer Institute and the research facility provided by the B.C. Cancer Foundation are gratefully acknowledged.

Special thanks are due to my wife, Marilyn, whose love and faith supported me, and to our daughter, Rebecca, who brought me great happiness. I am grateful to my parents, who provided my personality with enough determination to carry this work through to completion.

# CHAPTER 1

# INTRODUCTION

## 1.1 PION RADIOTHERAPY

The use of pions for the treatment of cancer was first proposed by Fowler (1) in 1961 and is currently under development as a clinical experiment at three centres: TRIUMF, Vancouver, Canada; LAMPF, Los Alamos, U.S.A.; and SIN, Villigen, Switzerland. It is anticipated that this new modality will make a significant impact on the cure of deep seated malignancies. However, pion radiotherapy is considerably more complex than photon radiotherapy in the production of the radiation, its delivery, and its characterization. Therefore, if this new modality is to be clinically successful, pion physical dosimetry must be understood. This thesis explores and solves many of the problems of pion dosimetry. In order to appreciate these problems, it is necessary first to understand the goals of radiotherapy and to see how pions are particularly suited to meet these goals.

### 1.1.1 Goal of Radiotherapy

It is the goal of radiotherapy to obtain local control of cancer in order to cure or palliate the patient. The efforts to attain this goal are frustrated by those tumours which have cells with peculiar radiobiologic characteristics (such as radioresistance induced by hypoxia)

or which are located at sites involving critical normal tissues (whose low radiation tolerance would lead to unacceptable radiation complications). It is expected that the ability to achieve uncomplicated local control of cancer would be improved if it were possible to increase the effective tumour dose while maintaining or reducing the effective dose to the surrounding normal tissues. This expectation is based on the dramatic increase in five year survival observed between 1955 and 1970 which has been attributed, at least in part, to the improved physical depth dose characteristics of megavoltage X-rays compared to kilovoltage X-rays (2) (see table 1.1). The physical properties of negative pions will result in further improvements in both the physical and the biologically effective dose distribution.

Table 1.1: Improved Survival When Treated with Megavoltage Radiotherapy (2)

| Type or Site of Cancer | % 5-Year Survival with Kilovoltage X-Rays (1955) | % 5-Year Survival with Megavoltage X-Rays (1970) |
|---|---|---|
| Bladder | 0 - 5 | 25 - 35 |
| Cervix | 35 - 45 | 55 - 65 |
| Embryonal Cancer of Testis | 20 - 25 | 55 - 70 |
| Hodgkin's Disease | 30 - 35 | 70 - 75 |
| Nasopharynx | 20 - 25 | 45 - 50 |
| Ovary | 15 - 20 | 50 - 60 |
| Prostate | 5 - 15 | 55 - 60 |
| Retinoblastoma | 30 - 40 | 80 - 85 |
| Seminoma of Testis | 65 - 70 | 90 - 95 |
| Tonsil | 25 - 30 | 40 - 50 |

### 1.1.2 The Advantages of Pion Therapy

In order to discuss the advantages of pion therapy, it is necessary to define terms used commonly to compare different radiation types. The quality of a radiation field is a descriptive term referring to those features of the spatial distribution of energy transfers that influence the effectiveness of the radiation. Beams of X-rays, $\gamma$-rays and electrons used routinely in radiotherapy are of the same low quality. On the other hand, pion beam quality is a function of location in the pion field. LET, linear energy transfer, is a physical parameter used to specify the beam quality. For a given particle, LET is the mean energy locally imparted by collisions with energy transfers less than some specified value, $\Delta$, divided by the distance traversed by the particle in making these transfers. If $\Delta$ is set to the maximum kinematically possible, then LET equals stopping power. RBE, relative biological effectiveness, of a particular radiation is the ratio of the dose of a reference radiation (280 keV X-rays) to the dose of the particular radiation (pions) required to attain the same effect on a given biological system. Radiation induced cell death is produced by a mechanism which is oxygen dependent. OER, oxygen enhancement ratio, is the ratio of the dose required to achieve a specified effect under anoxic conditions to the dose required to achieve the same effect under oxygenated conditions. RBE and OER are dependent upon LET as shown in figure 1.1. This dependence arises because of matching between the spatial distribution of ionization events and the cell structure.

To understand the advantages of pion therapy compared to $^{60}$Co $\gamma$-rays, consider the depth dose curves shown in figure 1.2. The $^{60}$Co curve exhibits skin-sparing in the build-up region where the dose rises from 60% right at the surface to 100% at 5 mm depth. Then the dose falls off exponentially

to 42% at 14 cm. The pion depth dose curve has three regions: the plateau, the peak and the tail.

In the plateau, the dose is deposited by passing high-speed particles: pions and the accompanying contaminants, muons and electrons. Pions emerging from the channel with the midline momentum of 180 MeV/c, will have a residual kinetic energy of 60 MeV in the plateau and a stopping power in water of 3 MeV-cm$^2$/g. Similarly, contaminant electrons and muons will be minimally ionizing projectiles. Except for the small dose deposited by pion in-flight nuclear interactions (4), the plateau is a region of low LET. Right at the surface (which is not shown in figure 1.2) there will be a build-up of knock-on electrons, but no significant skin-sparing build-up of dose (see appendix A or reference (5)). The plateau may be sloped depending on beam focusing.

There are two reasons for the increase in dose and mean LET observed in the peak. Firstly, as the pions slow down, the stopping power of the medium increases, producing a characteristic Bragg peak. This increase in dose is associated with an increase in LET. Secondly, when negative pions stop, they are captured by atomic nuclei with which they interact. This process is called pion star formation because of its appearance in cloud chambers. Of the 140 MeV pion rest mass, about 28 MeV (for Carbon capture) appears in the form of charged secondaries p, d, t, $^3$He, $^4$He, and Li, which increases the dose and the LET in the peak.

In the tail region most of the dose is due to contaminating electrons which have a residual kinetic energy of 50 MeV and a minimum stopping power (2 MeV-cm$^2$/g). This is low LET dose.

Consequently, the advantages of pion therapy are twofold. Firstly, the physical dose peak can be made to coincide with the tumour volume as

shown in figure 1.3 for the case of parallel opposed fields. Secondly, the average LET in the peak region is higher than in the plateau and this results in an increased RBE and decreased OER for the peak compared with the plateau (6). This provides the ability to increase the effective tumour dose while maintaining or reducing dose to the surrounding healthy tissue. Thus, local control of cancer with a minimum of treatment-induced side-effects ought to be achievable.

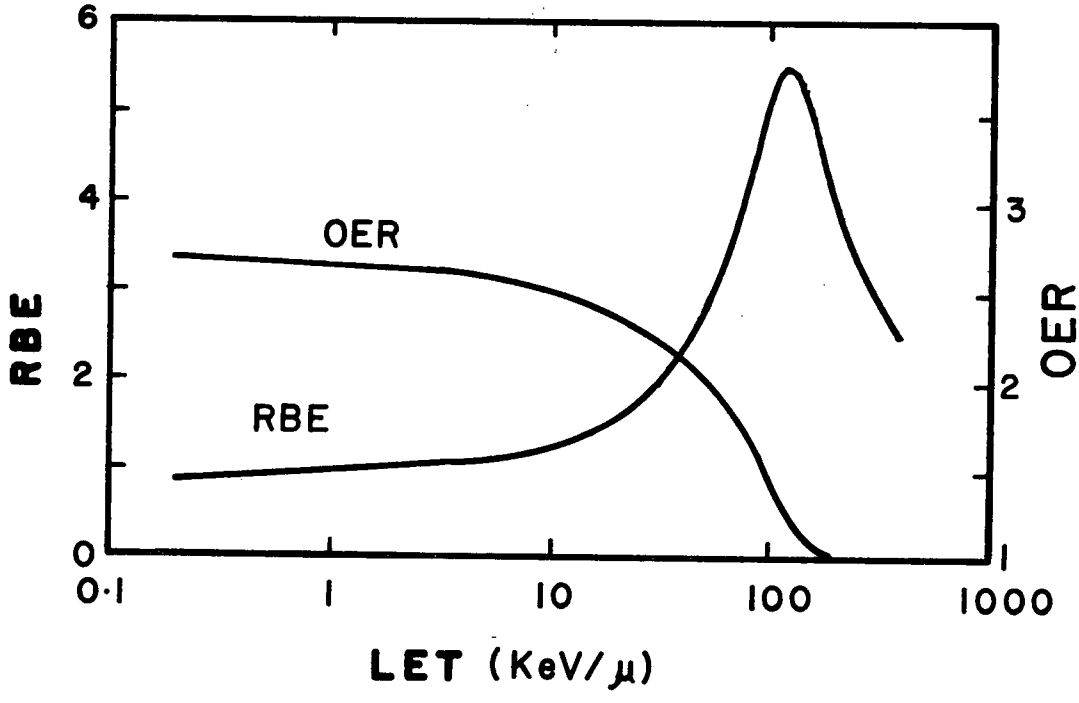


Figure 1.1: Dependence of RBE and OER upon LET

This curve is characteristic of various biological effects on cells. For more information, see reference (3).

Figure 1.2: Comparison of Depth Dose Curves for γ-Rays and Pions

The $^{60}Co$ γ-ray depth dose is for 10 x 10 cm field at 80 cm source to surface distance.

The pion depth dose was measured for a midline momentum of 180 MeV/c and 12 cm diameter at the 50% level.

The pion curve is shown with an 8 cm shift in order to simulate the treatment of a tumour at 14 cm depth (shown in figure 1.3).

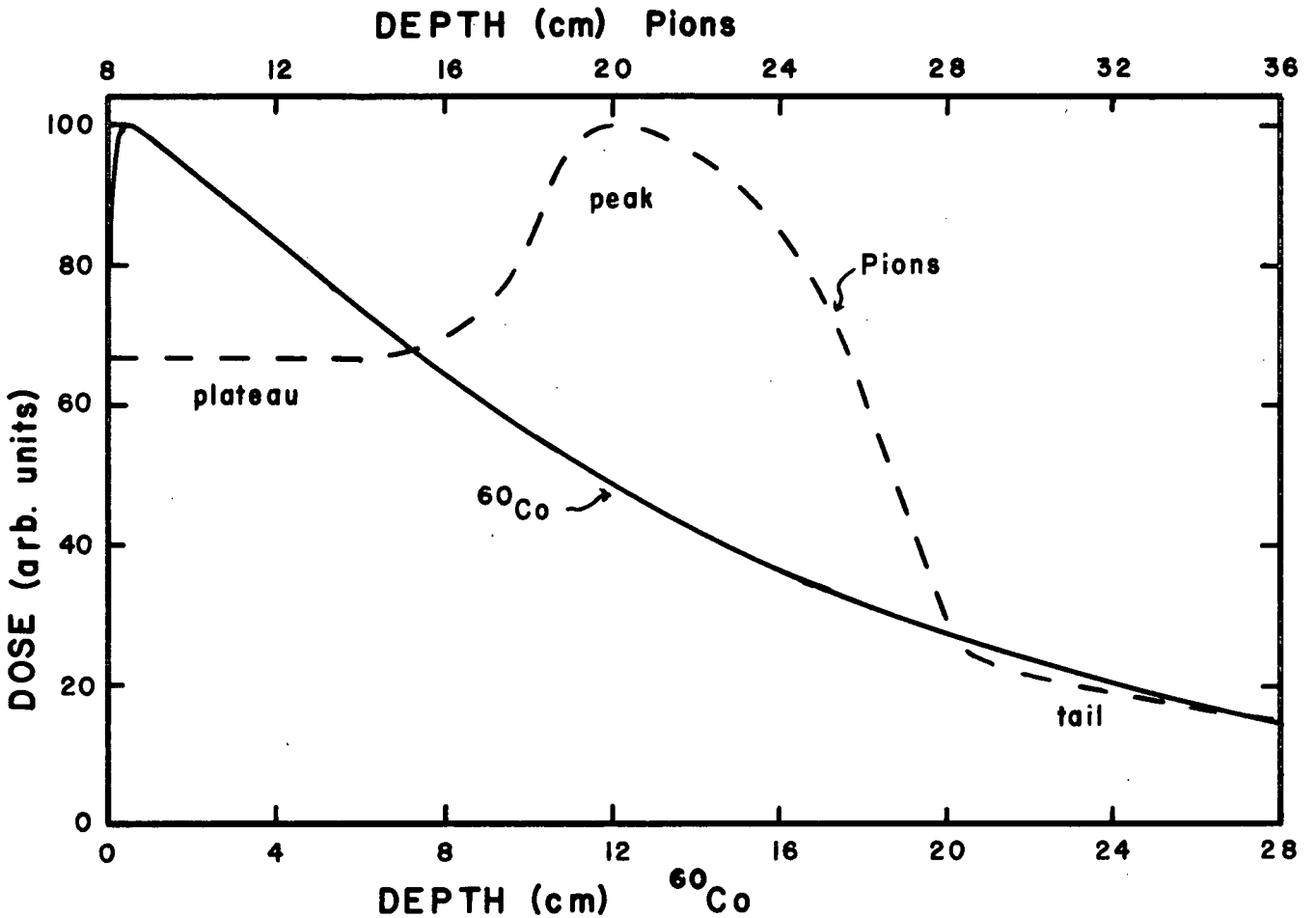
DEPTH (cm) Pions
8
12
16
20
24
28
32
36
100
80
60
40
20
0
DOSE (arb. units)
peak
Pions
plateau
60Co
tail
0
4
8
12
16
20
24
28
DEPTH (cm) 60Co

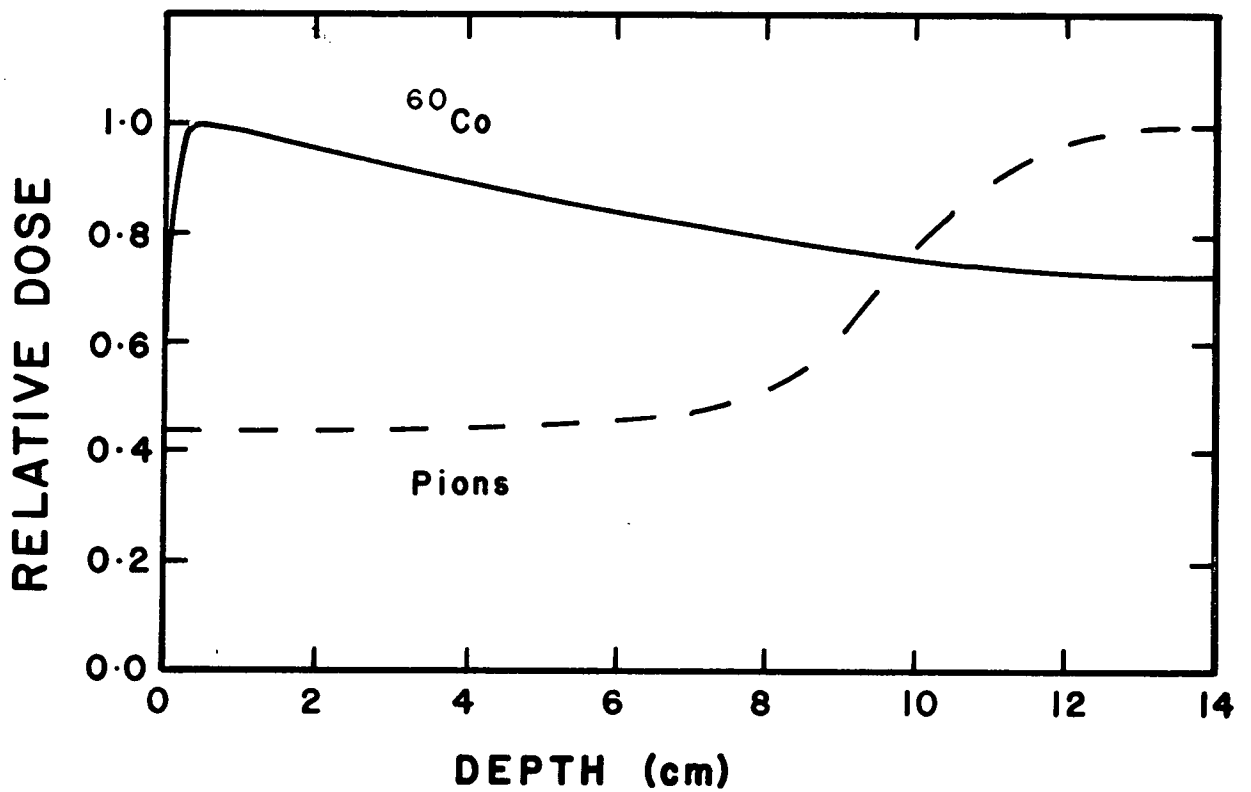


Figure 1.3: Superposition of Parallel Opposing Fields for γ-Rays and Pions

The tumour was taken to be at the midline of a uniform section 28 cm thick. The dose distribution is symmetric about the 14 cm depth.

## 1.2 PION DOSIMETRY

### 1.2.1 Significance of Absolute Dosimetry

It is the purpose of this project to investigate the absolute dosimetry of the biomedical negative pion beam at TRIUMF. Dose is defined as the quotient of the energy imparted by ionizing radiations to a volume element divided by the mass of the element. The measurement of dose involves a special type of limiting process, in that the mass must be small enough so that the measurement may be defined at a point, but large enough that the energy deposition is not caused by a few interactions with large statistical uncertainty. An absolute determination of dose requires the use of an instrument which can measure the energy imparted to the mass in its sensitive volume without the need for calibration in a known radiation field. The SI unit of absorbed dose is the Gray (Gy) = 1 J/kg. The unit used previously was the rad = .01 Gy.

An understanding of pion dosimetry contributes to the body of knowledge of physics, radiobiology and medicine. Relatively little was known about the physical dosimetry of pion beams and, therefore, a study of pion dosimetry was thought to be interesting and worthwhile for purely academic reasons. As well, this study has placed certain demands upon other disciplines of physics to improve the basic physical data required to carry out the necessary calculations.

From the point of view of biology, the ability to measure the dose forms the basis of RBE determinations according to

RBE = Dose with 280 keV x-rays / Dose with pions.

A failure to understand pion dosimetry will lead to misunderstanding the RBE.

From a strictly pragmatic point of view, a study of pion dosimetry is not essential to the initiation of treatment of patients with pions. As

discussed in the previous paragraph, the prediction of the effect of pions on patients will be based on biological systems whose response to pions will be compared with their response to conventional therapy. Errors in dosimetry will have reciprocal errors in RBE, but the product, effective dose, is invariant. Even in the long term, the success of pion therapy compared to conventional therapy will be based upon a clinical demonstration of the hoped for increase in survival for the same level of treatment-induced complications. On the other hand, it is necessary to understand pion therapy. Such an understanding involves comparisons between the clinical effects of pions and conventional radiation and between the clinical effects of the pion beams available at the different laboratories. A knowledge of pion dosimetry forms the basis of these comparisons, and is therefore essential to the understanding of pion therapy.

1.2.2 Ionization Chamber Dosimetry

In general, three methods are available for dosimetry: ionization chambers, chemical dosimeters and calorimeters. Due to the relatively low dose rate (<0.01 Gy/min), only ionization chamber measurements are practical.

The equation which relates ionization in the gas to dose deposited in the wall is:

$$D_{wall} = (J/M) \times \overline{W}g \times r \qquad 1.1$$

where J/M is the ionization per unit mass, $\overline{W}g$ is the average energy required to create an ion pair in the gas, and r is the quotient of dose in the wall divided by dose in the gas. In order to measure J/M, all of the ionization must be collected (that is, saturation must be achieved) and the mass of the gas must be determined. Calculation is required to determine the values for W and r. For a given projectile (for example, an alpha particle) the average energy required to create an ion pair in a particular gas is usually around 30 eV at high projectile velocities and it increases at low velocities. To determine the average W-value for the fraction of the dose due to stars, it is necessary to average over the energy spectrum of each secondary. Similarly, the calculation of r for the pion star dose also requires a detailed knowledge of the energy spectra for secondaries since the stopping power of a medium depends upon the projectile velocity.

The determination of the value for r requires the application of cavity chamber theory. There are different versions of cavity theory depending upon the underlying assumptions. Basic cavity theory (7) was developed by Bragg (8) and modified by Gray (9, 10). For the case of an infinitely small chamber, in Bragg-Gray theory, r is the stopping power ratio of the wall to the gas averaged over the spectrum of secondaries established in the wall. This theory has three assumptions: that primary interactions in the gas are negligible,

that the spectrum of secondaries established in the wall is not modified by the gas in the cavity, and that the primary interactions from which secondaries can enter the cavity is spatially uniform.

The last condition has been embodied into the definition of the special limiting process required when measuring dose by demanding that the mass be small enough that the dose be defined at a point. The first two conditions are not valid for large cavities, where large means a cavity whose size is comparable to the range of the secondaries which deposit dose in it. For such a large cavity, there will be significant pion capture in the gas. This modifies the total energy contained in the spectra of secondaries because the release of energy to charged secondaries due to pion capture in the gas will, in principle, be different from that due to pion capture in the wall. As well, the relative distribution of energies in the spectrum for a particular type of secondary is changed because the stopping power of the cavity differs in principle from that of the wall material. Thus, for large cavities the theory must explicitly consider interactions within the cavity as has been done for neutron irradiation (11, 12). A rough calculation based on the thesis of Henry (13) and the calculated secondary spectra of Guthrie (14) indicated that ion chambers in common use (1 to 2 $cm^3$) need to be considered as large compared to the range of the secondaries, and therefore such a detailed calculation of r is necessary.

If the primary radiation were gamma rays instead of pions, it would be possible to release the restriction on cavity size by selecting a chamber with an atomically matched gas-wall pair (for example, ethylene and polyethylene) to which Fano's theorem may be applied. This theorem states that in a medium of given composition exposed to a uniform flux of primary radiation, the flux of secondary radiation is uniform independent of the density of the medium and

independent of density variations from point to point, provided that the interactions of the primary radiation and the secondary radiation with the atoms of the medium are both independent of density. It is a corollary of Fano's theorem that for a cavity with atomically matched gas and wall, the stopping power ratio is unity independent of size and pressure if the stopping power is independent of density. Unfortunately, in the pion case, the stopping power for the pion secondaries depends upon the density of the stopping medium at energies within the range of interest. This fact has been documented in a recent survey by Thwaites (15) and is discussed further in section 2.3.2.1. Therefore, the atomically matched system employing ethylene and polyethylene would not have the value unity for r. The system employing methane-based TE gas and TE-A150 plastic is not atomically matched since the gas and wall have different ratios of carbon to oxygen atoms, and therefore it will not have the value unity for r. (TE-A150 plastic is not tissue equivalent for the same reason.) For pions, there is no matched gas-wall pair presently available to which Fano's theorem may be applied. Therefore the restriction on cavity size imposed by the simple Bragg-Gray theory cannot be circumvented. Since the range of the pion secondaries is small compared to the cavity size, the type of cavity theory due to Casewell (16), which explicitly considers interactions within the cavity, is necessary.

If the dose in tissue is required, a further step is required:

$$D_{tissue} = F\, D_{wall} \qquad 1.2$$

where F is loosely called the kerma factor. Kerma is the quotient of the sum of the initial kinetic energies of all the charged particles liberated by indirectly ionizing particles in a volume element divided by the mass of the matter in that element. The pion is a directly ionizing particle while in flight because it is charged and of sufficient energy to produce ionization

by collision. The pion is indirectly ionizing when captured because its interaction with the nucleus is due to the strong force, independent of the pion charge. The kerma factor is the ratio of the dose deposited in a small element of tissue located in a block of tissue divided by the dose deposited in a small element of wall material located in a block of wall material when both blocks are exposed to the same fluence of pions. For the pion star dose, F is composed of two parts:

$$F = K \times P \qquad 1.3$$

where K corrects for the difference in energy released to charged secondaries by capture in tissue compared to wall by virtue of their differing atomic composition, and P corrects for the difference in density of pion stops in tissue compared to wall by virtue of their differing stopping powers. Further comments concerning the factor K will be reserved for the discussion in chapter 3. The importance of the factor P will be dealt with in section 2.3.1.3.

### 1.2.3 The Approach to Absolute Pion Dosimetry

The absolute dosimetry of a negative pion beam was investigated by means of an ionization chamber. Appropriate values of $\bar{W}$ and r for two gas-wall combinations (methane and carbon dioxide with carbon electrodes) were calculated for the pion star dose as a function of chamber pressure using the Casewell type of cavity theory, which explicitly considers primary interactions in the gas and perturbation of the secondary spectra by the gas. $\bar{W}$ and r were shown to be pressure dependent, invalidating simple Bragg-Gray cavity theory. Values of J/M were measured for several gas-wall combinations as a function of gas pressure. Measurements in both the peak and plateau have permitted the extraction of the pressure dependence of effects specific to pion stars for comparison with the calculation. The calculation and experiment agree qualitatively, but the observed dependence of J/M on pressure is more dramatic than predicted, particularly for oxygen bearing gases.

The experimental value of J/M extrapolated to zero pressure was used with the calculated values of W and r in equation 1.1 to determine the dose in carbon. The ratio of ionization produced with aluminum and carbon electrodes permitted an evaluation of the dose in aluminum. The problem of converting dose in carbon to dose in tissue is discussed and the conversion factor is evaluated.

# CHAPTER 2

# CALCULATION

## 2.1 INTRODUCTION

A calculation was performed to determine the average energy expended per ionization, $\overline{W}_g$, in a gas cavity, and to determine the ratio, r, of the energy deposited in the gas cavity to the energy that would have been deposited if the cavity had been filled with wall material. The calculation was restricted to the dose deposited by pion stars since this is the part of the radiation field that is uniquely characteristic of pions and was poorly understood. The dose deposited by passing pions and electrons is better understood, and is specific to the contamination of the particular pion beam and to the position in the radiation field.

A calculation of this type was first performed by Casewell (16) in 1964 for neutron dosimetry and has been used by several other investigators to study neutrons (11, 12, 17). The calculation evaluates the energy deposited in a gas filled cavity by all the charged particles interacting in the cavity. It assumes that the particles travel in straight lines and lose energy continuously and locally. That is, the effects of multiple scattering, range straggling and energetic delta rays were not considered. Along with the energy deposited in the gas, the calculation evaluates the ionization produced by each particle from a knowledge of the W-values for those particles. This allows the

determination of the average energy expended per ionization, $\overline{W}_g$, to be made. The calculation is then repeated for the cavity filled with an equivalent mass of wall material instead of gas. The energy deposited in the wall material is evaluated in the same way as in the case of the gas filling, and the ratio , r, of the energy in the wall to the energy in the gas is computed.

The ratio r was calculated for the dose from pion stars as a function of the pressure of the gas in the cavity, or equivalently as a function of the mass of the gas. This calculation is dependent only on the areal density of the material filling the cavity and therefore cannot distinguish between cavities of increased volume and cavities with increased pressure.

## 2.2 THEORY

Consider a cavity inside an infinite homogeneous phantom (of physical density $\rho$) which is filled uniformly with stopped pions of density $\Pi$ pions/g. Let the initial energy spectrum per pion for a particular type of secondary particle be $K(\varepsilon)$ secondaries/MeV-pion. Then, the energy spectrum per gram for this secondary particle is given by

$$Np(\varepsilon) = \Pi K(\varepsilon) \quad \text{secondaries/MeV-g} \qquad 2.1$$

where p refers to the initial or production spectrum. Eventually, a summation over particle type is performed.

Consider a surface element located on the cavity boundary represented by $\bar{dA}$, its unit normal pointing into the cavity. $\bar{L}$ is a vector pointing from a unit volume located in the wall to the area $\bar{dA}$. $\theta$ is the angle between $\bar{dA}$ and $\bar{L}$ and $\phi$ is the azimuthal angle. The number of secondaries with energy between $\varepsilon$ and $\varepsilon + d\varepsilon$ produced inside a volume element dV located at $-\bar{L}$ is given by

$$Np(\varepsilon)\, d\varepsilon\, \rho dV = Np(\varepsilon)\, d\varepsilon\, \rho L^2 \sin\theta dL d\theta d\phi \qquad 2.2$$

Since the production of secondaries is isotropic, the fraction of the secondaries originating in dV travelling in direction $\bar{L}$ which enter dA (if they have sufficient energy to travel distance L) is $\frac{dA}{4\pi L^2}\cos\theta$. A secondary of residual energy E at the boundary could have started with energy $\varepsilon_1$ at $L_1$ or $\varepsilon_2$ at $L_2$ and so on. That is, the value of $\varepsilon$ depends on L for a given E. The total number of secondaries crossing the area with energy E will involve an integral over L in expression 2.2. This integral over L can be converted to an integral over $\varepsilon$ by first considering that

$$\rho dL = \frac{dE}{S(E)} \qquad 2.3$$

That is, for an increase in path length $\rho dL$, there will be a change in the

energy of that particle when it crosses dA of

$$dE = S(E)\,\rho dL \qquad 2.4$$

It is important to note that this relationship is true independent of the initial energy of the particle $\varepsilon$. Therefore, the number of particles crossing $\bar{dA}$ with energy between E and E + dE in direction $\bar{L}$ is given by

$$\frac{dE}{S(E)} \int_{\varepsilon=E}^{\varepsilon_m} Np(\varepsilon)\, d\varepsilon \; \frac{\sin\theta\cos\theta}{4\pi} \; d\theta\, d\phi\, dA \qquad 2.5$$

For convenience of notation, the equilibrium or slowing-down spectrum is defined as

$$Nr(E) = \frac{1}{S(E)} \int_{\varepsilon=E}^{\varepsilon_m} Np(\varepsilon)\, d\varepsilon \qquad 2.6$$

with units secondaries/MeV-$cm^2$. Then the total number of secondaries of energy between E and E + dE, crossing dA and travelling in direction L is

$$Nr(E)\, dE \; \frac{\sin\theta\cos\theta}{4\pi} \; d\theta\, d\phi\, dA \qquad 2.7$$

Let $\Delta$ be the energy deposited in the cavity by such a secondary. Generally, $\Delta$ depends upon E, cavity geometry and stopping power of the cavity material. The total energy deposited in the cavity is given by integrals over $\phi$, dA, $\theta$ and E. The integrals are considerably simplified if the cavity is assumed to be a sphere of diameter D. In this case, integrations over dA and $\phi$ can be performed to yield

$$\text{Energy} = \frac{\pi}{2} D^2 \int_{E=0}^{\varepsilon_{max}} \int_{\theta=0}^{\frac{\pi}{2}} Nr(E)\, \Delta(\theta, E) \sin\theta \cos\theta\, d\theta\, dE \qquad 2.8$$

The integral over $\theta$ runs from 0 to $\pi/2$ rather than $-\pi/2$ to $\pi/2$ to exclude particles crossing dA from inside the spherical cavity. These particles will be considered separately.

For stoppers (secondaries from the wall which stop in the cavity) $E_{max}$ is given implicitly by $R(E_{max}) = D$ where R is the range in the cavity. Also $\Delta \equiv E$ and $D\cos\theta > R(E)$. The lower bound on $\cos\theta$ sets an upper bound on $\theta$: $\theta_{max} = \cos^{-1} R(E)/D$. Then integration yields

$$E_{stopper} = \frac{\pi}{4} \int_{E=0}^{\varepsilon_{max}} Nr(E)\ E\ (D^2 - R^2(E))\ dE \qquad 2.9$$

and the ionization is given by

$$J_{stopper} = \frac{\pi}{4} \int_{E=0}^{\varepsilon_{max}} Nr(E)\ \frac{E}{W(E)}\ (D^2 - R^2(E))\ dE \qquad 2.10$$

For crossers (wall secondaries which cross the cavity), $\Delta$ is given implicitly by $R(E) = R(E - \Delta) + z$ where z is the path length given by $D\cos\theta$. In order to have a crosser, $z < R(E)$ and hence, $\cos\theta < R(E)/D$. Therefore,

$$z < R(E) \quad \text{if} \quad R(E) < D$$

$$z < D \quad \text{otherwise.}$$

The integral over $\theta$ can be transformed to an integral over z yielding

$$E_{crosser} = \frac{\pi}{2} \int_{E=0}^{\varepsilon_m} Nr(E) \int_{z=0}^{\min(R(E),D)} \Delta(E,z)\ zdz\ dE \qquad 2.11$$

The triangular chord length distribution zdz results from transformation of the isotropic angular distribution within a sphere. The ionization for crossers is given by

$$J_{crosser} = \frac{\pi}{2} \int_{E=0}^{\varepsilon_m} Nr(E) \int_{z=0}^{\min(R(E),D)} \left[\frac{E}{W(E)} - \frac{(E-\Delta)}{W(E-\Delta)}\right] zdz\ dE \qquad 2.12$$

where E/W(E) is the ionization that would be produced by completely stopping a particle of energy E in the gas and $(E-\Delta)/W(E-\Delta)$ is the corresponding ionization for the residual energy $(E-\Delta)$. Such a differential approach is

necessary where W is a strong function of energy and $\Delta$ is large. This completes the calculation of energy and ionization from secondary particles produced in the wall.

For those charged secondaries which originate from pion capture in the cavity material, the calculation of the energy deposition is similar to that above. By analogy with equation 2.1 we define the initial spectrum for pion capture in the cavity material to be

$$N_p^1(\varepsilon) = \Pi^1 K^1(\varepsilon) \qquad 2.13$$

The number of secondaries starting in a volume element dV at $-\bar{L}$, with energy between $\varepsilon$ and $\varepsilon + d\varepsilon$ and travelling in the direction $\bar{L}$ to pass through $\bar{dA}$ (assuming no loss due to slowing-down and isotropic production) is

$$N_p^1(\varepsilon)\, d\varepsilon\, \rho\, \frac{\sin\theta\cos\theta}{4\pi}\, dL\, d\theta\, d\phi\, dA \qquad 2.14$$

The energy deposited in the cavity by such a secondary, $\Delta$, is given implicitly by

$$R(\varepsilon) = R(\varepsilon - \Delta) + L \qquad 2.15$$

where $R(\varepsilon)$ is the range in the cavity material at energy $\varepsilon$ and L is the path length travelled in the cavity. The total energy deposited in the cavity is found by integrating over all the variables. Assuming spherical geometry, the integrals of $\phi$ and dA can be done separately to yield

$$\text{Energy} = \frac{\pi D^2}{2} \int_{\varepsilon} \int_{\theta} \int_{L} \Delta(L,\varepsilon)\, N_p^1(\varepsilon)\, \cos\theta\, \sin\theta\, dL\, d\theta\, d\varepsilon \qquad 2.16$$

For insiders (gas secondaries which remain within the cavity), $\Delta \equiv \varepsilon$ and we must have $R(\varepsilon) < L < D\cos\theta$. Hence $\theta$ varies between 0 and $\theta_m$ given by

$$\cos^{-1} \frac{R(\varepsilon)}{D}$$

The upper limit on $\varepsilon$ is given implicitly by $R(\varepsilon_R) < D$. Thus,

$$E_{insider} = \frac{\pi D^2}{2} \int_{\varepsilon=0}^{\varepsilon_R} \int_{\theta=0}^{\theta_m} \int_{L=R(\varepsilon)}^{D\cos\theta} \varepsilon N_p^1(\varepsilon) \cos\theta \sin\theta \, dL \, d\theta \, d\varepsilon \qquad 2.17$$

Performing the integration on L and then $\theta$ yields

$$E_{insider} = \frac{\pi}{12} \int_{\varepsilon=0}^{\varepsilon_R} (2D^3 - 3D^2R(\varepsilon) + R^3(\varepsilon)) \; \varepsilon N_p^1(\varepsilon) \, d\varepsilon \qquad 2.18$$

Since the insider loses all of its energy within the cavity, the ionization is

$$J_{insider} = \frac{\pi}{12} \int_{\varepsilon=0}^{\varepsilon_R} (2D^3 - 3D^2R(\varepsilon) + R^3(\varepsilon)) \; \frac{\varepsilon}{W(\varepsilon)} \; N_p^1(\varepsilon) \, d\varepsilon \qquad 2.19$$

For starters (gas secondaries which escape from the cavity) we must have $R(\varepsilon) > L$. The integral over L has limits 0 to the minimum of D or $R(\varepsilon)$ and that over $\theta$ has limits 0 to $\theta_m$ given by $\cos\theta_m = L/D$. After performing the integration over $\theta$, we have

$$E_{starter} = \frac{\pi}{4} \int_{\varepsilon=0}^{\varepsilon_{max}} N_p^1(\varepsilon) \int_{L=0}^{\min(D,R(\varepsilon))} \Delta(L,\varepsilon) \; (D^2 - L^2) \, dL \, d\varepsilon \qquad 2.20$$

and

$$J_{starter} = \frac{\pi}{4} \int_{\varepsilon=0}^{\varepsilon_{max}} N_p^1(\varepsilon) \int_{L=0}^{\min(D,R(\varepsilon))} \left[\frac{\varepsilon}{W(\varepsilon)} - \frac{(\varepsilon-\Delta)}{W(\varepsilon-\Delta)}\right](D^2 - L^2) \, dL \, d\varepsilon \qquad 2.21$$

This completes the derivation of the equations required to calculate the energy and ionization deposited in the cavity due to secondaries which originate from pion stars in the cavity. These quantities and equations have been summarized in appendix B. It should be noted that the integrals for stoppers and crossers involved the slowing-down spectrum Nr(E) as produced

by pion capture in the wall and subsequent slowing-down in the wall. On the other hand, the integrals for starters and insiders involve $\overset{1}{N}p(\varepsilon)$, the primary spectrum as produced in the cavity. In the process of calculating r, the cavity will alternatively be considered to be filled with gas and wall. For the former, $\overset{1}{N}p(\varepsilon)$ will be the spectrum due to gas, and in the latter, $\overset{1}{N}p(\acute{\varepsilon}) = Np(\varepsilon)$ due to wall material.

## 2.3 INPUT DATA

### 2.3.1 Pion Star Data

#### 2.3.1.1 Secondary spectra for carbon and oxygen

In order to carry out the calculations outlined in 2.2, the energy spectra of secondaries, $K(\varepsilon)$ (equation 2.3), are required. These energy spectra have been studied in medium energy physics in an attempt to understand the nuclear substructure. The pion-nucleus interaction can be considered a two stage process. The first stage yields high energy secondaries due to direct processes such as absorption of the pion on a nuclear pair or possibly an alpha particle cluster. The second stage yields lower energy secondaries due to "evaporation" of particles from the residual excited nucleus.

Guthrie (14) has used the intranuclear-cascade model to calculate secondary spectra, but this calculation places too much energy into charged particles: 42.7 MeV per pion stopped in carbon and 36.7 MeV per pion stopped in oxygen. Various experimenters (18, 19, 20, 21, 22, 23) have measured spectra for some of the secondaries over limited energy ranges. Data taken by a Karlsruhe group (24, 25, 26, 27) working at SIN have been used exclusively in this calculation. These data are comprehensive in that all of the energetic secondaries were measured from the experimental energy threshold up to the kinematical limit. The spectra for the different particle types are determined simultaneously by a multiparameter data acquisition system which records differential and total energy loss and time-of-flight. Their thin (20 $mg/cm^2$) target data have been corrected for particle loss and energy absorption using the unfolding procedure of Comiso (28).

The data for secondary spectra from pion absorption on a carbon ($CH_2$) target (24, 25) are shown in figure 2.1. The data for oxygen have been extracted

from preliminary Karlsruhe data (26, 27) for mylar and acetate which have relative capture ratios on carbon and oxygen of 1.7:1 and 1.1:1 respectively (26). The extraction procedure is outlined in appendix C and the data are displayed in figure 2.2. The yield of neutrons is about the same case (140). The yield of charged particles from oxygen is considerably reduced compared to carbon, particularly for He and Li ions.

Particle and energy balance sheets are given in tables 2.1 and 2.2. Each table is divided in half: the upper half records information for the observed particles and the lower half shows a possible scheme for completing the balance sheet. Consider table 2.1 for carbon. The stated errors of the multiplicities and the average energy per pion stop are 10% and 15 to 20% respectively including systematic errors (24). The total kinetic energy for observed particles is 103.5 MeV including neutrons and 27.5 MeV without them. 4.79 neutrons and 2.88 protons are accounted for. If the missing nucleons are assigned to unobserved recoil nuclei, then it is possible to check whether or not the total energy sums to the pion rest mass. Several of such recoils have been measured, but since only an estimate is required, then the recoils were taken to be $^{9}Be$ and $^{10}B$. The former is required to provide a slight excess of neutrons over protons and the latter is expected to be prominent on the basis of capture on a quasideuteron $^{12}C$ ($\pi^-$, nn) $^{10}B$. If it is assumed that a recoil nucleus carries 3 MeV (25) then the unobserved kinetic energy is 1.32 MeV. If the amount of gamma ray energy is taken to be 2 MeV for radiative capture and 3 MeV for nuclear excitation, then Kinetic Energy + Gamma Rays + Binding Energy of $^{12}C$ - Residual Binding Energy is 104.77 + 5 + 92.162 - 55.213 giving 146.7 MeV. This is slightly larger than the pion rest mass energy of 139.6 MeV, but it is within the limits of the error.

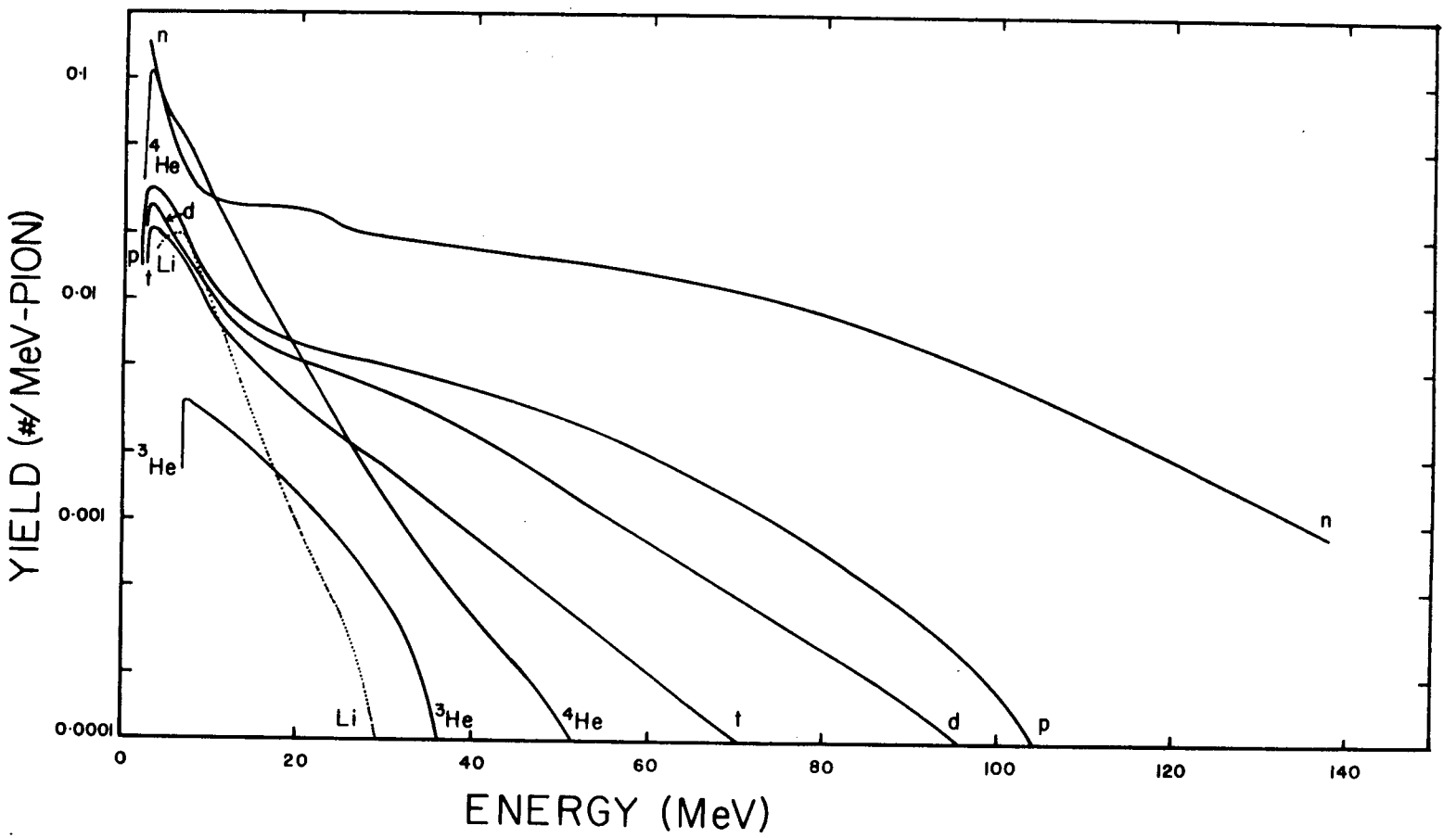


Figure 2.1: Secondary Spectra for Pion Absorption on Carbon

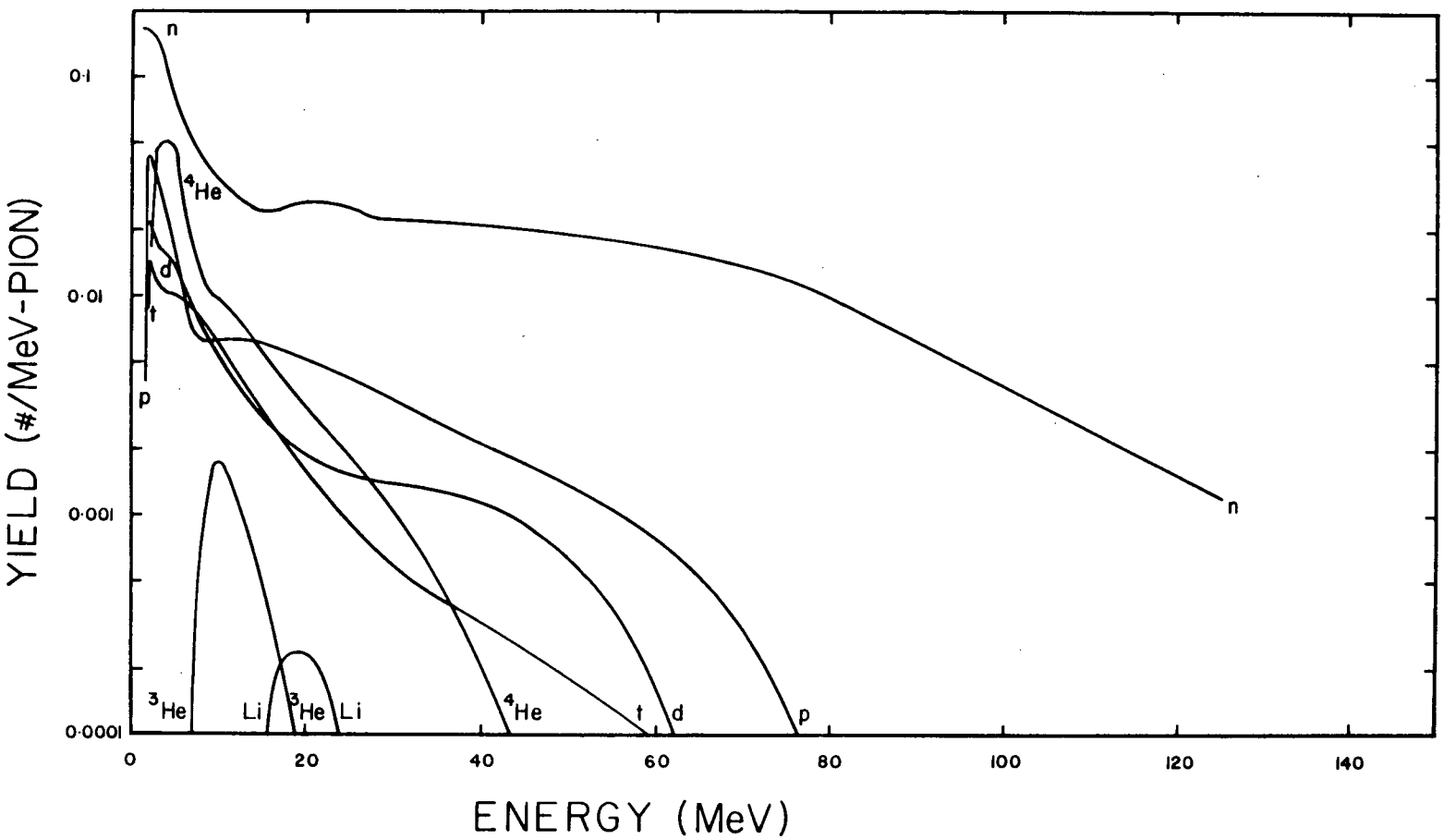


Figure 2.2: Secondary Spectra for Pion Absorption on Oxygen

Now consider table 2.2 for oxygen. The total observed kinetic energy is 91.0 MeV including neutrons and 12.0 MeV excluding them. The number of observed particles accounts for 3.74 neutrons and 1.22 protons. The missing nucleons can be accounted for by assigning them to the recoil nuclei. Again, the assignment is somewhat arbitrary. $^{14}N$ is expected from capture on a quasideuteron, $^{16}O$ ($\pi^-$, nn) $^{14}N$ and $^{12}C$ from capture on an alpha cluster $^{16}O$ ($\pi^-$, nt) $^{12}C$. A study of prompt nuclear X-rays following pion capture (29) has shown that these recoils predominate, that the total yield of carbon and nitrogen isotopes is roughly equal, and that the average recoil energy is 2.2 MeV for carbon and 0.6 MeV for nitrogen. Since there is an excess of missing protons, $^{7}Be$ is also included. Then, Kinetic Energy + Gamma Rays + Binding Energy of $^{16}O$ - Residual Binding Energy is 93.36 + 5 + 127.621 - 85.722 giving 140.3 MeV, which is very close to the pion rest mass.

Table 2.3 is a summary to compare carbon and oxygen data. The amount of kinetic energy carried away by charged particles for oxygen is about half that for carbon. While the total energy balance is confirmatory, it is not a definitive test because the energy going into charged particles is only a small fraction of the total. Although quantitatively incorrect, Guthrie's calculation (14) predicted a lower yield of charged secondaries from oxygen than from carbon. The oxygen results used here have been extracted from preliminary data (26, 30), however, the lower energy into charged particles from oxygen is plausible and is expected to be of this magnitude when the measurements have been confirmed. The difference appears to be due partly to the energy going into neutrons and partly to changes in the binding energy. Further implications for the kerma factor will be discussed in chapter 3.

Table 2.1: Particle and Energy Balance Sheet for Carbon

| Particle | Total Number of Particles | Total Kinetic Energy (MeV) | | Number of Neutrons | Number of Protons | Binding Energy (MeV) | Total Binding Energy (MeV) |
|---|---|---|---|---|---|---|---|
| n | 2.1 | 76 | | 2.1 | - | 0 | 0 |
| p | .452 | 10.51 | | - | .452 | 0 | 0 |
| d | .329 | 6.38 | | .329 | .329 | 2.225 | .732 |
| t | .222 | 3.07 | | .444 | .222 | 8.482 | 1.883 |
| $^{3}He$ | .041 | 0.64 | 27.45 | .041 | .082 | 7.718 | .316 |
| $^{4}He$ | .649 | 5.51 | | 1.298 | 1.298 | 28.296 | 18.364 |
| $^{6,7}Li$ | .165 | 1.34 | | .578 | .495 | 35.620 | 5.877 |
| Totals | | 103.45 | | 4.790 | 2.878 | | 27.172 |
| Missing | | | | 2.210 | 2.122 | | |
| $^{9}Be$ | .088 | .26 | 1.32 | .440 | .352 | 58.165 | 5.119 |
| $^{10}B$ | .354 | 1.06 | | 1.770 | 1.770 | 64.751 | 22.922 |
| Adjusted Totals | | 104.77 | | 7 | 5 | | 55.213 |

Table 2.2: Particle and Energy Balance Sheet for Oxygen

| Particle | Total Number of Particles | Total Kinetic Energy (MeV) | | Number of Neutrons | Number of Protons | Binding Energy (MeV) | Total Binding Energy (MeV) |
|---|---|---|---|---|---|---|---|
| n | 2.7 | 79 | | 2.7 | - | 0 | 0 |
| p | .292 | 5.24 | | - | .292 | 0 | 0 |
| d | .167 | 2.39 | | .167 | .167 | 2.225 | .372 |
| t | .125 | 1.52 | 11.99 | .250 | .125 | 8.482 | 1.060 |
| $^{3}He$ | .012 | .20 | | .012 | .024 | 7.718 | .093 |
| $^{4}He$ | .304 | 2.61 | | .608 | .608 | 28.296 | 8.602 |
| $^{6,7}Li$ | .002 | .03 | | .007 | .006 | 35.620 | .071 |
| Total | | 90.99 | | 3.744 | 1.222 | | 10.198 |
| Missing | | | | 5.256 | 5.778 | | |
| $^{7}Be$ | .522 | 1.57 | | 1.566 | 2.088 | 37.600 | 19.627 |
| $^{12}C$ | .284 | .63 | 2.37 | 1.704 | 1.704 | 92.163 | 26.174 |
| $^{14}N$ | .284 | .17 | | 1.988 | 1.988 | 104.660 | 29.723 |
| Adjusted Totals | | 93.36 | | 9 | 7 | | 85.722 |

Table 2.3: Comparison of Carbon and Oxygen Energy Distributions (MeV)

| | Carbon | | Oxygen | |
|---|---|---|---|---|
| Kinetic Energy Neutrons | 76 ± 8 | | 79 ± 8 | |
| Kinetic Energy Charged Particles (observed) | 27.5 | 28.8 ± 3 | 12.0 | 14.4 ± 5 |
| Kinetic Energy Charged Particles (unobserved) | 1.3 | | 2.4 | |
| Gamma Ray Energy | 5 ± 3 | | 5 ± 3 | |
| Change in Binding Energy | 37 ± 5 | | 42 ± 5 | |
| Total | 147 ± 10 | | 140 ± 11 | |

2.3.1.2 Fermi-Teller Z-law

When pions are captured in a medium which contains both carbon and oxygen, the charged particle spectra will be given by the sum of the spectra for the individual elements weighted according to the nuclear capture probability. Fermi and Teller (31) predicted that for a metallic compound of the form AnBm, the capture probability ratio into the atom A compared to that into the atom B is $nZ_A/mZ_B$. That is, the capture probability per atom is proportional to Z.

For muons, experimental (32) and theoretical (33) work has revealed that the capture probability is not linear in Z, but is proportional to $Z^n$ where $0.55 < n < 1.41$ and n varies with position in the periodic table. Recent work at LAMPF (34) using muonic X-rays has shown that a modified Z-law which distributes the muons among the atoms (including hydrogen) according to the Z-law and then transfers the muon from hydrogen to the nearest heavy atom gives better agreement with experiment than the Z-law alone.

Other than some Russian (35) theoretical and experimental investigations of pion absorption in hydrogenous compounds and some early work (36, 37), there has not been as much study of pionic capture as muonic capture. Effects in pion capture at the 10 to 20% level due to different chemical and physical composition have been observed (38, 39). Generally these condensed state effects seem less prominent with pions than with muons. The Karlsruhe group (26) has found for pion capture on carbon and oxygen in mylar and acetate that the nuclear capture ratio as predicted by chemical analysis and the Z-law agreed within 10% with the ratio as measured by the detection of pionic X-rays.

Based on this information, the secondary spectra for capture in compounds were evaluated using the Z-law. For hydrogenous compounds it was assumed that all of the pions initially captured on hydrogen were transferred to adjacent heavy atoms.

2.3.1.3 Pion stopping density

In section 2.2 it was pointed out that the pion stars were taken to be uniformly distributed throughout the infinite phantom and the cavity material with stopping densities $\Pi$ and $\Pi^1$ (pion/g) respectively. In general $\Pi \neq \Pi^1$ if the stopping powers of the phantom and cavity are different.

Consider a mono-directional stopping pion beam normally incident on a slab-shaped cavity containing an areal density ($\rho$ g/cm$^2$) of wall in one case and the same areal density of gas in the other case. Assume that the pion energy fluence has been selected to provide a uniform stopping density of $\Pi$ pions/g in the walls and wall material filling the cavity. When the cavity is filled with gas, consider a pion with the correct energy $E_0$ to just cross the gas. $R_g(E_0) = \rho$ g/cm$^2$. A pion with the same energy $E_0$ will have a range in wall material of $R_w(E_0)$. The two ranges are different if the stopping powers are different. The number of pions per unit area with energy less than $E_0$ is $\Pi\ R_w(E_0)$. Therefore the number of pions per unit area stopping in the gas is also $\Pi\ R_w(E_0)$, and hence the average pion stopping density in the gas is

$$\Pi^1 = \Pi\ R_w(E_0)/R_g(E_0) \qquad 2.22$$

If the gas has a higher stopping power than the wall, then the pion range will be smaller and the stopping density will be increased. Notice that $E_0$ depends upon the chamber size and gas density. If the ratio of the ranges is not independent of $E_0$ then the stopping density will be pressure dependent.

In order to evaluate this effect, it is necessary to know the range of low energy pions. Since no experimental data were available, range versus energy curves for pions were determined by integrating pion stopping powers

derived by scaling proton data (section 2.3.2). Figure 2.3 shows the ratio of the pion ranges for carbon to methane and for carbon to carbon dioxide as a function of areal density. The dose deposited by insiders and starters needs to be multiplied by this ratio. For $CO_2$, the ratio is slightly less than unity and changes by only a few percent over the range of pressures used experimentally. For $CH_4$, the ratio is about 1.5 and varies by 20%.

Due to the uncertainty in the value of this ratio, the calculations outlined in section 2.2 were performed with $\Pi = \Pi^1$ and this effect was subsequently included as a separate step. The uncertainty arises because of the proton scaling procedure used to determine the range and because of the failure to include the effects of multiple scatter. For example, the scaling procedure would predict equal ranges for positive and negative pions, whereas experimentally they differ by 3% at 1.6 MeV (40). The inclusion of multiple scatter would increase the effective size of the chamber, thus causing a shift up the areal density axis which would make the magnitude of the ratios closer to the stopping power ratio.

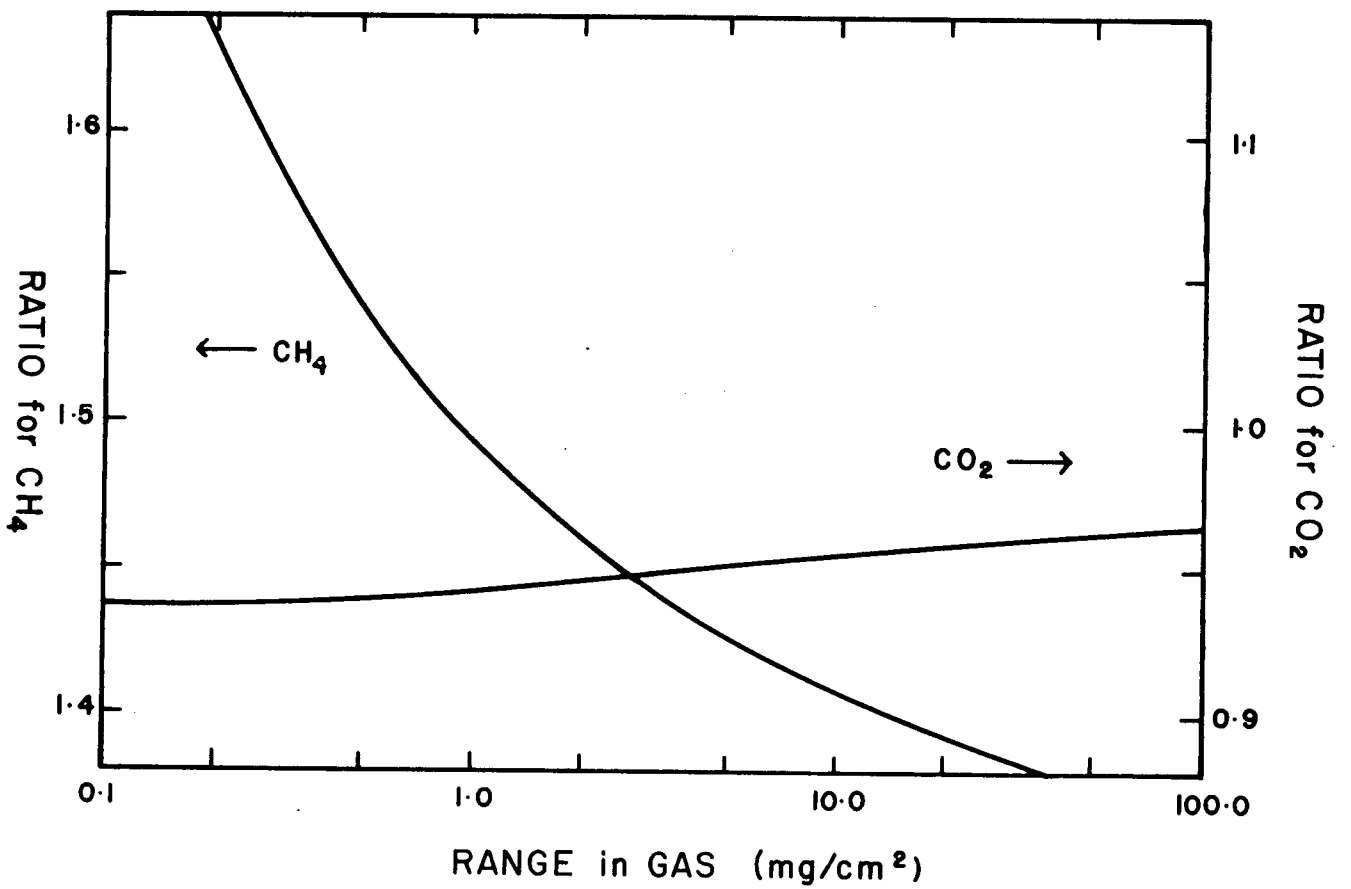


Figure 2.3: Range Ratio for Carbon/Methane and Carbon/Carbon Dioxide

2.3.2 Stopping Power Data

2.3.2.1 Stopping power for H and He ions in the elements H, C and O

For H and He ions stopping in the elements H, C and O, the analytical fits to the experimental data as derived by Andersen and Ziegler (41, 42) have been used. The stopping power versus energy curve behaves differently in each of three regions. At low energy, the Fermi-Thomas potential has been used to predict stopping power proportional to velocity. At high energy, Bethe theory with appropriate values for the ionization potential and shell corrections is found to be applicable. In the intermediate energy region, where the stopping power passes through a peak, empirical fits have been made to the data.

There are discrepancies of the order of 10% between experimental measurements made within the last decade, particularly in the intermediate energy range. The approach of Andersen and Ziegler implicitly denies the ability of any one experiment to yield a value closer to the true value than any other experiment. In taking an average over various experimental determinations any hidden systematic errors between these experiments ought to cancel out. If several independent experiments find agreement on a new value different from the present Andersen and Ziegler fit, then it would be practical to modify the constants to fit the newly accepted value.

Before adopting this approach, all of the references cited in the Andersen and Ziegler bibliography (43) and new data (44, 45, 87) not available to them were plotted and compared to their fitted values. Representative carbon data is shown in figures 2.4 and 2.5. Most of the discrepancy is in the region of the peak where the maximum deviation is 8%. This discrepancy does not appear to be excessive, and there seems to be no reason to prefer one set of experimental results over the others. Therefore

Figure 2.4: Stopping Cross Section for Protons in Carbon

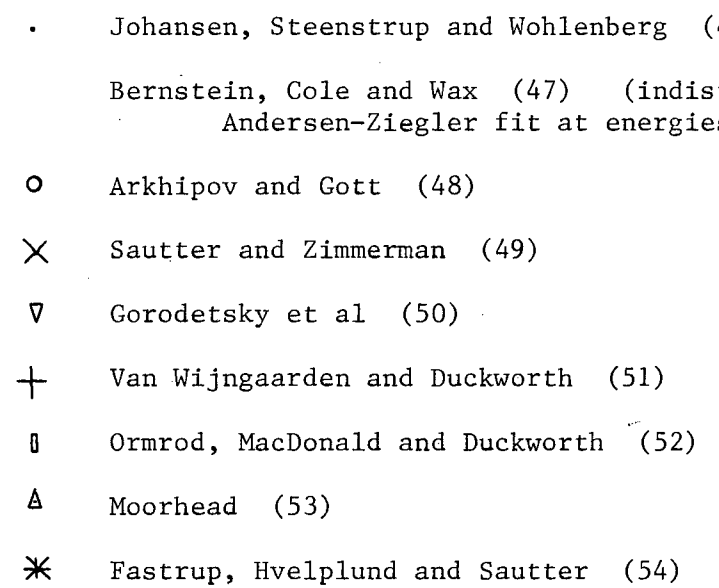

· Johansen, Steenstrup and Wohlenberg (46)

Bernstein, Cole and Wax (47) (indistinguishable from the Andersen-Ziegler fit at energies less than 20 keV)

o Arkhipov and Gott (48)

× Sautter and Zimmerman (49)

▽ Gorodetsky et al (50)

+ Van Wijngaarden and Duckworth (51)

▯ Ormrod, MacDonald and Duckworth (52)

△ Moorhead (53)

✳ Fastrup, Hvelplund and Sautter (54)

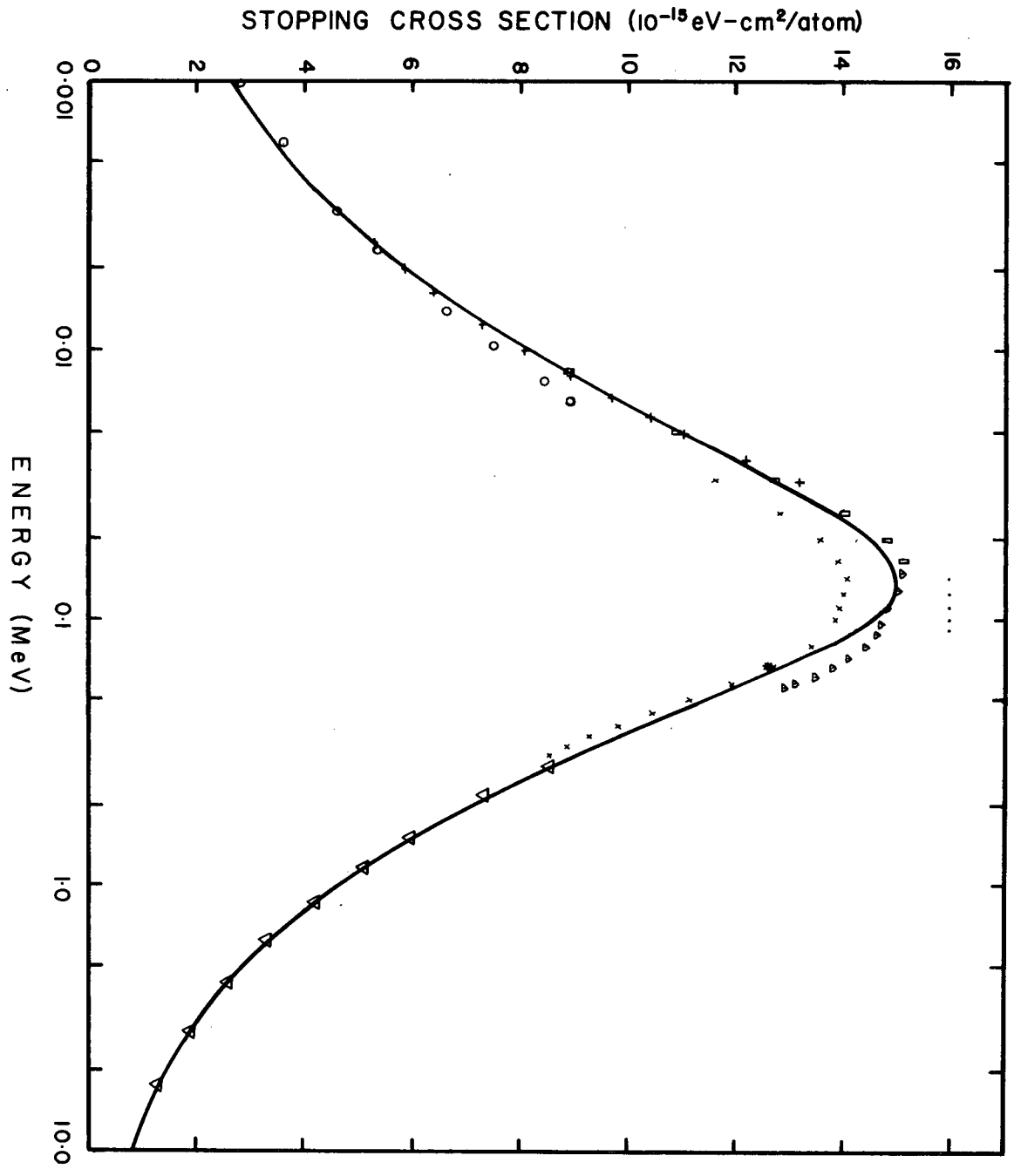
STOPPING CROSS SECTION (10⁻¹⁵ eV-cm²/atom)
0
2
4
6
8
10
12
14
16
ENERGY (MeV)
0·001
0·01
0·1
1·0
10·0

Figure 2.5: Stopping Cross Section for Alphas in Carbon

Santry and Werner (44)


Santry and Werner (45)

Sautter and Zimmerman (49)


Van Wijngaarden and Duckworth (51)

Moorhead (53)


Porat and Ramavataram (56)


Matteson, Chau and Powers (57) [graphite, vapour deposition]

Chu and Powers (58)

Ormrod and Duckworth (59)

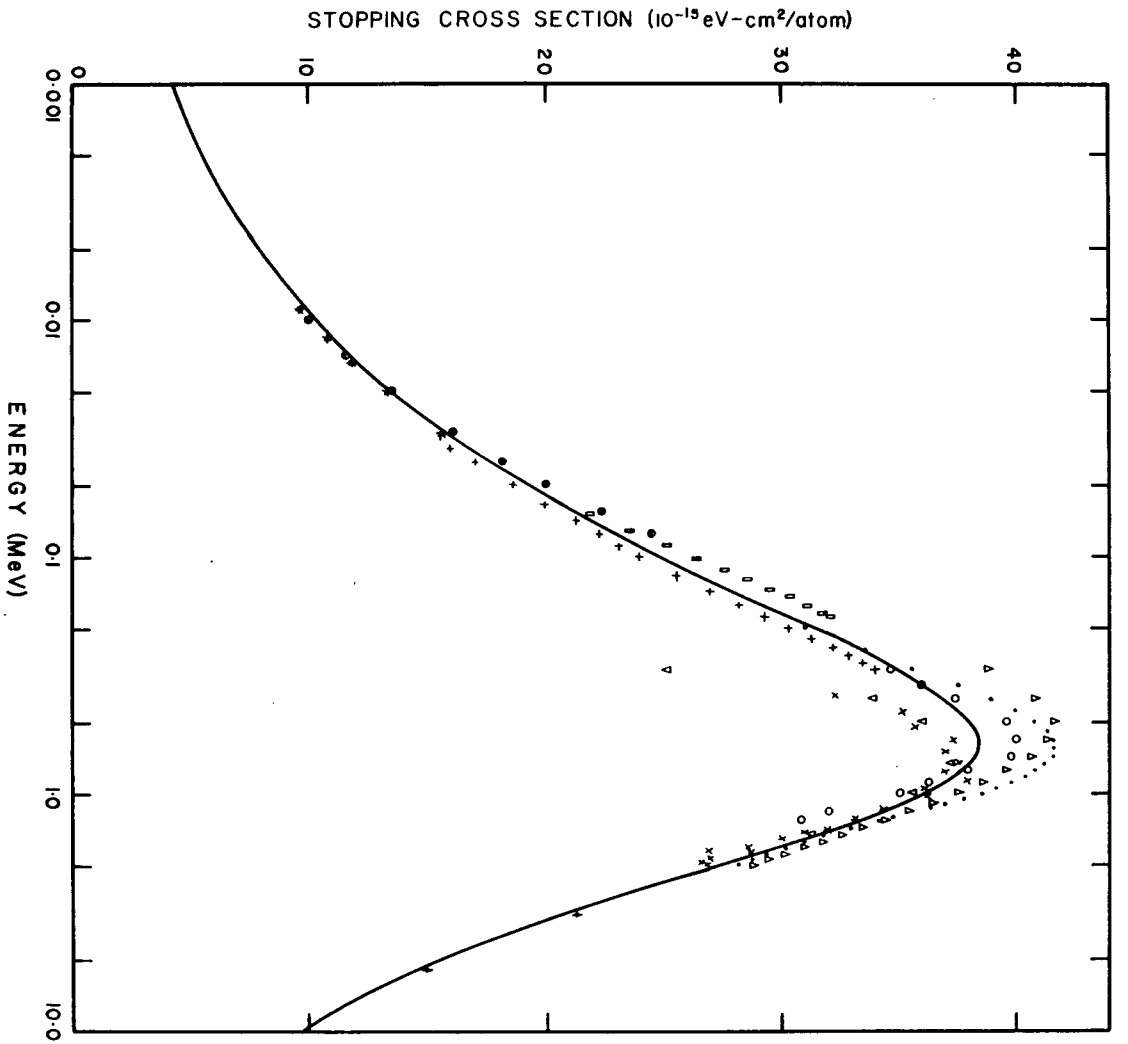
STOPPING CROSS SECTION (10⁻¹⁵ eV-cm²/atom)
0
10
20
30
40
ENERGY (MeV)
0·001
0·01
0·1
1·0
10·0

the fits of Andersen and Ziegler were accepted as reliable summaries of the experimental stopping powers.

The elastic nuclear scattering contribution to the stopping power is small and was not included in these calculations.

In section 1.2.2 it was pointed out that Thwaites (15) has shown that the stopping power ratio for vapour to solid is not unity at low energies. In fact, it may be as large as 1.25 for 1 MeV alpha particles in hydrocarbons. The Andersen and Ziegler tables do consider such condensed state effects for alphas by tabulating separate constants for gas and solid phases and their values for carbon compare very well with those of Thwaites (15). For protons, Andersen and Ziegler indicate the ratio is unity, whereas Thwaites indicates a maximum value of 1.1 between 0 and 2 MeV.

2.3.2.2 Bragg additivity rule

The Bragg additivity rule (64) states that the stopping power of a medium is the sum of the stopping powers of its atomic components and is independent of both the chemical relationships between its constituents and the physical state of the medium. This rule describes (65, 66, 67, 68, 69) a limited number of compounds, ions and energy regions, but it has not been found to be universally valid (70, 71, 72, 73, 74, 75). The review by Thwaites (15) includes additional references to the condensed state effects. There is insufficient information in these references to decide if the Bragg rule is valid for methane and carbon dioxide. Hence, the stopping power in H, C and O was calculated (as in 2.3.2.1), combined according to the Bragg rule and compared with the available experimental data in figures 2.6 through 2.9. The fit is excellent except for the case of protons in carbon dioxide where the Bragg rule predicts a value 8% higher at the peak than observed by the one available experiment. Such agreement justifies the use of the Andersen and Zeigler values and the Bragg rule for these two gases, but it does not validate the rule for general use.

Figure 2.6: Stopping Cross Section for Protons in $CO_2$

o Swint, Prior and Ramirez (77)

▯ Brolley and Ribe (78)

Δ Phillips (79)

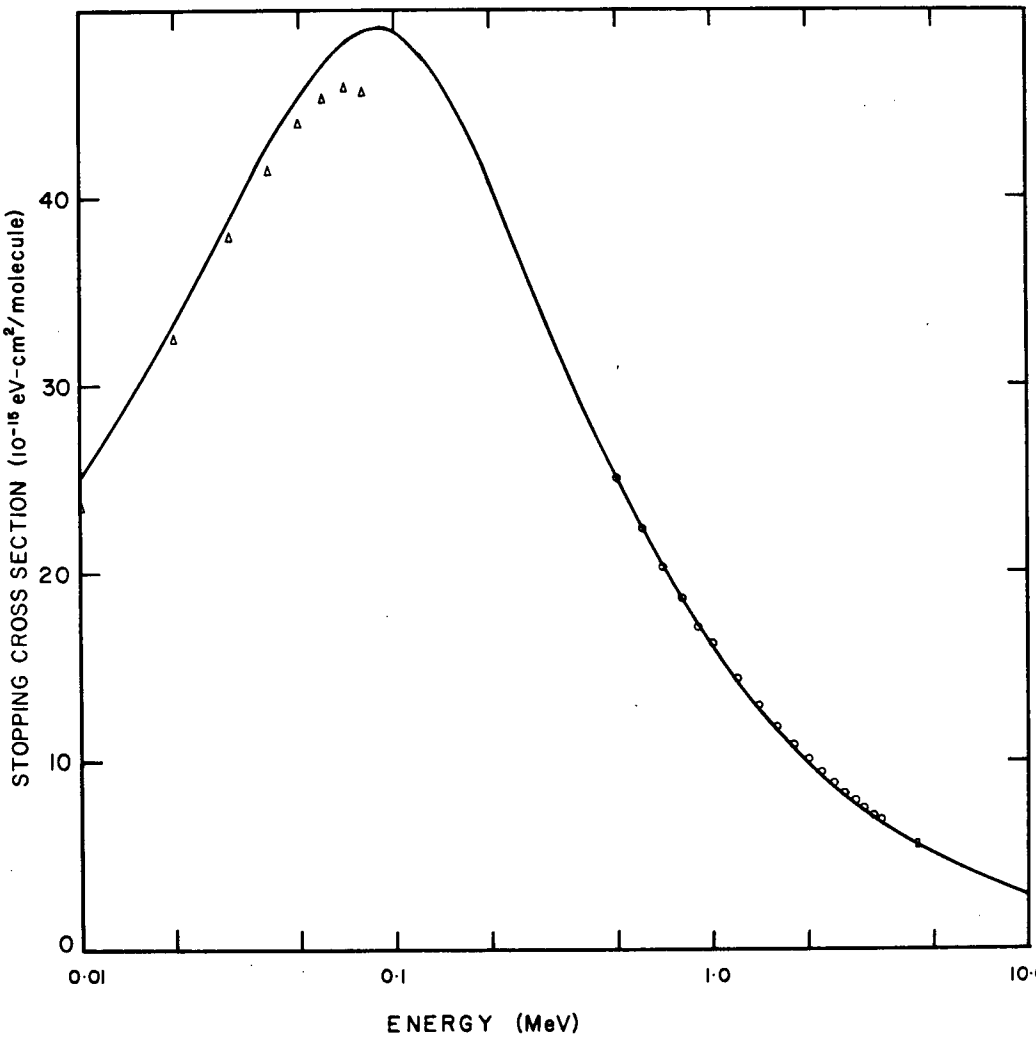
STOPPING CROSS SECTION (10⁻¹⁵ eV-cm²/molecule)
40
30
20
10
0
0·01
0·1
1·0
10·0
ENERGY (MeV)

Figure 2.7: Stopping Cross Section for Protons in $CH_4$

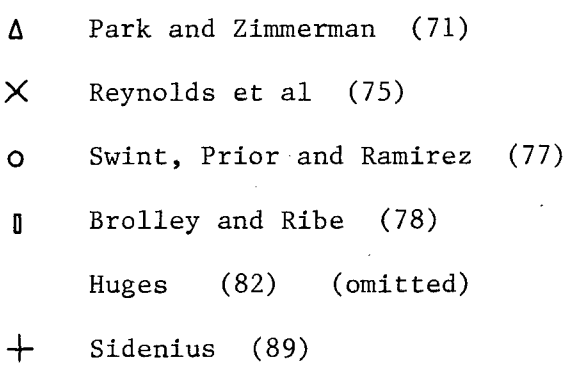

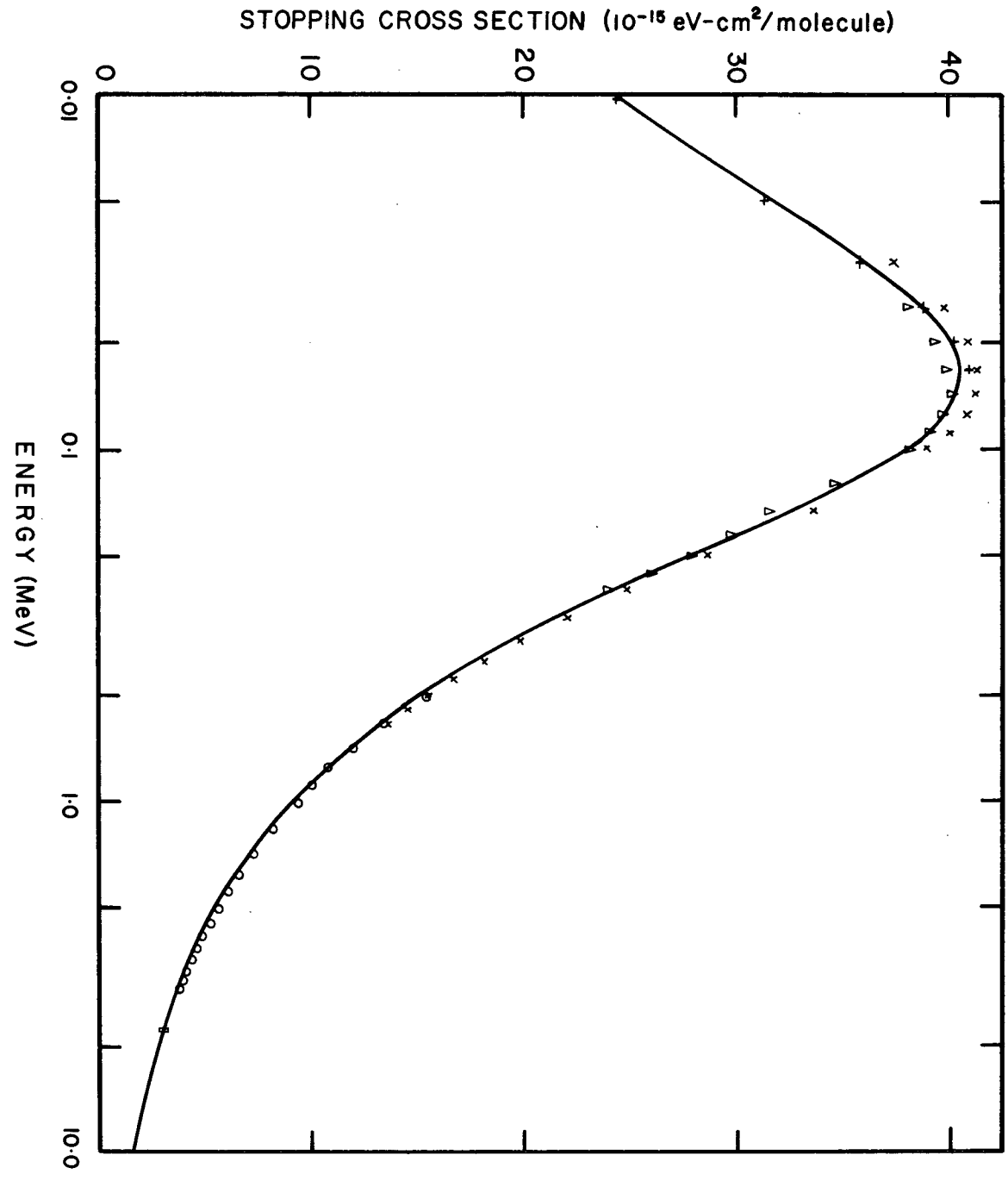
STOPPING CROSS SECTION (10⁻¹⁵ eV-cm²/molecule)
0
10
20
30
40
ENERGY (MeV)
0·01
0·1
1·0
10·0

Figure 2.8: Stopping Cross Section for Alphas in $CO_2$

Δ Bourland, Chu and Powers (83)

× Kerr et al (84)

o Rotondi (85)

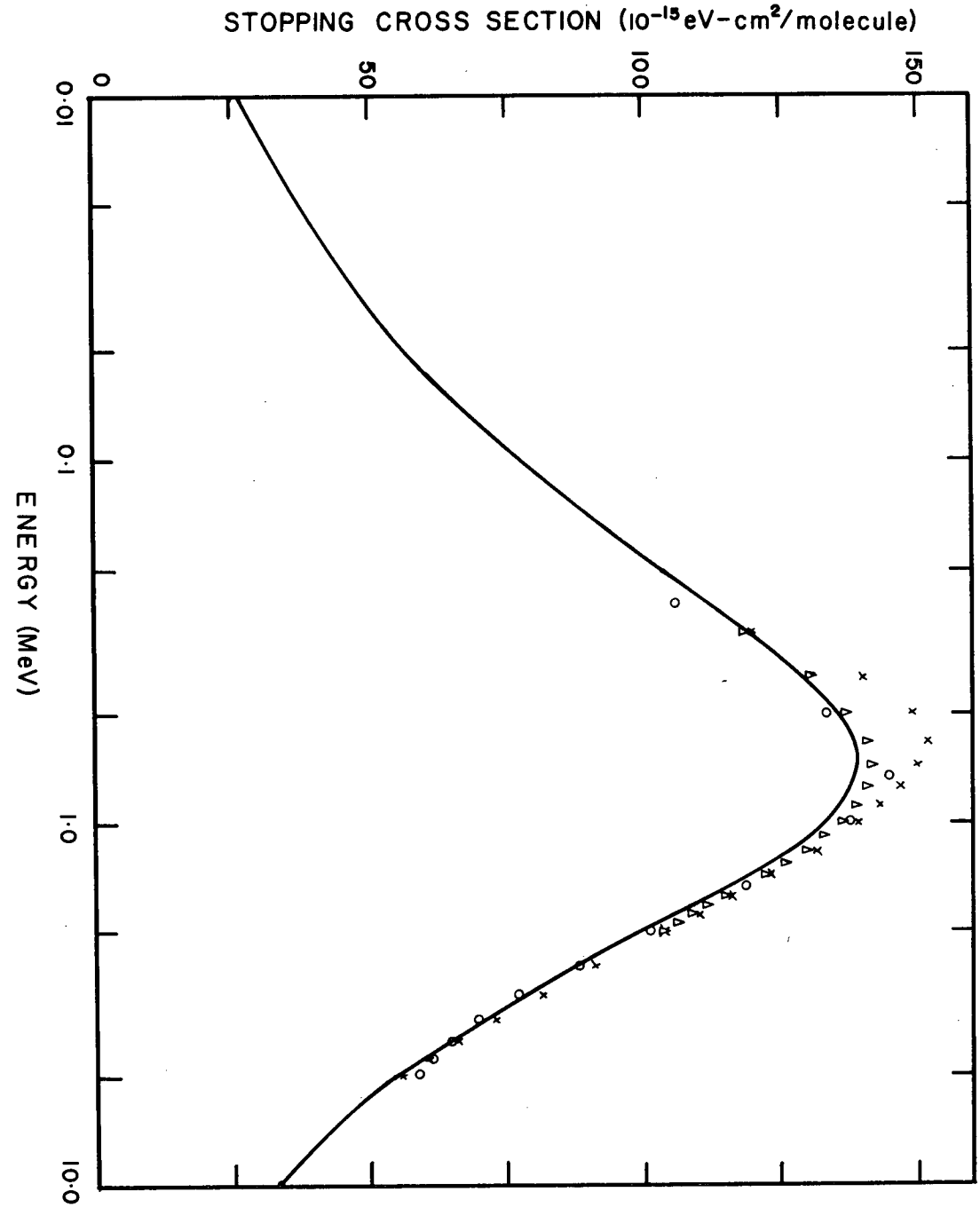
STOPPING CROSS SECTION ($10^{-15}$ eV-cm$^2$/molecule)
0
50
100
150
10·0
1·0
0·1
0·01
ENERGY (MeV)

Figure 2.9: Stopping Cross Section for Alphas in $CH_4$


Park (68)


Bourland, Chu and Powers (83)


Kerr et al (84)


Rotondi (85)


Whillock and Edwards (87)


Sidenius (89)

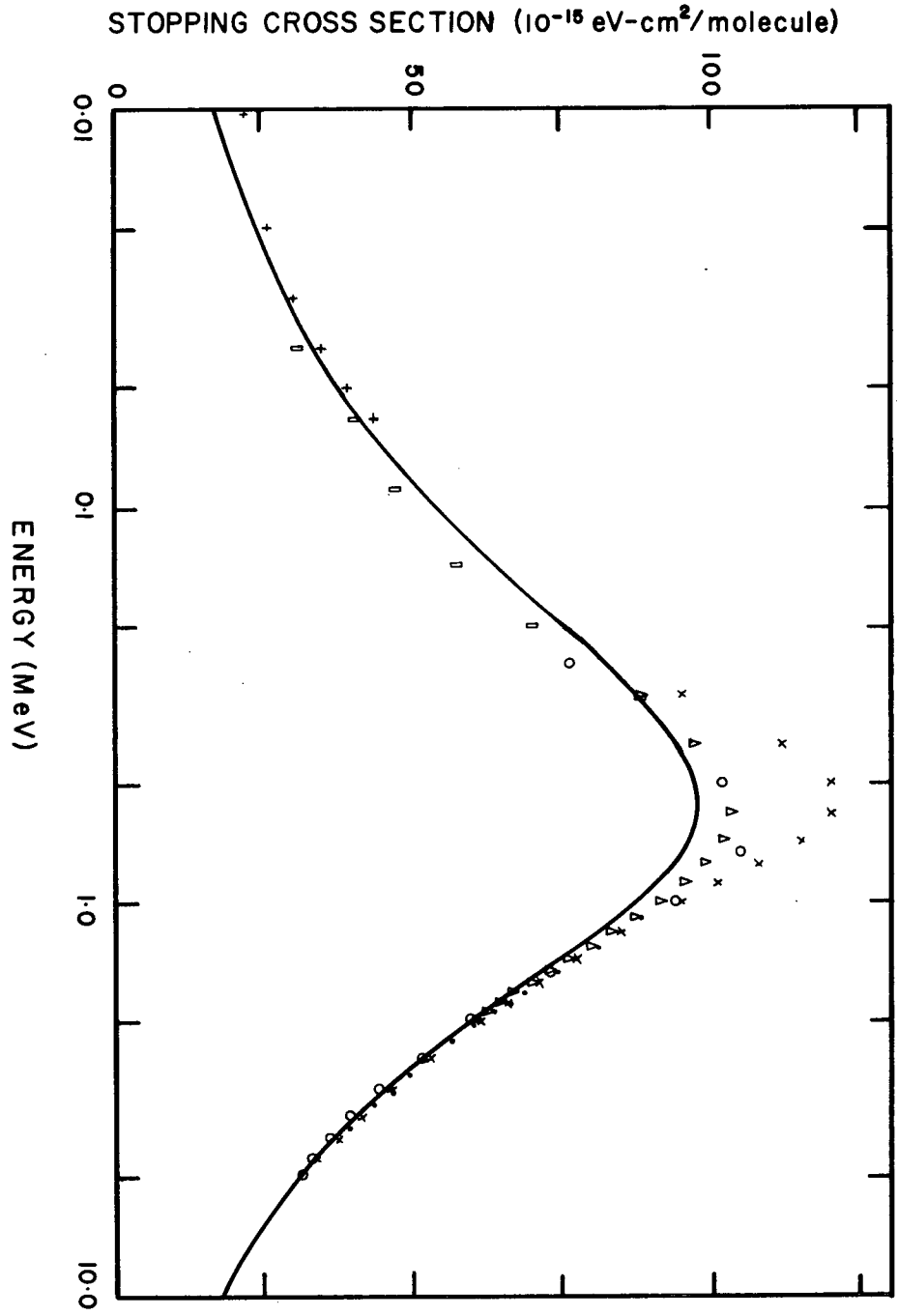
STOPPING CROSS SECTION (10⁻¹⁵ eV-cm²/molecule)
0
50
100
ENERGY (MeV)
10·01
0·1
1·0
10·0

2.3.2.3 Stopping power for lithium

The experimental data for stopping lithium ions is very sparse. In carbon there was no data available above 150 keV, although recent data by Santry (45) now extends to the peak region. The analytical fit for carbon to be published (92) (fall of 1979) by Ziegler does not extend below 1.4 MeV where the ion becomes partially charged. In carbon dioxide there is one experiment which covers the peak (88). In methane an experiment (89) is available below 150 keV and two other experiments (88, 90) in the peak region disagreed by 25%. A curve of the square of the effective charge as a function of velocity was generated by comparing the stopping power for lithium in a given material to the stopping power for protons of the same velocity as determined by Andersen and Ziegler and the Bragg rule:

$$Z^2 = \frac{\frac{dE}{dx}\ \text{Li, } v_1\text{, G}}{\frac{dE}{dx}\ \text{P, } v_1\text{, G}} \qquad 2.23$$

(G refers to a particular compound.) This curve is shown in figure 2.10. Except for minor departures by hydrogen, all the gases fall on the same curve. At low velocity, the available data for carbon indicated a larger value of $Z^2$ than for gases. Since there was no carbon data available for $v > v_0$, where $v_0$ is the Bohr velocity = c/137, stopping power data for aluminum were used as well as measurements of $Z^2$ (96, 97) for Li ions leaving carbon foils. At a particular velocity, the former technique gave $Z^2$ higher than for gases, and the latter technique gave $Z^2$ lower. Hence, for $v \geq v_0$ $Z^2$ for carbon was taken to be the same as for gases. Stopping powers, based on the effective charge and proton stopping powers, for the lithium ions in carbon, methane and carbon dioxide are shown in figures 2.11, 2.12 and 2.13.

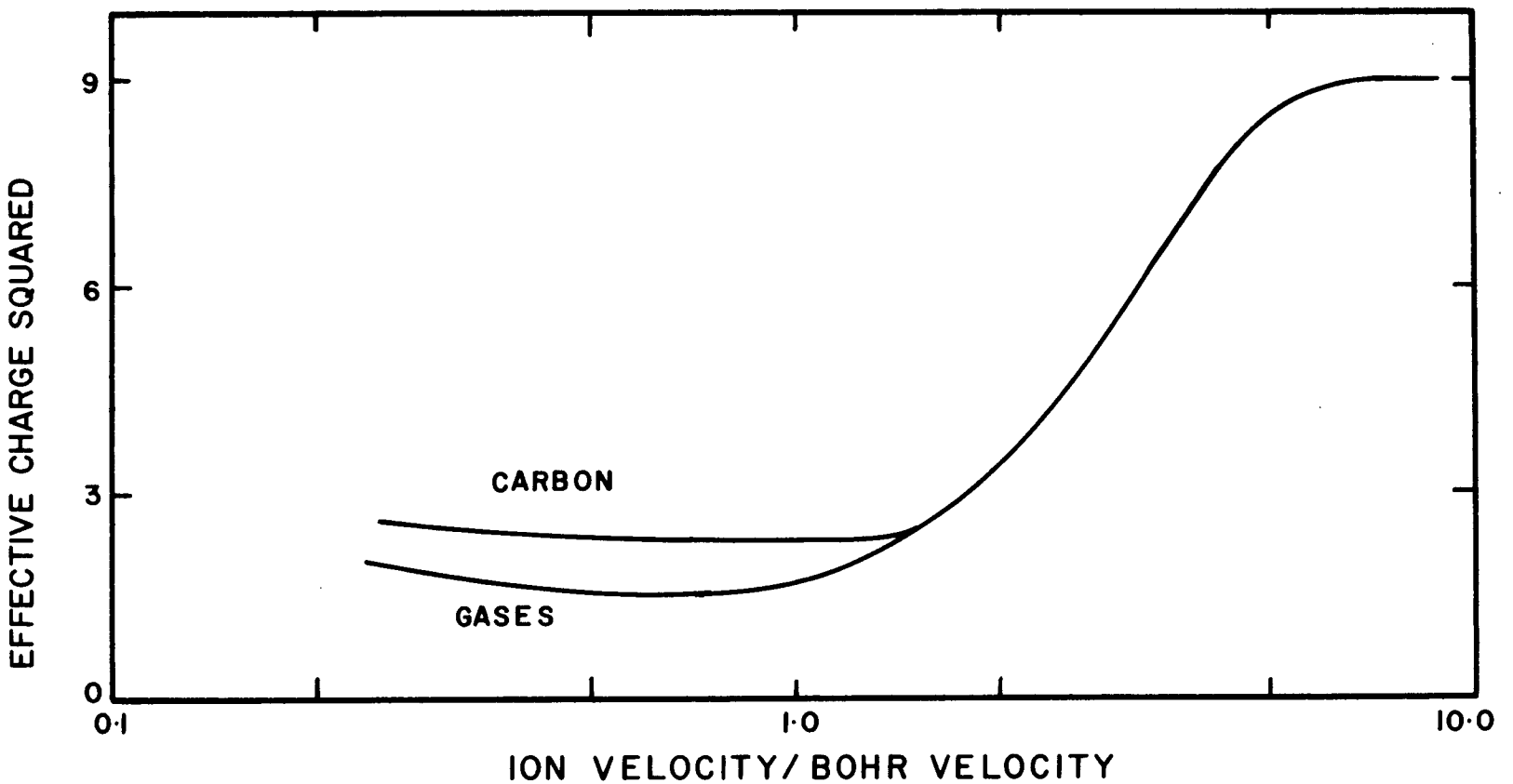


Figure 2.10: Square of the Effective Charge for Lithium Ions

Figure 2.11: Stopping Cross Section for Li Ions in Carbon

× Santry and Werner (45)

\+ Ormrod and Duckworth (59)

Δ Ziegler (92)

o Högberg (93)

• Pivovar, Nikolaichuk and Rashkovan (94)

▯ Bernhard et al (95)

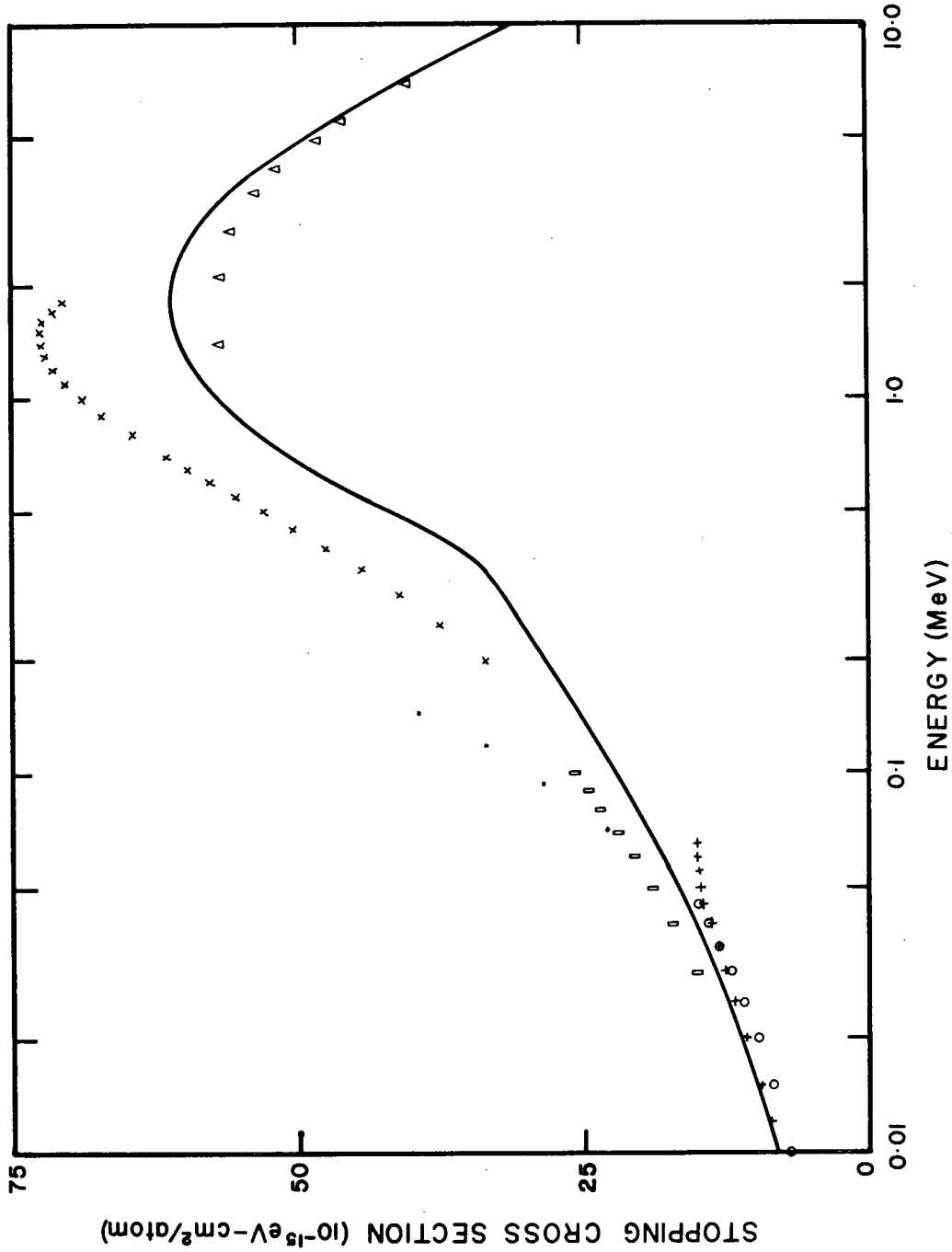
STOPPING CROSS SECTION (10⁻¹⁵eV-cm²/atom)
75
50
25
0
0·01
0·1
1·0
10·0
ENERGY (MeV)

Figure 2.12: Stopping Cross Section for Li Ions in $CO_2$

- Allison, Anton and Morrison (88)

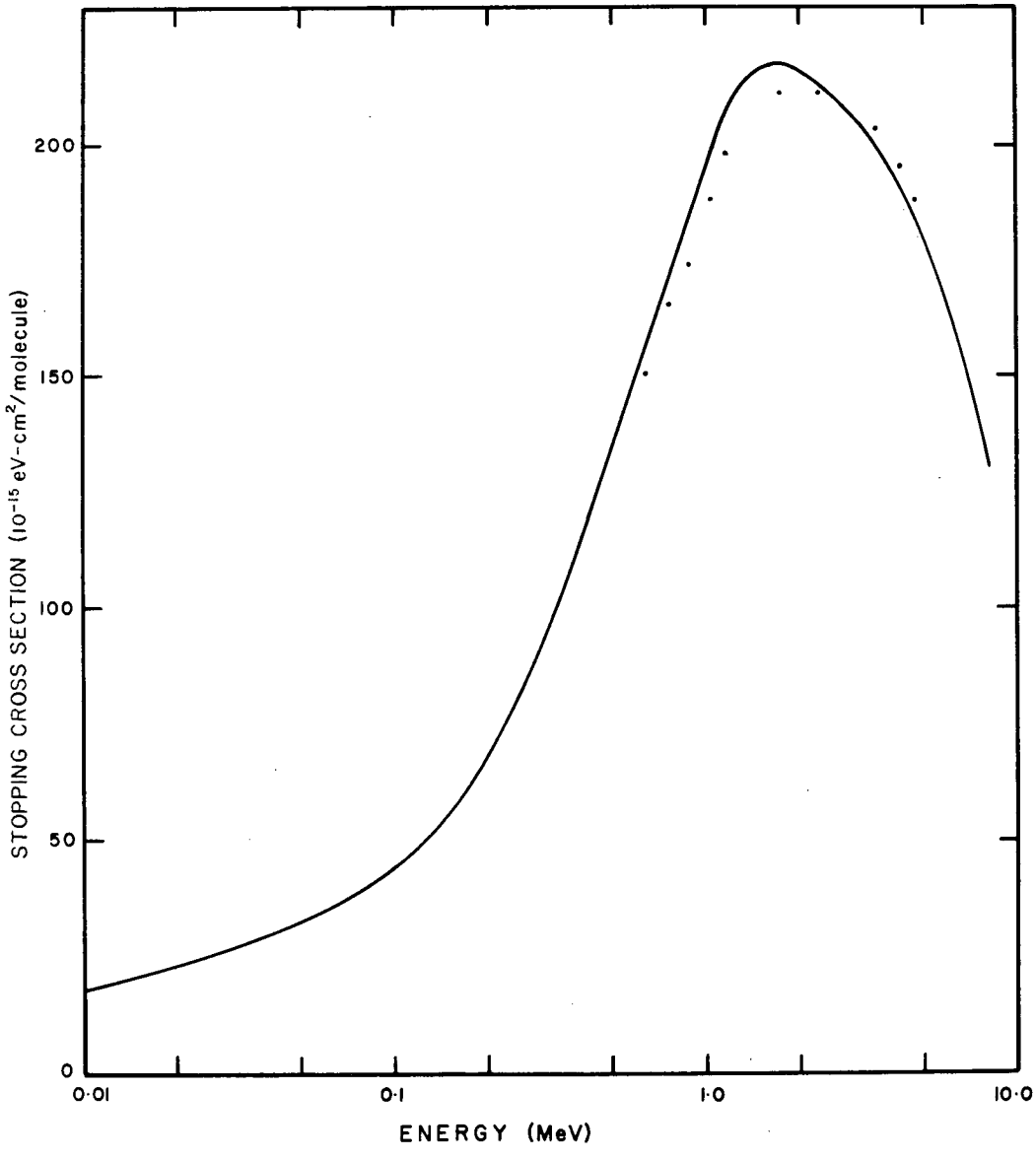
200
150
100
50
0
STOPPING CROSS SECTION ($10^{-15}$ eV-cm$^2$/molecule)
0·01
0·1
1·0
10·0
ENERGY (MeV)

Figure 2.13: Stopping Cross Section for Li Ions in $CH_4$

- • Allison, Anton and Morrison (88)
- × Sidenius (89)
- + Teplova et al (90)

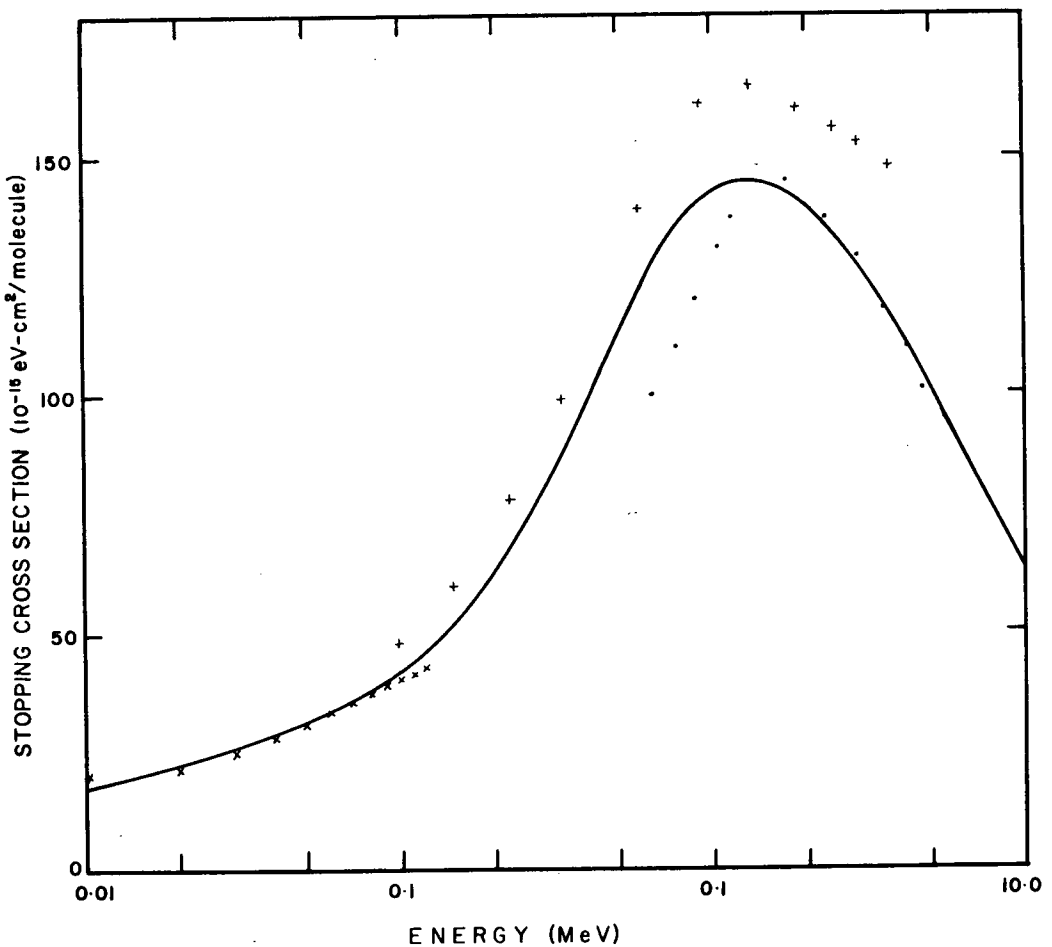
STOPPING CROSS SECTION ($10^{-15}$ eV-cm$^2$/molecule)
150
100
50
0
0·01
0·1
0·1
10·0
ENERGY (MeV)

2.3.3 W-Value Data

The W-value is defined by

$$W = E/N \qquad 2.24$$

where N is the total number of ions created by completely stopping an ion of energy E in the gas. As the velocity of a heavy ion decreases, the W-value increases, going to infinity at the first ionization potential. Based on MacDonald and Sidenius' systematic investigation (98) of ionization in methane for various ions, Dennis (99) has derived an empirical equation to determine the W-value as a function of energy:

$$W(E) = W_\beta \left[1.035 + A(Z)\ (E/M)^{-n(Z)}\right] \qquad 2.25$$

where $W_\beta$ is the W-value for fast electrons, M is the ion mass in amu and E is the energy in keV. The value of n(Z) is roughly 0.5 so $W(E)/W_\beta$ is linear in 1/v (for $v < v_0/2$). For ions having E > 1000 keV/amu, a different equation is used:

$$W(E) = W_\beta \frac{E/M}{(E/M - b)} \qquad 2.26$$

where b is chosen to normalize to equation 2.25 at E/M = 1000 keV/amu. The constants used in this calculation are given in table 2.4.

The Dennis equations are in common use (100, 101, 102, 103). A more recent analytical fit based on the same data set (105) removes the discontinuity in slope at 1000 keV/amu, but does not change the values significantly (102). A comparison of the fitted curve and some experimental data (107, 108, 109, 110) for alpha particles in methane is shown in figure 2.14. The 6 to 10% discrepancy at low energy between the various experiments is also typical of the agreement obtained with other gases (109, 111, 112).

Table 2.4: Constants Used in the Dennis Formula for W-Values

| Ion | Mass (113) (amu) | n(Z) | A(Z) $CH_4$ | A(Z) $CO_2$ |
|---|---|---|---|---|
| proton | 1.00783 | .04902 | .1301 | .0814 |
| alpha | 4.00260 | .5360 | 1.810 | 1.1331 |
| lithium | 7.01600 | .7630 | 3.219 | 2.0151 |

$W_\beta$ = 27.3 for $CH_4$ (114)

$W_\beta$ = 32.9 for $CO_2$ (114)

Figure 2.14: W-Value for Alpha Particles in $CH_4$

o Varma and Baum (107)

+ Bortner and Hurst (108)

× Kuhn and Werba (109)

Δ Jesse (110)

Solid line is the fit of Dennis (91) to the data of MacDonald and Sidenius (98)

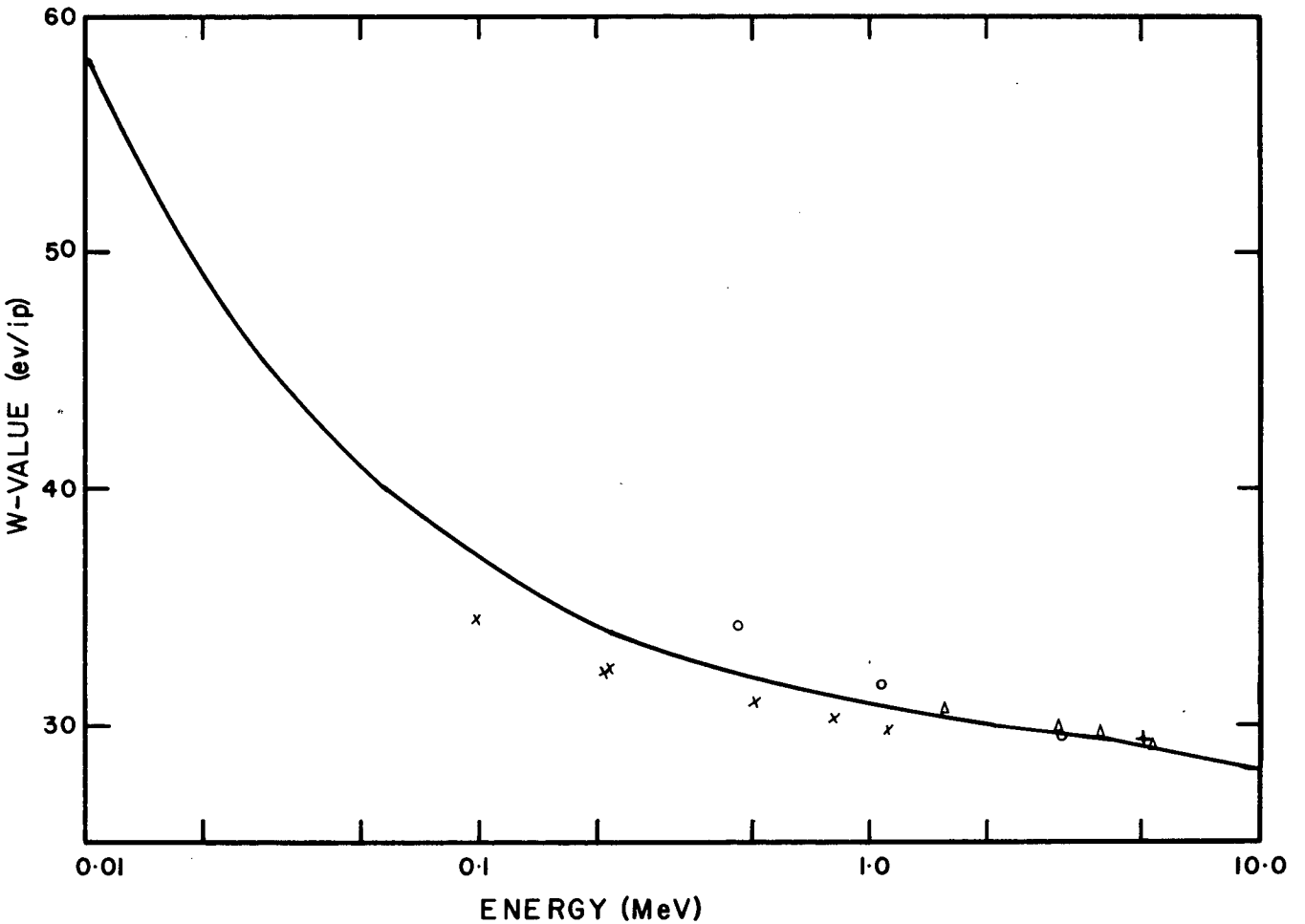
60
50
40
30
W-VALUE (ev/ip)
0·01
0·1
1·0
10·0
ENERGY (MeV)

## 2.4 RESULTS OF THE CALCULATION

The calculation that has been described in section 2.2 has been performed for a carbon cavity of 2 cm diameter filled with either methane or carbon dioxide at various pressures and 22°C. Appendix B contains a summary of the quantities calculated and the equations used. Self-consistency checks built into the computer program indicate that systematic errors in the computation are less than 0.5%.

### 2.4.1 Partitioning the Dose Between the Various Event Types

Figure 2.15 illustrates how the dose is partitioned between the various event types (stoppers, crossers, insiders and starters) for lithium ions released by pion capture in carbon. At very low pressure, all of the dose is due to crossers originating from pion capture in the walls. As the gas pressure is increased, some of the crossers have insufficient energy to traverse the cavity and thus become stoppers. At this pressure, there are also a significant number of pion stars which occur in the gas and whose Li ions have sufficient energy to escape (starters). As the pressure is further increased, the number of gas stars continues to increase, but ions that once were starters now have insufficient energy to escape and become insiders. At very high pressures, there will be no crossers and only the cavity surface will have stoppers and starters present. The partitioning of the dose for lithium exhibits the most variation in the range of chord lengths that are of interest because its mean range is of the order of 1 to 10 $mg/cm^2$. For protons, crossers deposit most of the dose even at the largest chord lengths investigated because the mean range of the protons is $10^3$ - $10^4$ $mg/cm^2$. As shown in table 2.5, 70% of the total kerma is due to the Z = 1 secondaries. Therefore figure 2.16, which shows the partitioning

of the total dose among the four event types, shows less variation than for lithium. It is important to note that for chambers in common use (a 2 cm diameter sphere filled with air at one atmosphere has a mean chord length of 1.6 mg/cm$^2$) only 90% of the star dose results from stars in the wall with secondaries having sufficient energy to be crossers.

Table 2.5: Average Energy and Kerma According to Particle Type (Carbon)

| Particle | E Production Spectrum (MeV) | E Slowing-down Spectrum (MeV) | Energy per Pion Stop (MeV/pion) | Fraction of the Total Kerma |
|---|---|---|---|---|
| p | 23.25 | 34.81 | 10.50 | .383 |
| d | 19.39 | 30.46 | 6.38 | .233 |
| t | 13.97 | 22.60 | 3.07 | .112 |
| $^3$He | 15.66 | 13.13 | .64 | .023 |
| $^4$He | 8.49 | 11.02 | 5.51 | .201 |
| Li | 8.08 | 6.33 | 1.34 | .049 |

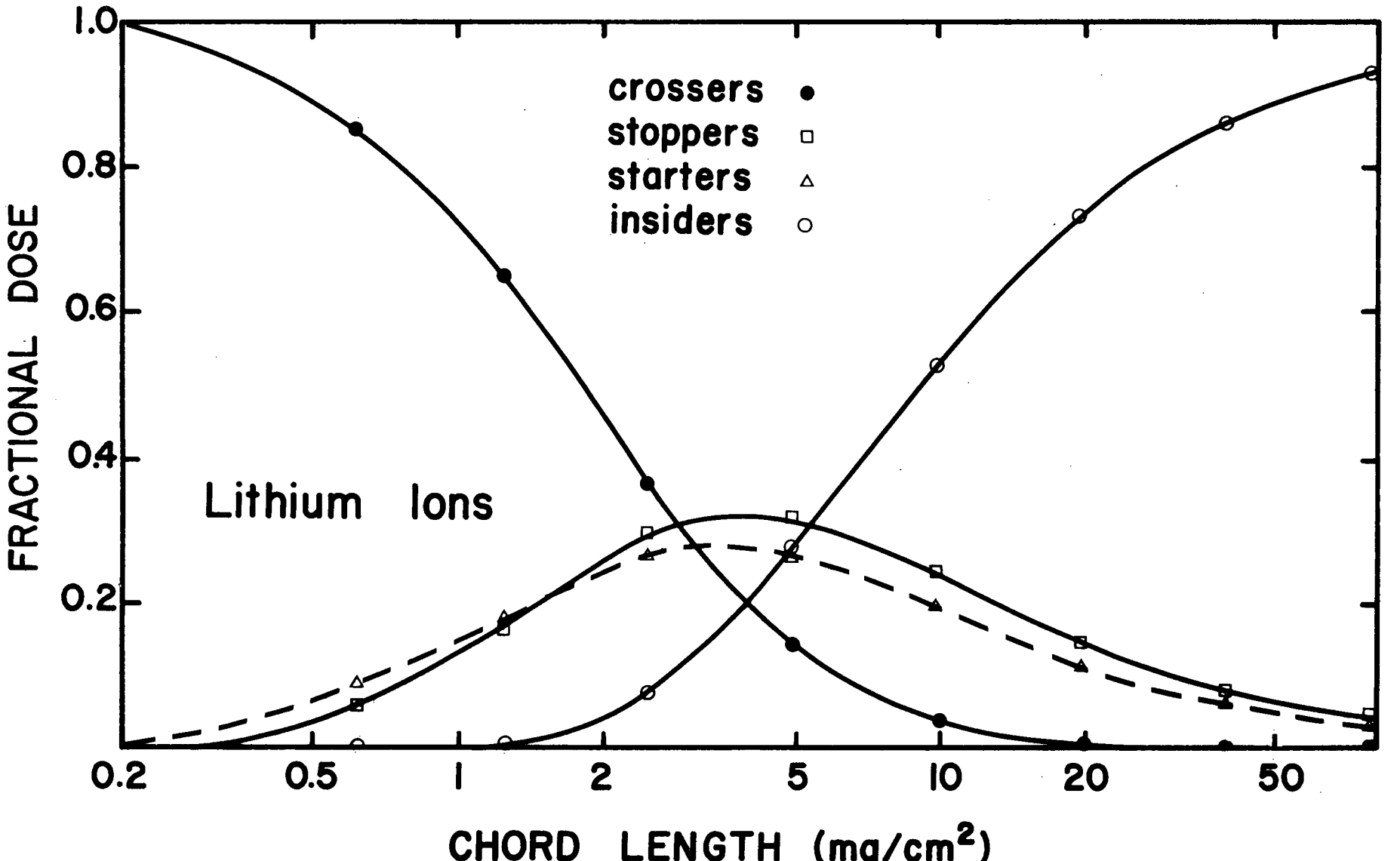


Figure 2.15: Partitioning the Dose Among the Event Types for Li Ions

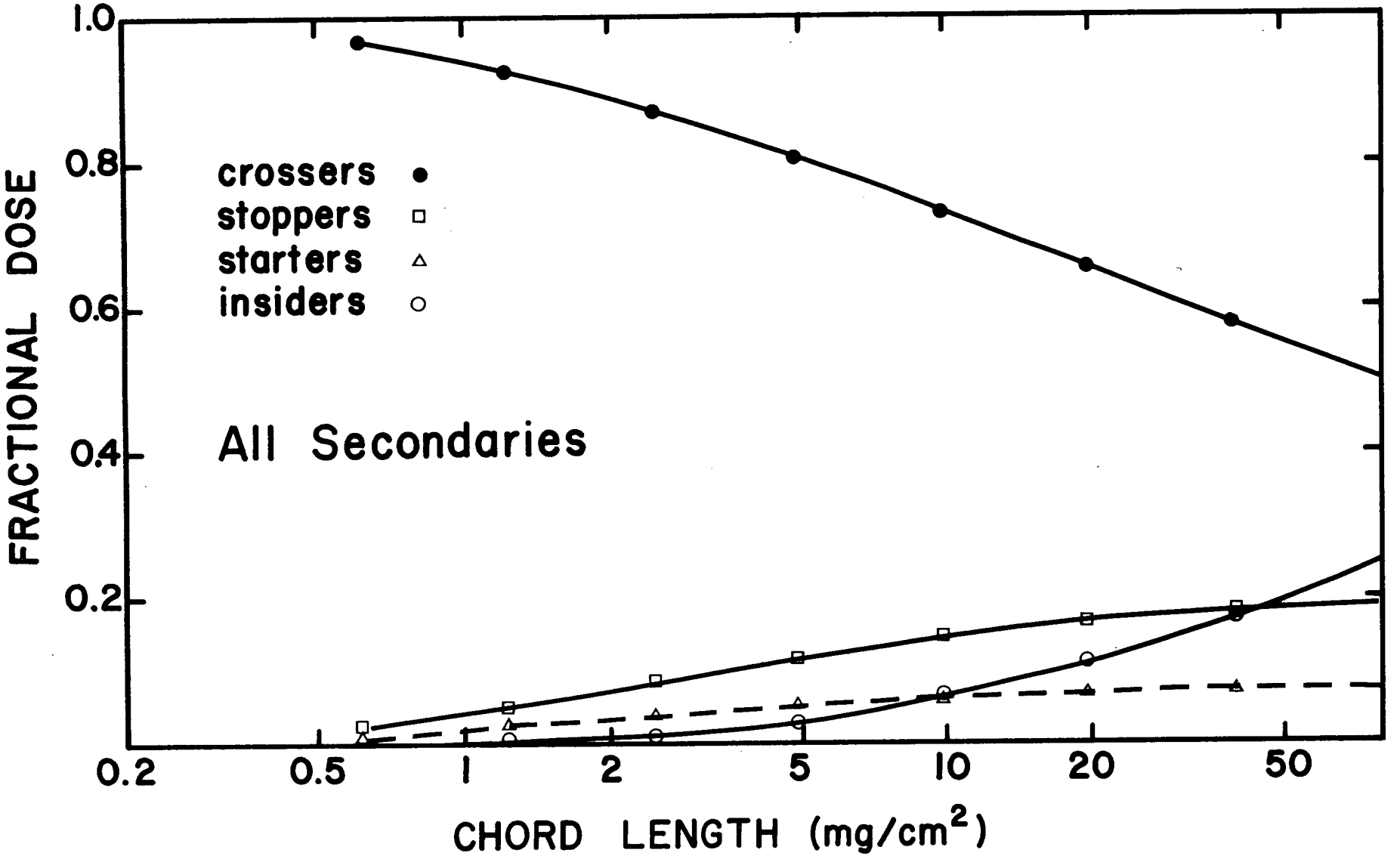


Figure 2.16: Partitioning the Dose Among the Event Types for All Secondaries

2.4.2 W and r for $CH_4$ and $CO_2$ in Carbon Walls

If the quotient of the average W-value divided by the fast electron W-value is defined as

$$u = \overline{W}g/W_\beta \ ,$$

then equation 1.1 can be rewritten as

$$\frac{J}{M} = \frac{1}{u} \times \frac{1}{r} \times \frac{D_{wall}}{W_\beta} \qquad 2.27$$

Since $D_{wall}$ and $W_\beta$ are constants, J/M is proportional to $(ur)^{-1}$. Table 2.6 gives the calculated values of u, r and $(ur)^{-1}$ as a function of pressure for the 2 cm diameter carbon sphere filled with methane gas at 22°C.

Table 2.6: Values of W and r for C-$CH_4$ (2 cm diameter sphere)

| Pressure (100 kPa) | $u = \overline{W}g/W_\beta$ | r | $(ur)^{-1}$ |
|---|---|---|---|
| 0 | 1.0135 | .7384 | 1.3362 |
| 0.25 | 1.0139 | .7357 | 1.3406 |
| 0.51 | 1.0143 | .7337 | 1.3437 |
| 1.01 | 1.0149 | .7329 | 1.3444 |
| 2.03 | 1.0152 | .7358 | 1.3387 |
| 4.05 | 1.0155 | .7409 | 1.3291 |
| 8.10 | 1.0156 | .7494 | 1.3138 |

For convenience, the calculation has been done for a spherical geometry. In order to simplify the chamber construction, it was made of parallel plate design. Therefore, the results of the calculation for the sphere have been compared with the parallel plate geometry at equivalent average chord lengths. For a convex body exposed to a uniform isotropic field of straight infinite tracks, the mean chord length is given by the Cauchy theorem (115, 116) to be

$$\bar{\ell} = 4V/S \qquad 2.28$$

For the sphere, $\bar{\ell} = \frac{2}{3} D$, where D is the diameter, and for the cylinder, $\bar{\ell} = \frac{2h}{1 + h/R}$, where h is the height and R the radius of the cylinder. The pressure of the sphere, $P_s$, whose $\bar{\ell}$ is the same as for the cylinder at pressure, $P_c$, is given by

$$P_s = \frac{3h}{(1 + h/R)\ D}\ P_c$$

For the particular experimental geometry which used a cylinder of height 0.614 cm and radius 1.024 cm

$$P_s = 0.576\ P_c$$

The results of the calculation that have been tabulated in table 2.6 for a 2.0 cm sphere are plotted in figure 2.17 as a function of pressure in an equivalent parallel plate chamber. As was discussed in section 2.3.1.3, there is a further correction related to the stopping density of pions that must be applied to the insiders and starters which is shown in figure 2.3. The values of $(ur)^{-1}$ including the pion stopping density correction are also shown in figure 2.17.

The calculation was repeated for a carbon sphere containing carbon dioxide gas and the results are displayed in table 2.7.

Table 2.7: Values of W and r for C-$CO_2$ (2 cm diameter sphere)

| Pressure (100 kPa) | $u = \overline{W}g/W_\beta$ | r | $(ur)^{-1}$ |
|---|---|---|---|
| 0 | 1.0129 | 1.0346 | .9542 |
| 0.25 | 1.0129 | 1.0407 | .9486 |
| 0.51 | 1.0129 | 1.0470 | .9429 |
| 1.01 | 1.0127 | 1.0587 | .9327 |
| 2.03 | 1.0124 | 1.0760 | .9180 |
| 4.05 | 1.0120 | 1.0994 | .8988 |
| 8.10 | 1.0116 | 1.1260 | .8780 |

The uncorrected and density corrected values of $(ur)^{-1}$ as a function of pressure in an equivalent plate chamber are plotted in figure 2.18.

The pressure dependence of $(ur)^{-1}$ for these gases is quite different. For methane, there is a 0.6% increase between 0 and 1 atmospheres. Since the W-value is independent of pressure (= 0.1%), these changes are due to variation in the value of r. Further, since the calculation treats methane as a pure carbon gas for the purpose of pion capture, these changes in r reflect the conversion of the secondary spectra from the "equilibrium" spectrum characterizing the crossers to the "production" spectrum characterizing the insiders. Carbon dioxide, on the other hand, exhibits a rapid and continuous decrease of 6½% between 0 and 8 atmospheres. In this case, the conversion from the wall "slowing down" spectrum to the gas "production" spectrum is dramatic because of the rather low kerma for carbon dioxide (16.3 MeV/pion due to its oxygen content). In other words, as the pressure

increases, a larger fraction of the captures occur in the gas, but since the energy released to charged secondaries per capture is smaller, the dose decreases.

If we consider the dependence of $(ur)^{-1}$ on pressure after correcting for the perturbation in pion stopping density, the picture changes. The hydrogen in methane increases its stopping power and therefore increases the density of pion stops in the gas. This effect is large and masks out changes in $(ur)^{-1}$ due to changes in the secondary energy spectra. There is a net increase in $(ur)^{-1}$ of 2.3% between 0 and 8 atmospheres. On the other hand, the density correction for $CO_2$ is less than unity and it serves to slightly enhance the decrease in $(ur)^{-1}$ with pressure. There is a net decrease in $(ur)^{-1}$ of 7% between 0 and 8 atmospheres.

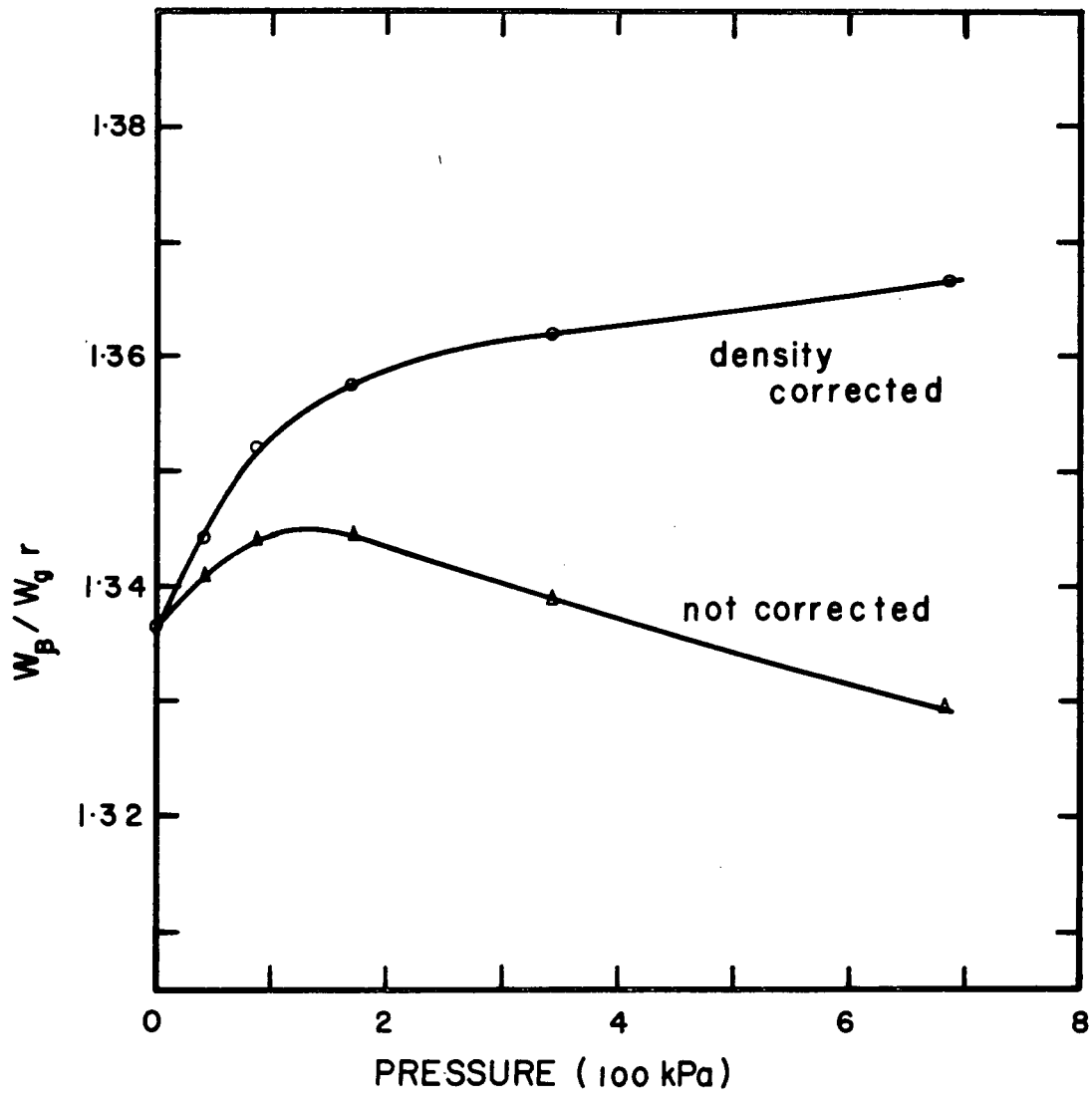


Figure 2.17: $\frac{W_\beta}{\overline{W}g\ r}$ for C-$CH_4$ in the Parallel Plate Chamber

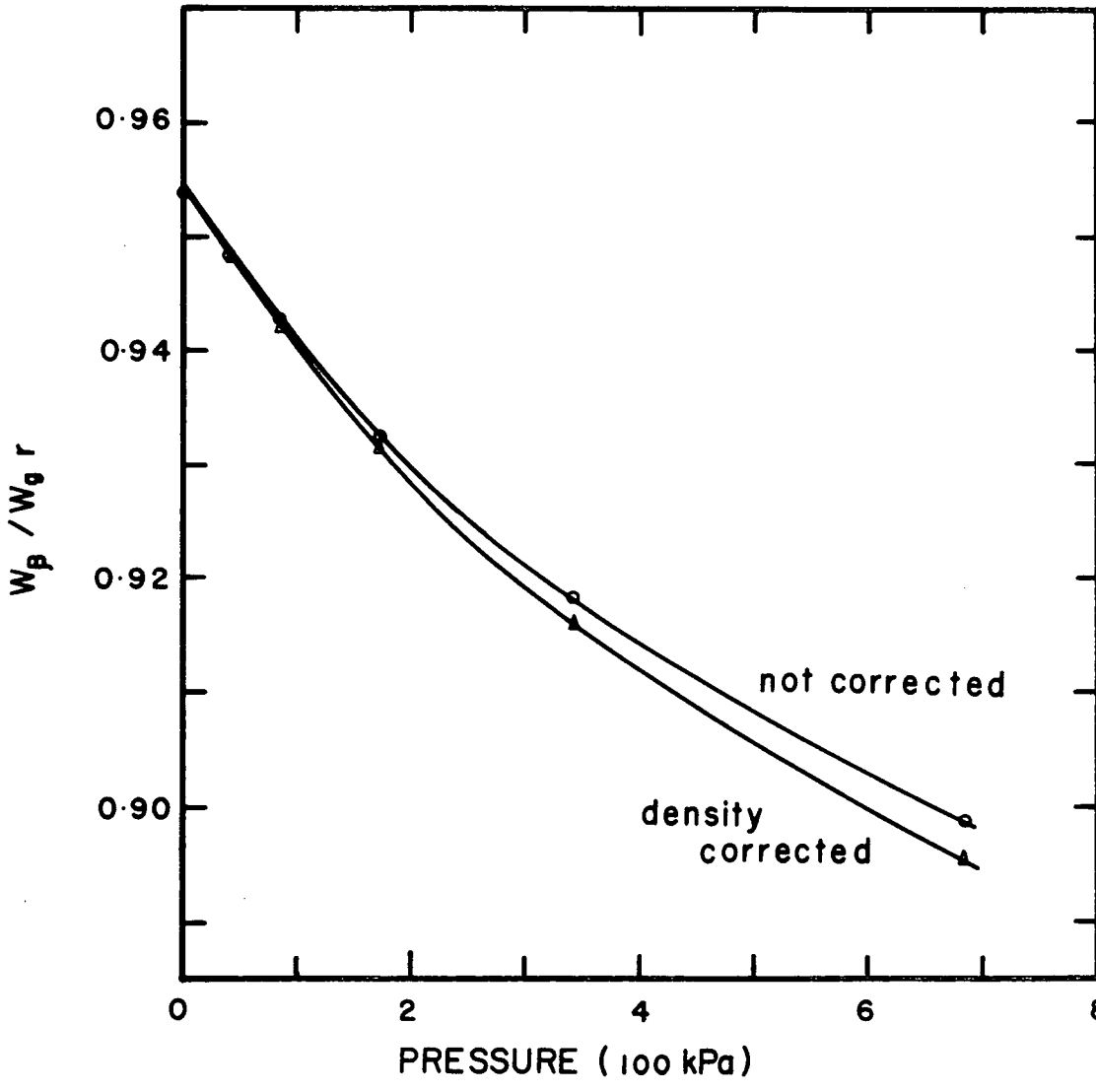


Figure 2.18: $\frac{W_\beta}{\overline{W}g\ r}$ for C-$CO_2$ in the Parallel Plate Chamber

## 2.5 DOSE DEPOSITED BY OTHER PARTICLES

In this section, the expected pressure dependence of the stopping power ratio for electrons and passing pions is calculated and that for neutrons is discussed. Relative to the length of time and effort spent investigating the pion star dose, very little was spent investigating the dose deposited by other particles in the beam. The reason for this was pointed out in section 2.1: investigating the pion star dose was interesting because of its uniqueness and its possible contribution to a deeper understanding of cavity theory. The dose from the other particles is discussed here to indicate what tendencies might be observed for an experimental chamber necessarily exposed to all the beam components.

### 2.5.1 Electrons and Muons

For all charged projectiles moving at relativistic velocities, there is a density effect which reduces the mass stopping power for high densities. In appendix D this Sternheimer density correction has been calculated in order to determine stopping power for electrons in carbon dioxide, methane, and carbon at two kinetic energies: 150 MeV and 130 MeV, an average residual electron energy in the plateau and peak respectively (assuming an incident midline momentum of 180 MeV/c). The stopping power ratio for gas to wall is plotted in figure 2.19 as a function of pressure. For both gases the stopping power ratio shows a 10% decrease between 0 and 8 atmospheres. Therefore, that part of the ionization chamber response (J/M) due to the electron contamination will decrease by 10% (assuming that the electron W-value is pressure independent).

There is also a pressure dependent density effect for the muon

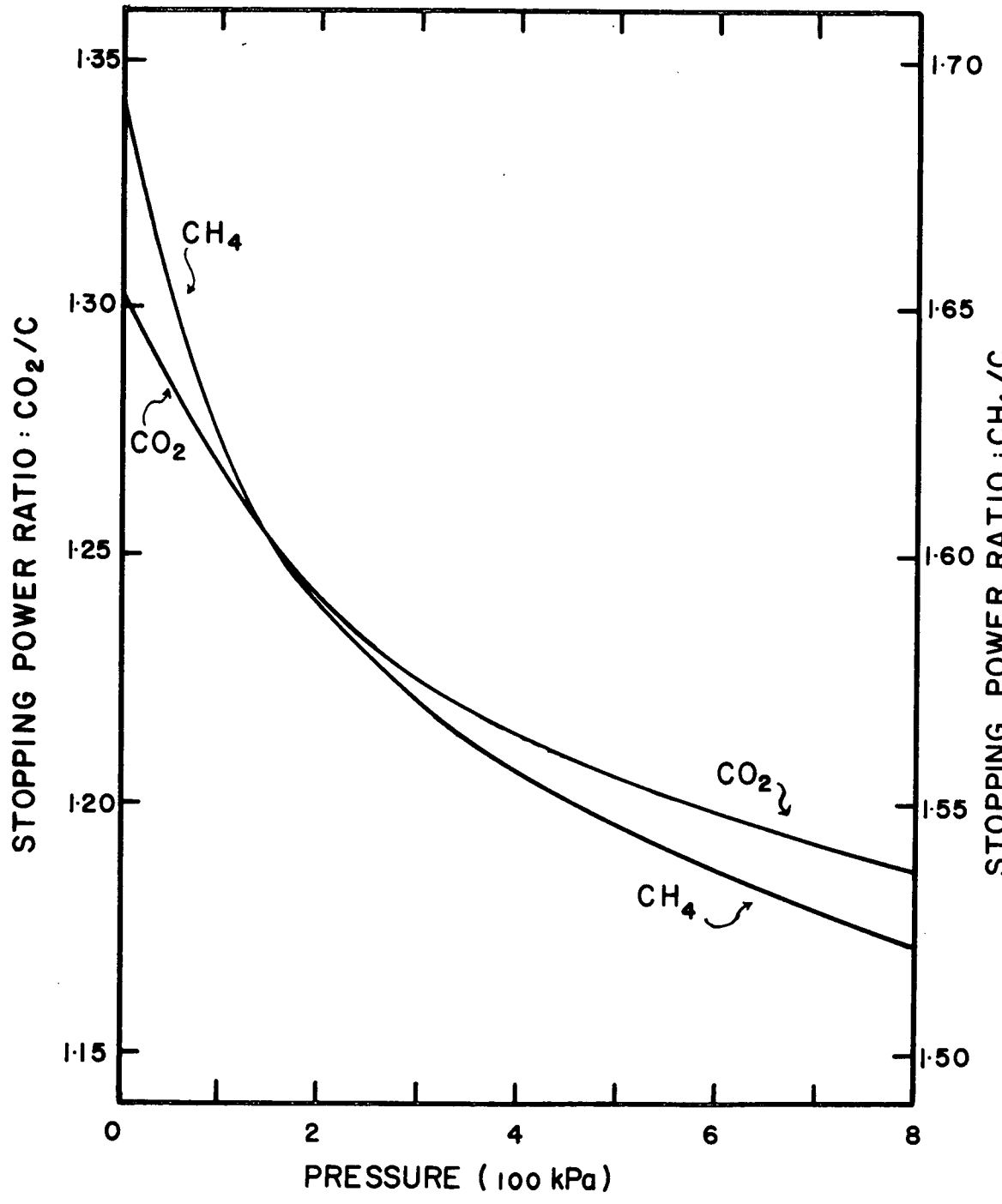


Figure 2.19: Electron Stopping Power Ratio Versus Pressure

contamination which is extinguished at depths greater than 5 $g/cm^2$ because the muon residual kinetic energy has fallen below the energy threshold of 0.874 $M\mu C^2$ = 92.5 MeV (118).

2.5.2. Directly Ionizing Pions

Next, only the dose deposited by the direct interaction between the pions and the atomic electrons is considered. The total dose in a cavity of areal density $\rho L$ exposed to a slowing-down spectrum of pions given by Nr(E) as measured at the cavity is

$$D_{direct} = \int_0^{E_{stop}} \frac{E\ Nr(E)}{\rho L}\ dE + \int_{E_{stop}}^{E_{max}} \frac{\Delta\ Nr(E)}{\rho L}\ dE$$

The first term is due to pions which stop in the cavity. $E_{stop}$ is defined implicitly by $R(E_{stop}) = \rho L$ where R is the range. The second term is the dose due to passing pions. $E_{max}$ is the maximum energy available and governs the width of the stopping peak. The energy deposited by a passer is $\Delta$ given implicitly by $R(E) = R(E - \Delta) + \rho L$. The integral for passers may be subdivided at energy Ea such that for $E > Ea$, the substitution $\Delta = S(E) \cdot \rho L$ is valid where S(E) is the stopping power. This gives

$$D_{direct} = \int_0^{E_{stop}} \frac{E\ Nr(E)}{\rho L}\ dE + \int_{E_{stop}}^{Ea} \frac{\Delta\ Nr(E)}{\rho L}\ dE + \int_{Ea}^{E_{max}} S(E)Nr(E)dE$$

The value of $E_{stop}$ (and hence the relative importance of each integral) will depend upon the areal density. For the extreme case of $CO_2$ in a carbon walled chamber of L = .614 cm and P = 8 atmospheres, $E_{stop}$ = 0.92 MeV, $R(E_{stop})$ = 0.009 $g/cm^2$, Ea = 2.25 MeV and R(Ea) = 0.045 $g/cm^2$. Therefore, at all positions of the chamber except at the distal edge of the stopping

distribution, the dose is dominated by

$$\int_{Ea}^{E_{max}} S(E)\ Nr(E)\ dE$$

and the ratio of dose in wall to dose in gas is given by the stopping power ratio.

For example, consider a chamber located in the plateau at least a distance R(Ea) (= 0.05 g/cm$^2$) upstream from the leading edge of the pion stopping region. Then $Nr(E) \equiv 0$ for $E < E_{min} = Ea$ and hence,

$$r = \frac{\int_{E_{min}}^{E_{max}} S_C(E)\ Nr(E)\ dE}{\int_{E_{min}}^{E_{max}} S_{CO_2}(E)\ Nr(E)\ dE}$$

Further,

$$\frac{S_C(E)}{S_{CO_2}(E)} = 1.03 \pm 0.005$$

for E > Ea, and therefore r is identical to the stopping power ratio independent of the pion energy spectrum, the areal density of the chamber or its location in the plateau.

Next consider the chamber to be located near the dose peak, say 2.5 g/cm$^2$ in front of the distal edge of the stopping peak. Then $E_{max}$ = 22.5 MeV and the relative importance of the three integrals is 4%, 6% and 90% respectively. Even though the contribution to the dose from the first and second integral has started to become significant, the ratio of the dose in carbon to dose in carbon dioxide does not change from 1.03. The corresponding value for methane is 0.74.

In conclusion, the ratio of dose in carbon to dose in gas is not expected to be significantly different from the stopping power ratio.

### 2.5.3 Neutrons and Gamma Rays

Dose deposited by neutrons arising from pion stars is not localized and therefore the fraction of the dose due to neutrons is field size dependent. On the basis of references (119, 120) the neutron dose at the peak for the field size used here is approximately 10% of the charged particle dose (not including electron contamination). The effect of the neutrons is to knock on protons and to disrupt nuclei in much the same way as is done by pion stars. Therefore, as a rough estimate, it is assumed that the absolute value and the pressure dependence of $(ur)^{-1}$ for the neutron dose will be the same as that observed for the pion star charged particle dose.

The gamma ray dose is one to two orders of magnitude smaller than the neutron dose (119) and has therefore been neglected.

## 2.6 SUMMARY

In this chapter it was shown that deviations from the simple Bragg-Gray law are expected. That is, the ionization per unit mass is a function of pressure in the region where the pions stop. Specifically, the ionization per unit mass for carbon dioxide is expected to decrease rather dramatically as the pressure is increased, whereas for methane it is not expected to change very much. This is primarily due to the lower yield of charged secondaries from oxygen compared to carbon which becomes evident at higher pressures since more pions are interacting directly with the chamber gas. Because this phenomenon is oxygen specific, all oxygen bearing species are expected to exhibit the same decrease in ionization per unit mass as the pressure is increased. The perturbation in stopping pion density caused by the difference in stopping power augments the difference in behavior between methane and carbon dioxide.

It was also shown in this chapter that the electron contamination present in a pion beam produces ionization which will exhibit a pressure dependence due to the Sternheimer density effect. Since electrons are present in both the peak and the plateau, a decrease in ionization per unit mass is expected for all gases in both the peak and plateau. The decrease in the total ionization per unit mass for oxygen bearing gases ought to be larger in the peak than in the plateau since both phenomena are present there.

# CHAPTER 3

# EXPERIMENT

## 3.1 INTRODUCTION

In order to determine the dose using an ionization chamber, it is necessary to measure the ionization in a cavity which contains a known mass of suitable gas. The equipment and technique used in making these measurements are described in the first half of this chapter. This description also includes documentation about the operation of the monitor chambers of the biomedical channel to which all dosimetry is referenced.

In chapter two it was shown that the ionization per unit mass is expected to exhibit a decrease as the pressure is increased for carbon dioxide, but it ought to remain fairly constant for methane. Therefore, in the second half of this chapter, the measured ionization per unit mass as a function of pressure is presented for these gases and several others. Good qualitative agreement between these measurements and the calculation confirms the importance of the physical processes described in chapter two.

## 3.2 APPARATUS

Figure 3.1 is a block diagram indicating the various pieces of apparatus.

### 3.2.1 Beam Delivery System

The experiments discribed here were performed on the M8 channel at TRIUMF (121, 122). The channel is 8 m in length and collects pions from the production target at 30° in the forward direction above the proton beam. Two 45° bending magnets are used to bring the pion beam horizontally into the irradiation cave. The momentum blades located at the dispersed focus have an acceptance $\Delta P/p$ = 15% FWHM when fully opened (122). Before entering the water in the dosimetry tank, the beam traverses the end window of the vacuum pipe, the monitor chamber, scintillator 1, the multiwire counter, scintillator 2, and the front window of the water tank. All of this material amounts to an equivalent thickness of 2.24 cm of water.

### 3.2.2 Beam Tune and Dose Profiles

A 500 MeV proton beam at 10 to 12 μA was used to produce pions in the 10 cm beryllium target at station T2. The channel tune #10 provided a midline momentum of 180 MeV/c. This particular target and momentum are used commonly. The electron contamination was measured at the entrance to the water tank by a time-of-flight technique (123, 124) and it was found to be 28 ± 2% of the particle flux. The muon contamination was previously found to be 10% of the flux (123).

The ionization versus depth profile for this tune is shown in figure 3.2. The data was measured using an aluminum walled parallel plate ion chamber filled with methane gas at a pressure of 250 kPa. The chamber had a gap of 0.619 cm and a diameter of 2.049 cm. The depth axis was

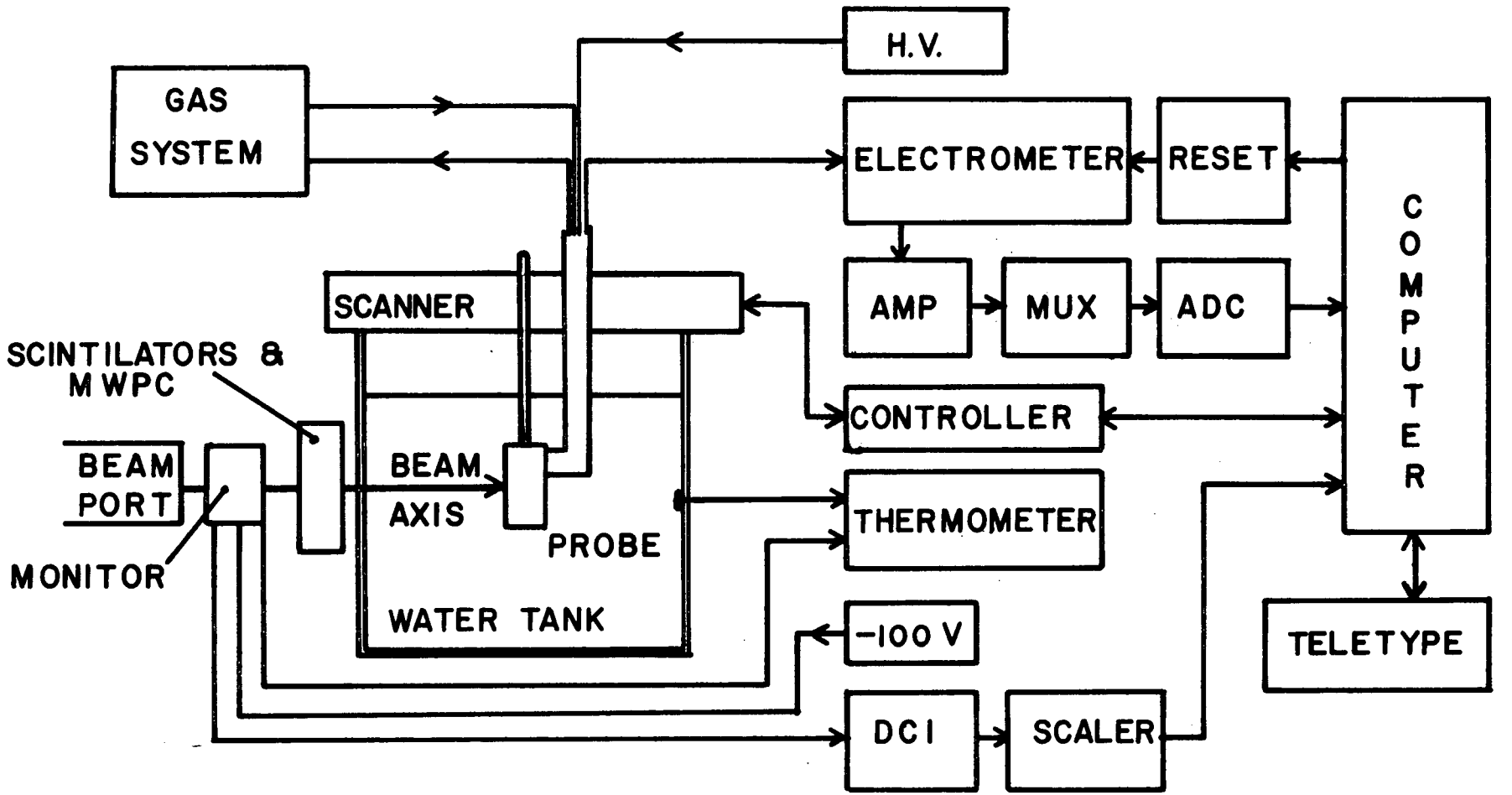


Figure 3.1: Block Diagram of Apparatus

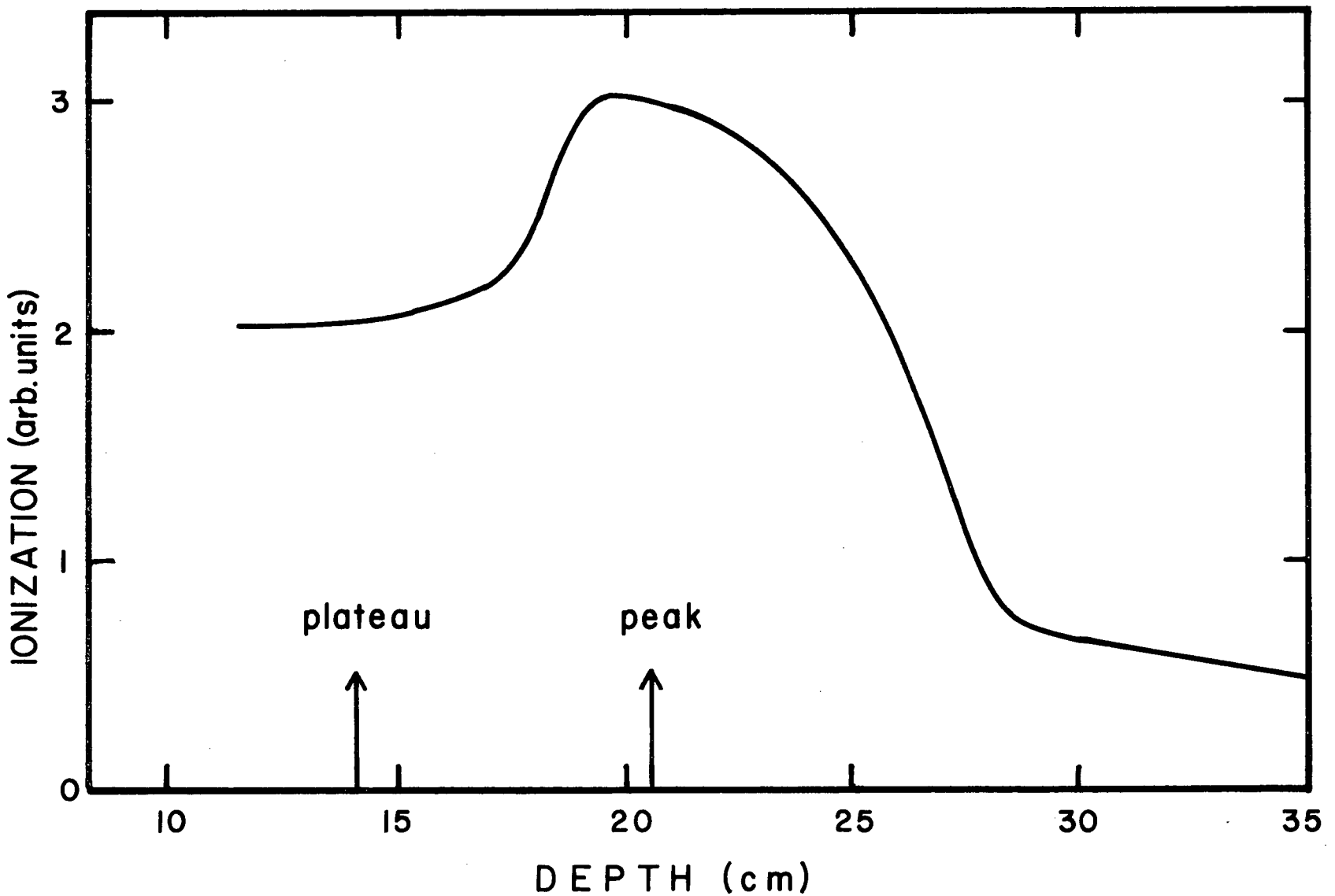


Figure 3.2: Ionization Versus Depth Profile (longitudinal)

calibrated in centimetres of water by comparing a stopping density distribution of FWHM = 1 cm measured with a differential range telescope, whose position had been calibrated by direct measurement, to the corresponding ionization curve measured with a nominal 1 mm gap.

Such a calibration procedure assumes that the ionization and stopping curves are coincident and that the effective centre of the chamber is located right at the front surface of the parallel plate chamber. This latter assumption is valid in the plateau region where the radiation is primarily normally-incident, but not in the peak region where the pion star products are isotropic. Here, the effective centre of the chamber is shifted towards the centre of mass of the gas (1 - 2 mm). The effect of this shift is small enough that it can be ignored. The positions of measurement in the peak and plateau are indicated by arrows in figure 3.2.

Orthogonal cross scans measured at the peak are shown in figure 3.3. It can be seen that the full width at 80% is 9.9 cm vertically and 8.6 cm horizontally. A field which is large compared with the 2 cm diameter collector was chosen so that the dose which would ordinarily be provided by secondaries from the side walls will instead be replaced by dose from secondaries originating in the front and back face. The 5½% horn visible on the horizontal scan is due to second order aberrations in the beam optics.

In order to extract the dependence of J/M on pressure for the star dose alone, it is necessary to separate the dose into its various components according to particle type: electron dose, muon dose, dose due to direct ionization by pions, star dose, and dose due to in-flight interactions. The separation for this tune is shown in figure 3.4.

Consider the plateau region first. The percentage dose due to in-flight interactions was taken from the experiment of Nordell et al (125),

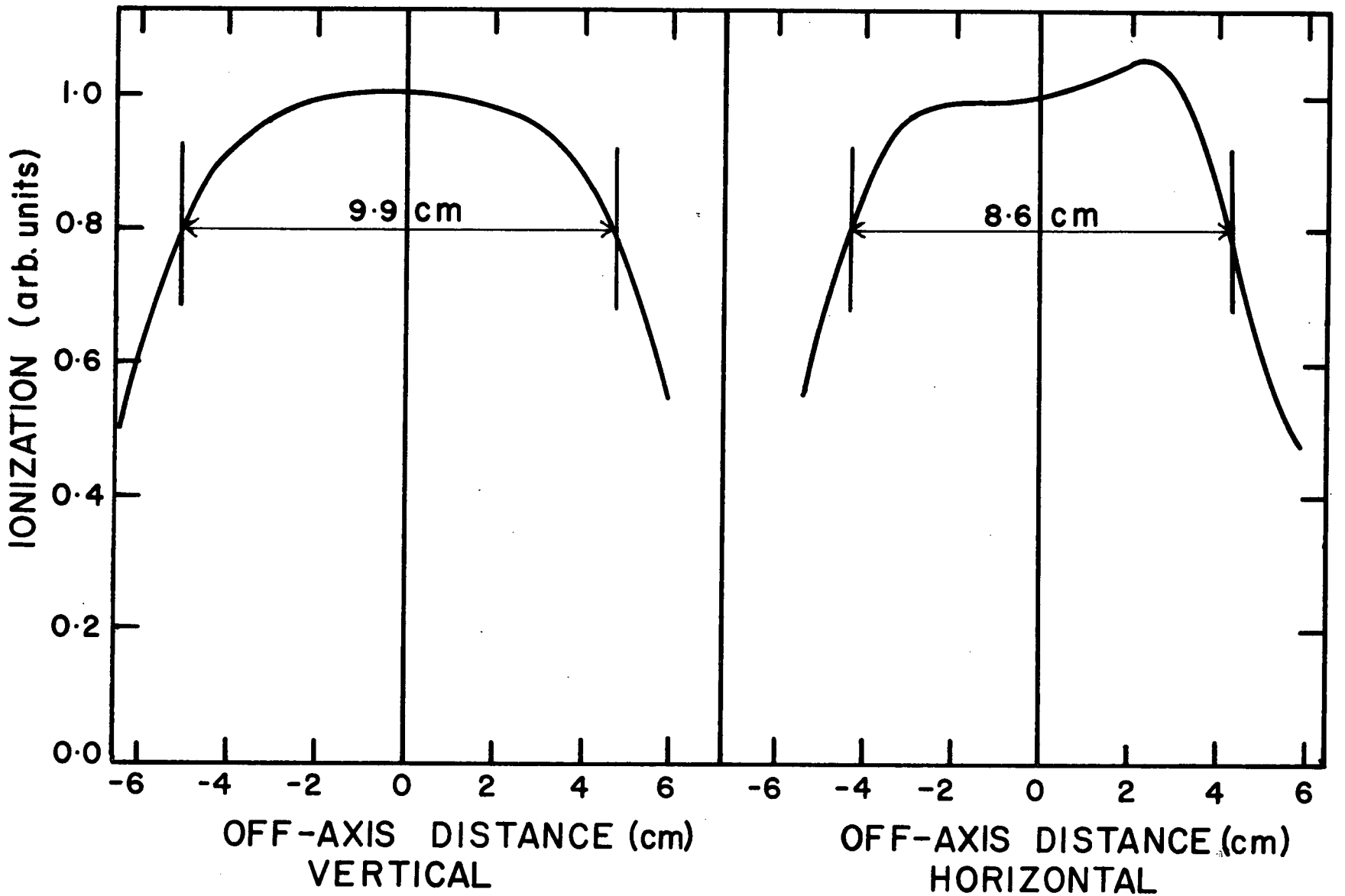


Figure 3.3: Cross Scans at the Peak

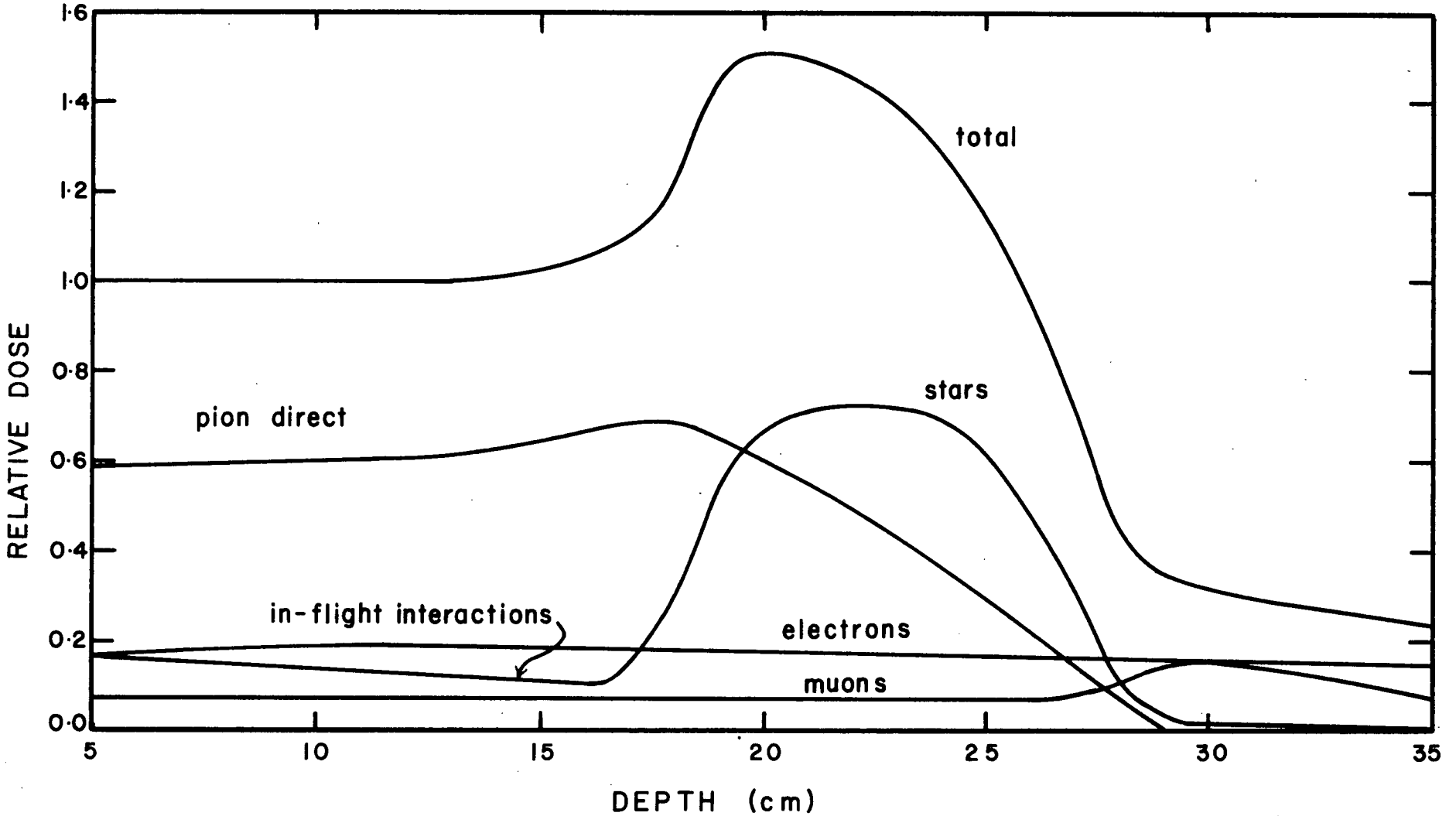


Figure 3.4: Dose by Particle Type

whose values were about twice as large as calculated by Monte Carlo techniques (126). This latter reference (126) was used to fraction the rest of the plateau dose between the direct pion dose and the dose due to contaminating muons plus electrons. The e + μ contamination in the calculation was 23% + 14% = 37%, which is comparable to tune #10 with 28% + 10% = 38%. The contaminant dose was further divided between electrons and muons using the calculation of Alsmiller (127) as a guide to the shape of the electron curve, the calculation of Turner (126) as a guide to the shape of the muon curve, and the experimentally determined ratio of electrons to muons. This completes the separation of the dose in the plateau. This picture is consistent with what was expected on the basis of combining the measured particle flux with estimated stopping powers and including the measured (124) in-flight interaction at 1.6%/cm.

The dose in the peak region can be separated between direct pion ionization and stars. The star dose is proportional to the pion stopping density which was determined by the charge collector technique. This method (5) is described in appendix A. On the basis of the data from Turner (126) and Nordell (125) for narrow momentum bites, the percentage of the total dose which is attributed to stars was set to 50% at the star dose peak. Finally, the star dose plus contaminant doses were subtracted from the total to yield the direct ionization dose. This method of fractioning the dose yields the correct ratio for the energy contributed by passing pions divided by the energy contributed by stars. The fraction of the dose by particle type at both irradiation positions is given in table 3.1. The dose due to neutrons is included with the stars and is responsible for the small star dose component extending into the tail region.

Table 3.1: Percentage of the Dose by Particle Type

| | Plateau (%) | Peak (%) |
|---|---|---|
| pions (direct) | 63 ± 5 | 37 ± 8 |
| in-flight | 11 ± 4 | - |
| stars | - | 46 ± 10 |
| electrons | 19 ± 3 | 12 ± 2 |
| muons | 7 ± 2 | 5 ± 2 |

This completes the description of the beam tune and dose profiles. Those parameters of this particular beam which could be measured directly were combined with calculations and experiments from the literature to provide as complete and accurate a characterization as possible at present. Microdosimetric measurements (128) are consistent with this description.

### 3.2.3 Monitor Chamber

All experiments on the M8 channel requiring a proton production current of more than 1 μA are normalized to the ionization produced in a transmission monitor chamber. This chamber was an integral part of this experiment, and it will be used to determine the patient dose during clinical trials. It was essential therefore that this device and its operation be thoroughly understood.

3.2.3.1 Construction

The monitor chamber is of the transmission type with nine aluminized mylar foil electrodes of thickness 0.81 mg/cm$^2$ arranged as shown in figure 3.5. There are six chambers in total. The ones labelled "B" and "T" are of symmetric design and are identical. "T" was the one used throughout this experiment. During patient irradiation "B" will be used as a backup monitor. Foil "Q", which has been etched to make one chamber in each quadrant, is used to monitor beam drift.

Each foil was stretched between two snap together rings with an open space of 18 cm diameter. The deflection at the centre of a tightly stretched foil did not exceed 1 mm when supporting a weight of 10 g. Electrical contact to the foil was made by a copper wire soldered to the ring and then to a BNC connector at the casing. The rings were held in place by a set of three teflon insulators which rode on guide posts and which determined the relative spacing between foils. The calibration change as a result of complete disassembly was typically 1%. The monitor was mounted on the pole faces of the last quadrupole, Q5, by means of electrically insulating nylon feet.

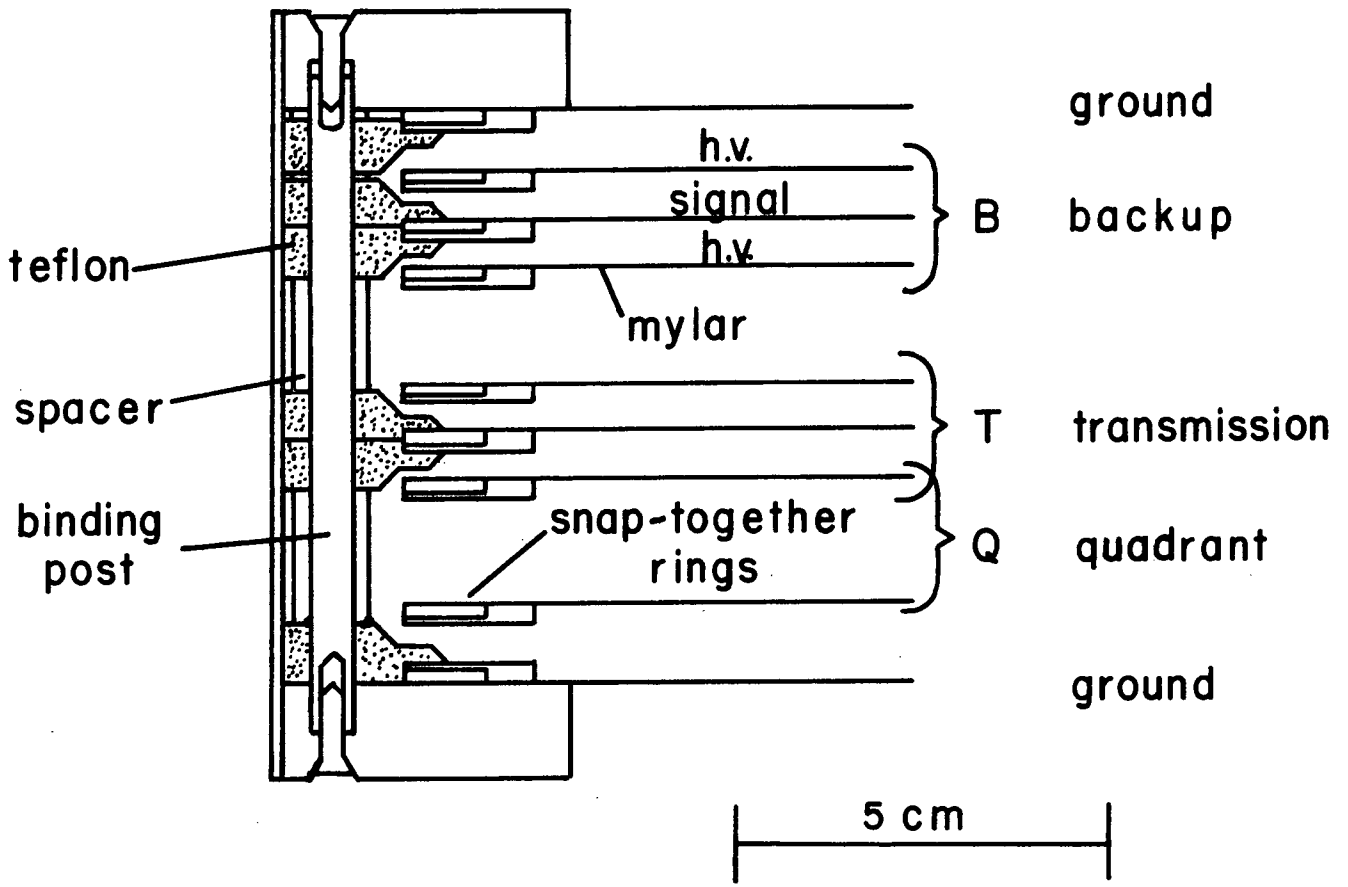


Figure 3.5: Schematic Diagram of the Monitor

3.2.3.2 Operation

The chamber was air-filled and open to the atmosphere with two 2 mm diameter ports. The pressure was measured with a precision mercury barometer (Princo) located near the control console. The temperature was monitored by a surface probe thermistor (YSI T2630) attached to the aluminum casing. Chamber readings were corrected to 22° C and standard pressure (1 atmosphere) in the data acquisition program according to

$$\text{equivalent monitor counts} = \text{specified monitor counts} \times \frac{273+T}{273+22} \times \frac{1}{p(\text{atmospheres})}.$$

The temperature varied between 26.3 and 31.9 °C and the pressure varied between 742 and 767 mm during a four month experimental period.

The chamber output current was integrated by a digital current integrator (Ortec model 439). The read sequence is described in section 3.2.5. Typically, for a proton current of 10 μA, 20 pulses of $10^{-10}$ C/pulse were counted in 9½ seconds ($2.1 \times 10^{-10}$ A).

There was no observable polarity effect. An investigation of saturation for pions at low rates ($0.1 \times 10^{-10}$ A) and for X-rays at high rates ($16 \times 10^{-10}$ A) indicated that the saturation current was 0.25% higher than the current obtained at the usual operating voltage (100 Volts).

When the channel was used with positive pions, an absorber was required to stop the low energy proton contamination which otherwise produced about 100 times the ionization caused by the passing pions, muons, and electrons.

3.2.3.3 Calibration versus particle flux

Some preliminary dosimetry measurements had been taken with the channel tuned at midline momentum 148 MeV/c. When the momentum was changed to 180 MeV/c as a routine, it became necessary to investigate the momentum dependence of the monitor chamber response per incident particle in order to compare with the earlier measurements. At that time, the primary proton current was of the order 1 μA and so the dead time correction for coincidences in scintillators 1 and 2 was less than a few percent. The chamber response per 1.2 coincidence versus midline momentum (full momentum bite) is shown in figure 3.6. The response per coincidence has a peak at 110 MeV/c. As the momentum is decreased from the peak, the electron fraction of the beam increases (123) and since the electrons have a lower stopping power than the pions, the response per particle decreases. On the other hand, as the momentum is increased from the peak, the pion fraction of the beam increases, and since the pions have a lower stopping power, the higher their momentum, the chamber response per particle decreases again.

The calibration of the chamber depends on the separation between the scintillators and the chamber. This is caused by pion in-flight decay to muons, most of which come off at a laboratory angle of about 14°. These muons can miss the scintillators, causing the chamber response per 1.2 coincidence to increase (see figure 3.7).

It is not possible to test the dose rate response of the chamber over a very large range of rates because at proton currents less than 1 μA, electrical leakage in the monitor is a significant fraction of the signal, and at proton currents larger than 1 μA dead time for the 1.2 coincidence is excessive. The dose rate response was linear for 100 keV X-rays up to the maximum rate investigated which was equivalent to a 75 μA proton current.

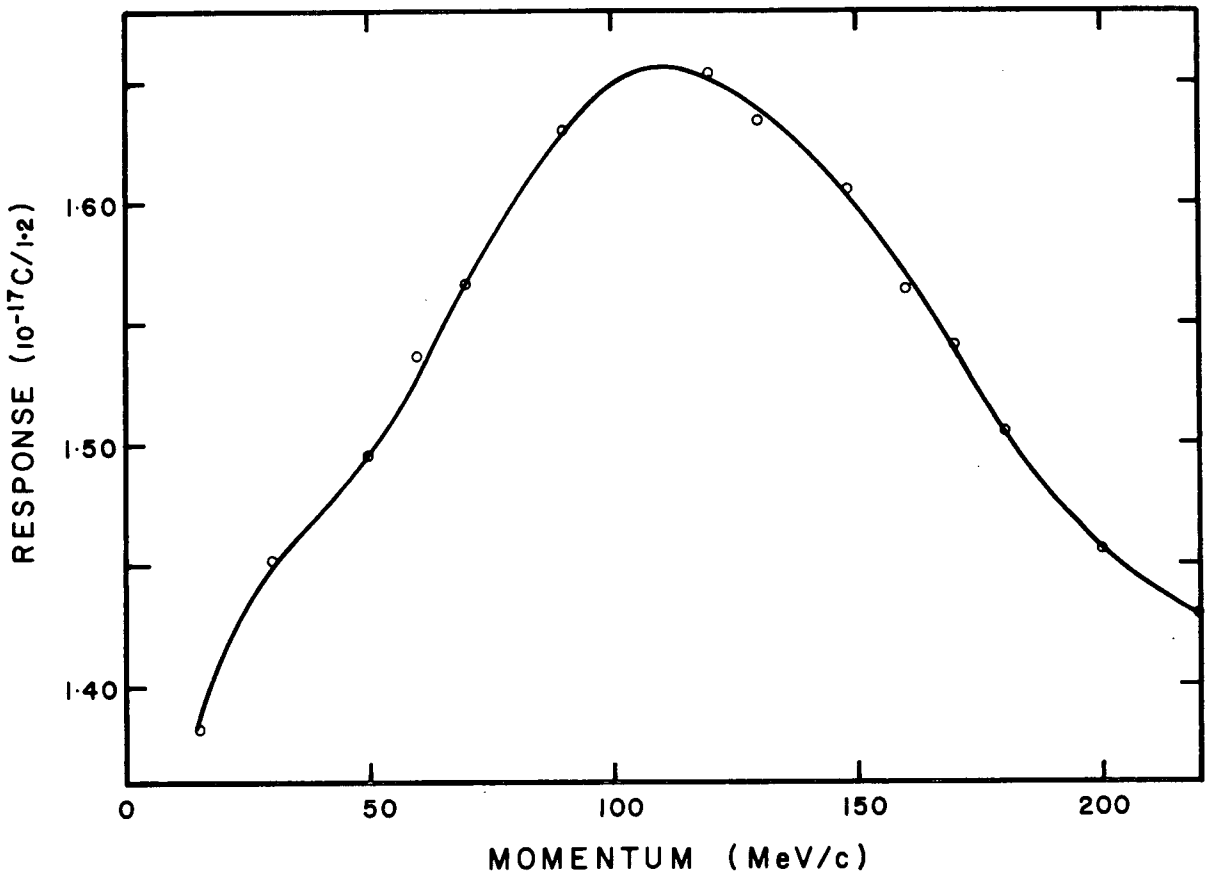


Figure 3.6: Transmission Chamber Response Versus Momentum

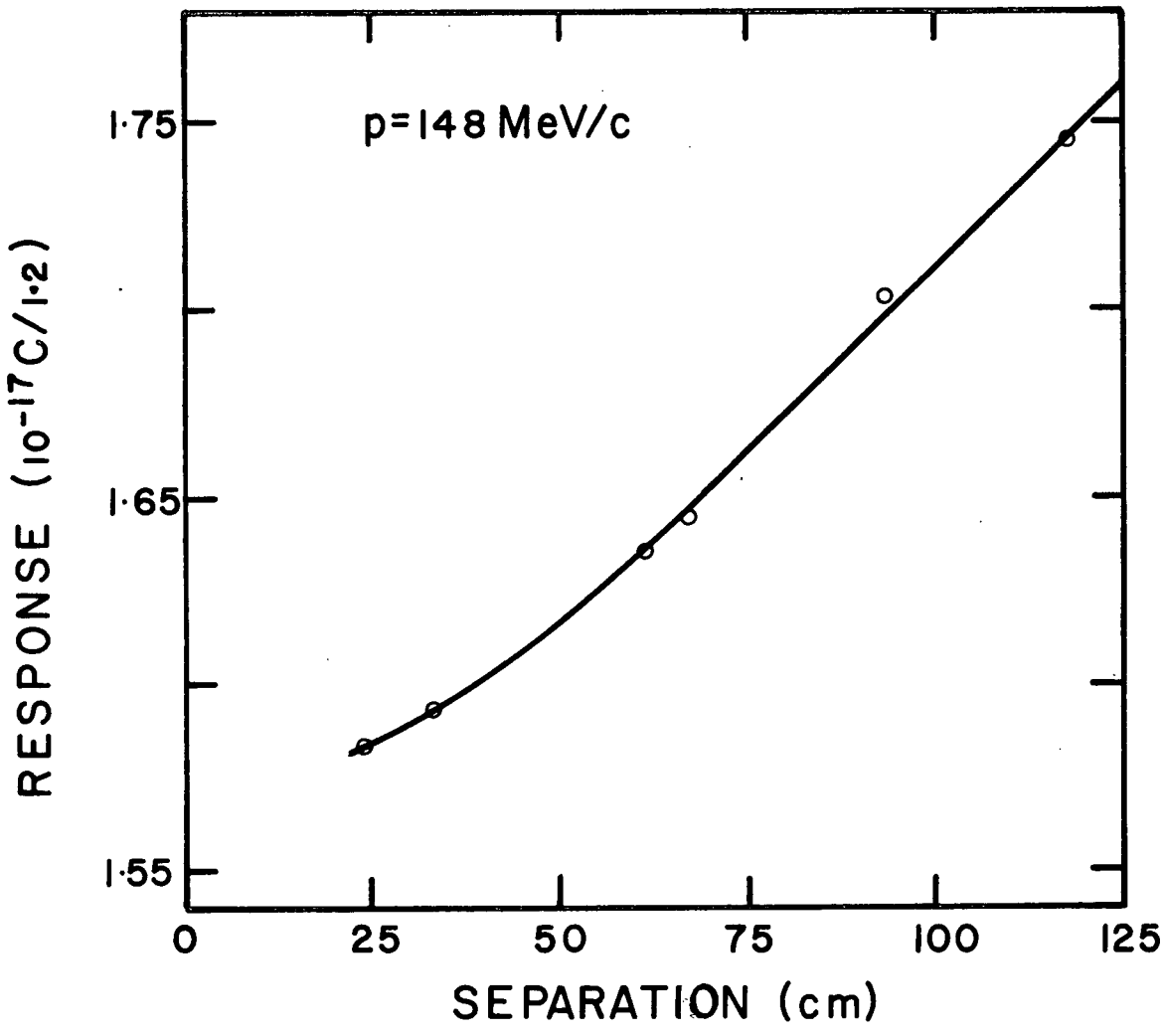


Figure 3.7: Transmission Chamber Response Versus Separation

It has been noticed at the termination of high current tests ($I_p$ = 100 μA) that the monitor appears to be detecting a radioactive background which decays with a half life of the order of 10 minutes. This could be due to the build up of radiation induced positron emitters $^{15}O$ ($T_{1/2}$ = 2.1 m), $^{13}N$ ($T_{1/2}$ = 10.0 m) or $^{11}C$ ($T_{1/2}$ = 20.5 m) inside the monitor chamber. This decaying signal is insignificant in comparison to the beam signal, but it is significantly larger than the usual chamber leakage.

This completes the discussion of the monitor chamber. Throughout the experiments the chamber operated reliably and was reproducible at the ± 1% level.

### 3.2.4 Parallel Plate Ionization Chamber

The parallel plate chamber design was selected for the measurement of dose in the phantom because of its ease of construction and flexibility in exchanging electrodes. As well as eliminating leakage from the high voltage to the collector, the guard ring reduces the problem of electric field rounding at the edges and thereby gives a well defined volume.

#### 3.2.4.1 Construction

A schematic cross section of the ion chamber is shown in figure 3.8. The outer casing is made of aluminum and is held together by six brass rods. The casing could be disassembled to exchange or remove the spacer rings which had thicknesses of 5 mm and 10 mm in order to provide nominal gaps of 1, 6 or 11 mm. Electrodes of various materials and sizes were available as shown in table 3.2. The electrodes were thick enough that all secondaries from stars in the insulator (except for the most energetic protons) would be stopped in the electrodes with the result that the cavity viewed a slowing down spectrum

Figure 3.8: Parallel Plate Ionization Chamber Construction

1. Spring loaded contact to H.V. electrode
2. H.V. plate
3. Polystyrene insulator for H.V. plate
4. Aluminum face plate
5. Nylon screw
6. Rubber O-ring
7. Body ring
8. Space ring (5 mm)
9. Gas flow groove; gas inlet and outlet are not shown
10. Back plate
11. Guard ring
12. Collector
13. Collector screw
14. Polystyrene insulator for signal plate
15. Connector plate
16. Water proof conduit

This view of the electrical connections illustrates the principle of the method for electrical feed through. In actuality, both the signal and high voltage leads were located at the same radial distance as shown here for the H.V. lead. The lead (not shown) which made contact between the guard ring and connector plate was spring loaded.

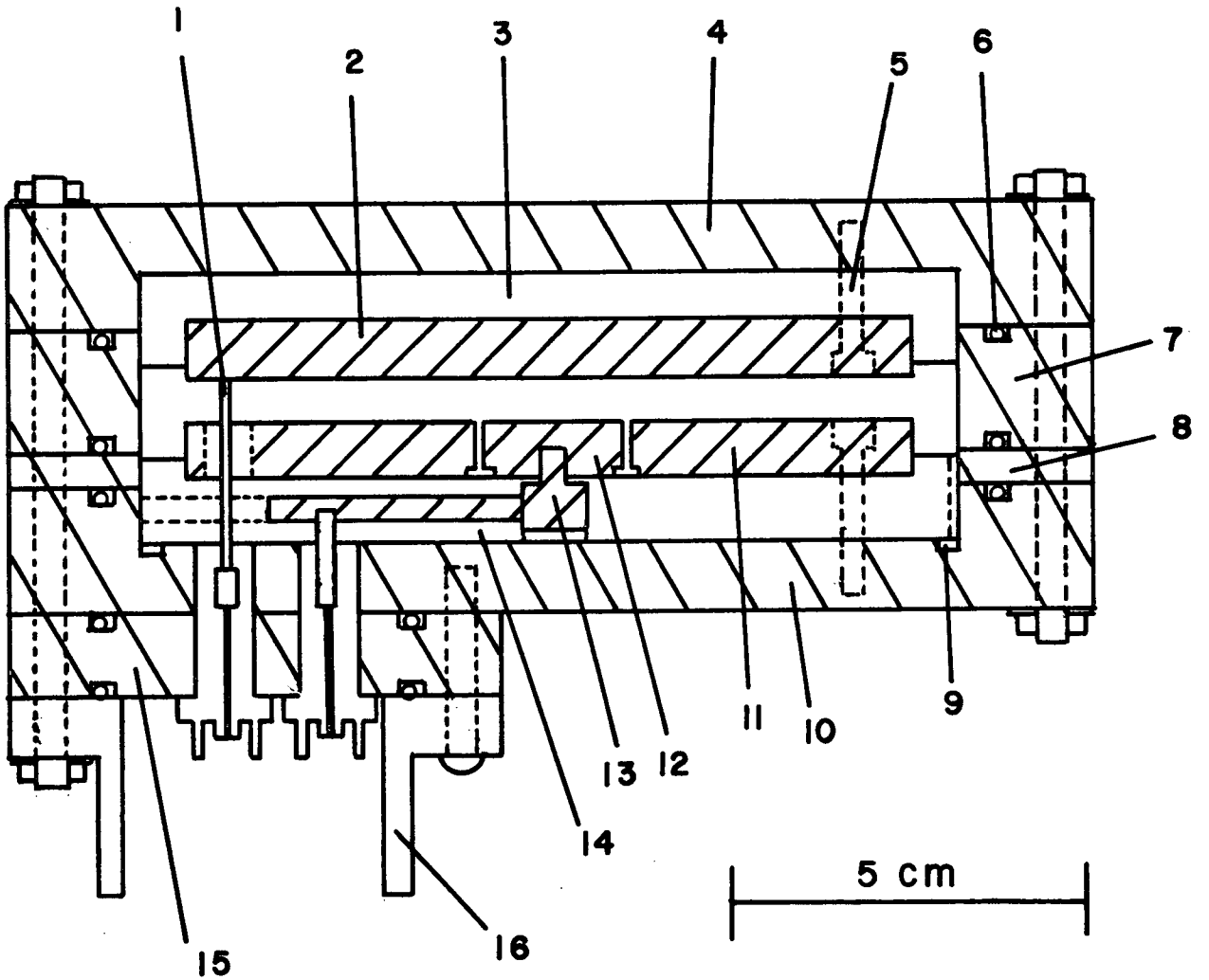
1
2
3
4
5
6
7
8
9
10
11
12
13
14
15
16
5 cm

which is characteristic of the electrode material only. The outer diameter of the guard extended to where the dose was less than 50%.

Electrical connections were made through a water proof conduit fixed to the back plate. The connectors were BNC type with ceramic-to-metal seals and rubber o-rings (Kings Electronics M39012/24-0002). The high voltage lead was spring loaded and the connection to the signal lead was made with a tapered pin. Care was taken to fill the space around the leads with polystyrene insulation to prevent arcing around the high voltage lead and to avoid creating any secondary chamber within the case. In order to eliminate a large polarity effect, a 0.18 mm thick strip of cellulose acetate insulation was inserted into the space between the guard ring and collector. Without it, the polarity effect was large because the electrometer held the collector at approximately +100 mV with respect to the guard ring, thus creating a secondary ion chamber.

Table 3.2: Electrode Materials and Configuration
(the gap and diameter are independently selected)

| Material | Density ($g/cm^3$) | Impurities | Gap (mm) | Diameter** (mm) |
|---|---|---|---|---|
| Carbon | 1.786 ± .015 | .06% (130) | 6.14 ± .02 | 20.47 ± .03 |
| TE A150 plastic | 1.125 ± .007 | * | 6.37 ± .02 | 21.03 ± .03 |
| Aluminum | 2.714 ± .017 | .5% (131) | 6.19 ± .02 | 20.49 ± .03 |
| | | | 1.17 ± .04 | 50.47 ± .04 |
| | | | 11.17 ± .05 | 10.53 ± .03 |

* TE A150 plastic is a mixture widely used in neutron dosimetry whose elemental composition has recently been documented (129): (percent mass) H 10.33, C 76.93, N 3.30, O 6.94, F 1.14 and Ca 1.37.

** Effective diameter is the mean of the collector diameter and the guard ring opening.

3.2.4.2 Gas delivery system

The gas inlet and outlet were connected by grooves so that the gas was forced to flow from one side of the chamber to the other passing over the collector. Although the chamber was not used with continuous flow, this arrangement provided efficient flushing. Rapid approach to the equilibrium pressure was provided by ¼" polyflo tubing coupled to connectors threaded to the back plate and located alongside the electrical connectors. A schematic diagram of the system is shown in figure 3.9. The gas cylinders, gauges and valves were located near the central console about 8 m from the chamber.

The system was usually evacuated when not in use. This was particularly important for the carbon electrodes which were very efficient at adsorbing gases. Before taking data with a new gas, the system was alternately filled and evacuated three times. Readings were usually taken starting at low pressures. This procedure was varied occasionally to look for systematic errors, which were never observed.

Three 6" diameter precision gauges (Matheson) on the outlet port were used to measure pressure in the ranges 0 - 760 mm absolute, 0 - 30 psig and 0 - 100 psig. Corrections for gauge non-linearity were made after calibration using a mercury manometer. In order to determine the absolute pressure, the atmospheric pressure was measured with a precision mercury barometer (Princo). The uncertainty in pressure was ± 1% except at the lowest pressure (15 kPa) where it was ± 2%.

The various gases used, their densities (132) at 22°C and the manufacturer's stated purity are shown in table 3.3.

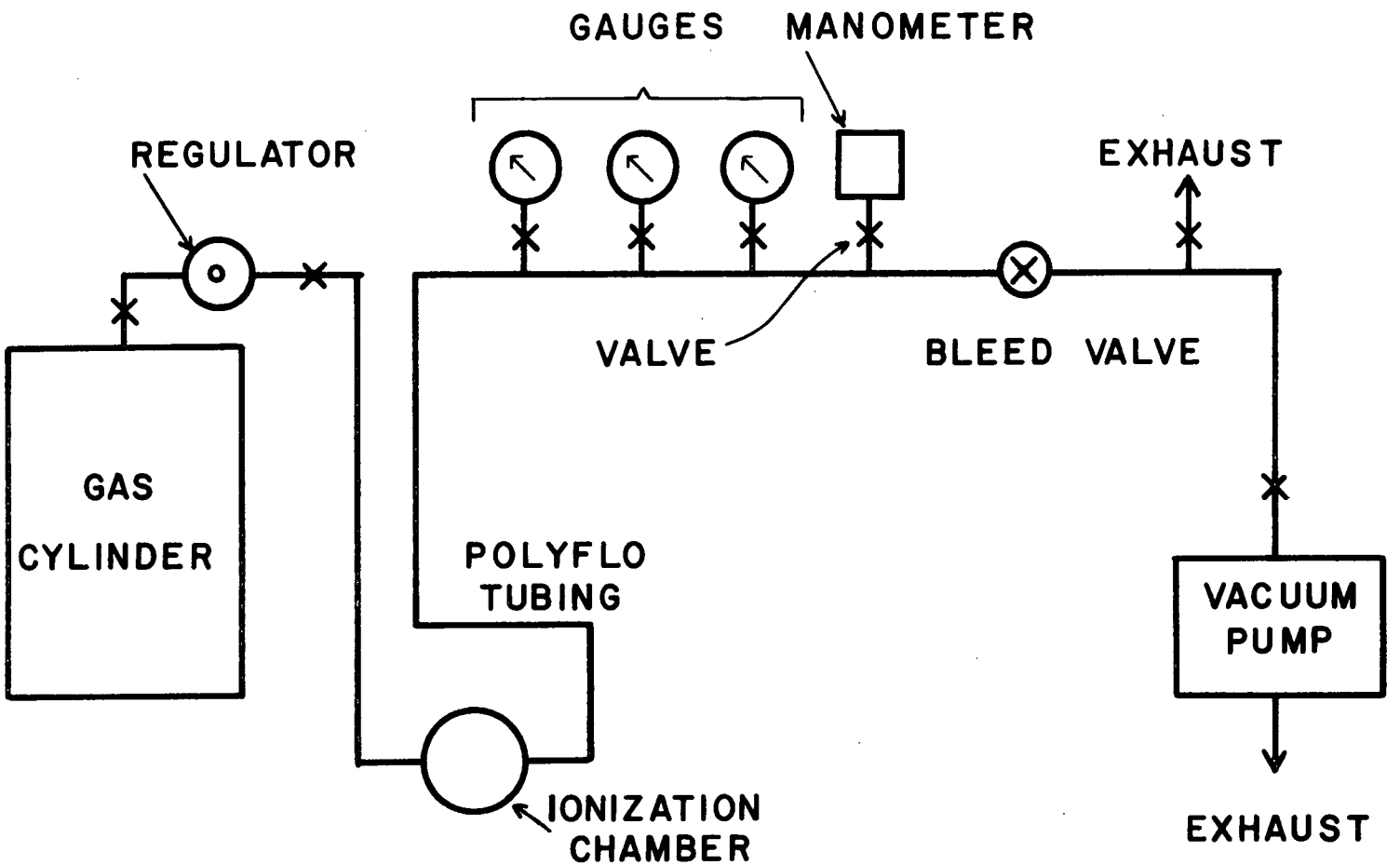


Figure 3.9: Gas Delivery System

Table 3.3: Gas Density & Purity

| Gas | Density ($mg/cm^3$) at 22°C and 1 atmosphere | Composition or Purity |
|---|---|---|
| $CH_4$ | 0.6633 | commercial 99.0% |
| $C_4H_{10}$ | 2.416 | instrument grade 99.5% |
| $CO_2$ | 1.8296 | bone dry 99.8% |
| $O_2$ | 1.3224 | medical 99.6% |
| A | 1.6507 | prepurified 99.998% |
| $N_2$ | 1.1573 | oxygen free 99.998% |
| $N_2O$ | 1.8296 | medical 98% |
| air | 1.1965 | 80% $N_2$ + 20% $O_2$ |
| TE | 1.0416 | 65.88% $CH_4$ + 31.2% $CO_2$ + 2.92% $N_2$ by partial pressure |

3.2.4.3 Temperature monitor

The gas temperature inside the cavity was taken to be the same as the water tank which was monitored with a thermistor probe (YSI T2635). Over a four month period, the temperature varied between 24 and 28°C. The ionization inside the cavity was corrected to 22°C according to

$$J(22°C) = J(T) \times \frac{273 + T}{273 + 22}$$

The mass of gas in the cavity at 22°C was taken to be the product of volume, density and absolute pressure (atmospheres).

3.2.5 Electronics

There were three voltage sources used for various ranges: 0 to 1000 Volts - batteries, 100 to 3000 Volts - Power Designs high voltage calibrated d.c. power source, model 1570, and 500 to 5000 Volts - CPS precision HV power supply, model 5001. Voltages were measured where necessary with a digital multimeter, either DANA model 4300 or FLUKE model 8000A.

The charge from the parallel plate chamber was determined by means of Keithley electrometers, either model 616 or model 610C, with range selector set to $10^{-9}$ Coulomb full scale and the multiplier switch chosen appropriately. These two instruments agreed with each other to ± ¼% and were therefore used interchangeably. They have been compared with other similar devices during pion dosimetry workshops and the agreement with the mean has been better than ± 1%.

The electrometer was used in the charge collection mode in order to obtain adequate sensitivity at the low dose rates available and to average over beam fluctuations during irradiation, since the beam is difficult to turn off. Consequently, the dosimetry system was operated in a dynamic charge collection mode. The voltage output from the electrometer, which was proportional to the charge collected, was read by a minicomputer (Data General NOVA 2/10) through a chain consisting of an inverting three times amplifier, a multiplexer and a 10-bit analogue to digital converter (GEC Elliot ADC 1201) (see figure 3.1). The pulsed output from the digital current integrator used to read the transmission chamber was fed to a preset scaler which also reported to the minicomputer.

The timing sequence for reading these devices is shown schematically in figure 3.10. The electrometer was released from zero

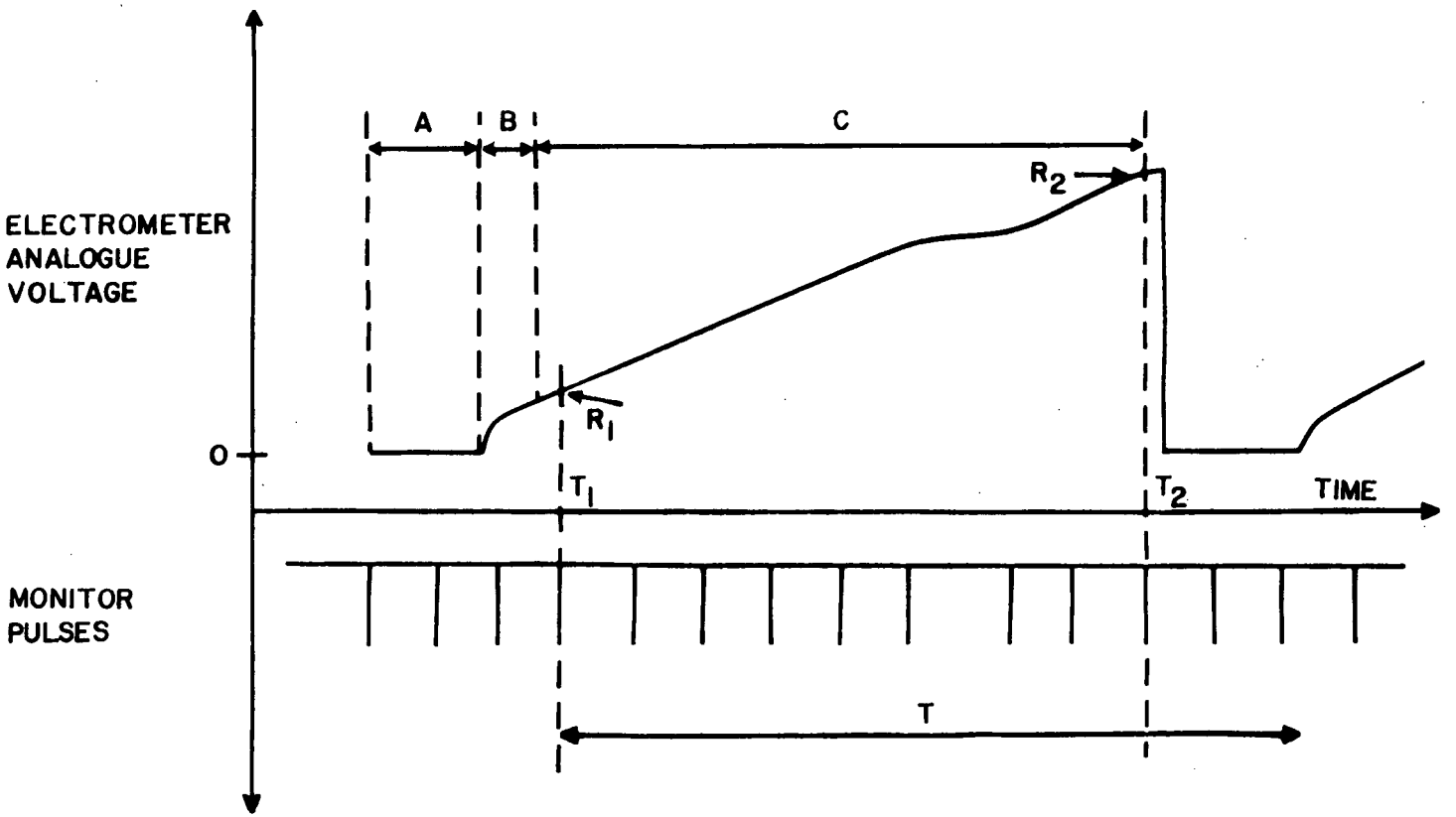


Figure 3.10: Timing Sequence for Reading the Electrometer

B is the 3 second time delay required to avoid transients

C is the elapsed time used to reject readings taken at too low dose rates

and charge collection initiated by a command to the solenoid reset device. There was a three second delay in order to avoid transients associated with this zero release. Immediately after the arrival of the next pulse from the digital current integrator, the electrometer and the real time clock were read. Immediately after the last of a predetermined number of pulses was received, the electrometer and clock were read again. The difference between the two electrometer readings divided by the specified number of monitor pulses gave the charge (in units of the ADC) collected per monitor pulse. The total elapsed time was used to reject measurements taken when the average intensity was less than 80% of the expected intensity. The dosimetry system is described fully in (139).

This system exhibited a 1¼% decrease in sensitivity over full-scale deflection. This non-linearity was corrected manually. The absolute value of the normalized charge was calibrated in the following manner. With the beam off, the electrometer was zeroed and released. The beam was turned on and the automatic control of the beam stopper was used to terminate the irradiation after the required number of monitor pulses. A graph of the collected charge versus number of monitor counts has a slope (charge per monitor count) which was compared to the computer determined value (ADC units per monitor count). The overall uncertainty in the normalized absolute charge is ± 1.0% for the electrometer calibration, ± 0.8% for the ADC-computer system calibration and ± 1.0% for the transmission chamber reproducibility which gives ± 1.6% when added in quadrature.

## 3.3 RESULTS

### 3.3.1 Saturation Characteristics

#### 3.3.1.1 Theoretical

One of the experimental difficulties involved with ionization chamber measurements is to ensure that all of the ion pairs are collected. Complete collection (saturation) is hampered by ion recombination which is of two types: initial and general. Initial recombination occurs where the ions formed in the track of a single ionizing particle meet and recombine. The amount of initial recombination is determined by the ion density along each separate track and is independent of the dose rate. Thus, at low pressures, initial recombination is important for the high LET tracks only, whereas at high pressures, it is important for both high and low LET tracks. Once the initial track structure has been obliterated by thermal diffusion and ionic drift, only general recombination remains. In general recombination, ions formed by the different ionizing particles recombine as they drift towards opposite electrodes. Therefore, general recombination increases with dose rate.

In this experiment, the dose rate was low enough that general recombination was negligible. According to Boag (133), the general recombination efficiency of ion collection in an air-filled parallel-plate chamber is given by

$$f = \frac{1}{(1 + \frac{1}{b}\xi^2)} \qquad 3.1$$

where $\xi = M\frac{d^2}{V}\sqrt{q}$, $M = 36.7\sqrt{P}$, P is the pressure in atmospheres, d is the plate separation in cm, V is the applied voltage in Volts, and q is the ion production rate in esu $cm^{-3}$ $sec^{-1}$. For the carbon chamber filled with air and placed at the peak dose rate provided by a proton current of 12 μA,

$q < 9.2 \times 10^{-3}$ P esu $cm^{-3}$ $sec^{-1}$. If the loss due to general recombination is to be kept less than 1%, $\xi < .246$ and hence,

$$V > 36.7 \quad P \quad (.614)^2 \quad 9.2 \times 10^{-3} \quad P \quad (.246)^{-1}$$

$$> 5.4 \; P$$

At the maximum pressure of 7½ atmospheres, the applied voltage must be greater than 40 Volts. Since this was easily attained for all gases investigated, general recombination was negligible. In some cases it was not possible to eliminate initial recombination entirely, and so some method of extrapolation to saturation was required. Based on a theory of Jaffé (134) as modified by Xanstra (135), Boag (133) has derived the expression

$$\frac{1}{i} = \frac{1}{I} + \frac{b}{E} \qquad 3.2$$

where i is the current measured at electric field strength E (volts/cm), I is the saturation current available at infinite voltage and b is a constant for a given type of radiation. This can be rearranged to give

$$i = I - bI \frac{i}{E} \qquad 3.3$$

$$\text{or} \quad f = \frac{i}{I} = 1 - b \frac{i}{E} \qquad 3.4$$

It has already been stated that f, the collection efficiency, must be independent of dose rate for initial recombination. Therefore, the parameter b in 3.4 must be inversely proportional to dose rate, and this is inconvenient. Since the quantity being studied here was J/M, the charge collected per unit mass per monitor pulse, then in equation 3.3, i is replaced by J/M and bI by a constant k giving

$$J/M = (J/M)_s - k \; (J/ME) \qquad 3.5$$

During the experiments, saturation was investigated by measuring J/M at different field strengths, E, and plotting J/M versus J/ME. This was

extrapolated to J/ME = 0, that is E very large, to yield the saturation value, $(J/M)_s$, and the slope, k. Similar procedures are in common use for neutron beams (136), alpha particles (137) and heavy ions (60).

3.3.1.2 Experimental

Saturation was studied for the various gases according to the technique outlined above. In figure 3.11, the values of J/M are plotted against J/ME (E is the field strength in V/cm) for the case of aluminum electrodes and carbon dioxide gas. As the pressure is increased, the collection efficiency at a particular voltage decreases. This is manifested by an increase in the value k.

At high pressure, it is more difficult to fit the data to a straight line. General recombination causes an additional decrease in efficiency at the low voltage end which makes the lines bend downwards. Ionization by collision at high voltages causes an increase in current which eventually leads to sparking. This latter problem has been encountered with ion chambers used to study fission recoils (104) and it may be diminished by rounding of chamber parts, particularly at the electrode edges (106).

In figure 3.12, the value of k is plotted versus mass with chamber position as a parameter for the case of carbon electrodes and methane gas. The steepness of the k versus mass curve increases with depth in the phantom because the mean LET increases with depth as shown in table 3.4. Some ion chamber systems (81) designed to measure mean LET are based on this dependence of k upon LET.

The values of k are plotted as a function of mass for a number of gases in figure 3.13 for the peak position and figure 3.14 for the plateau position. If the electric field is 100 V/cm, then k is numerically the percentage increase in current required to achieve saturation. The data

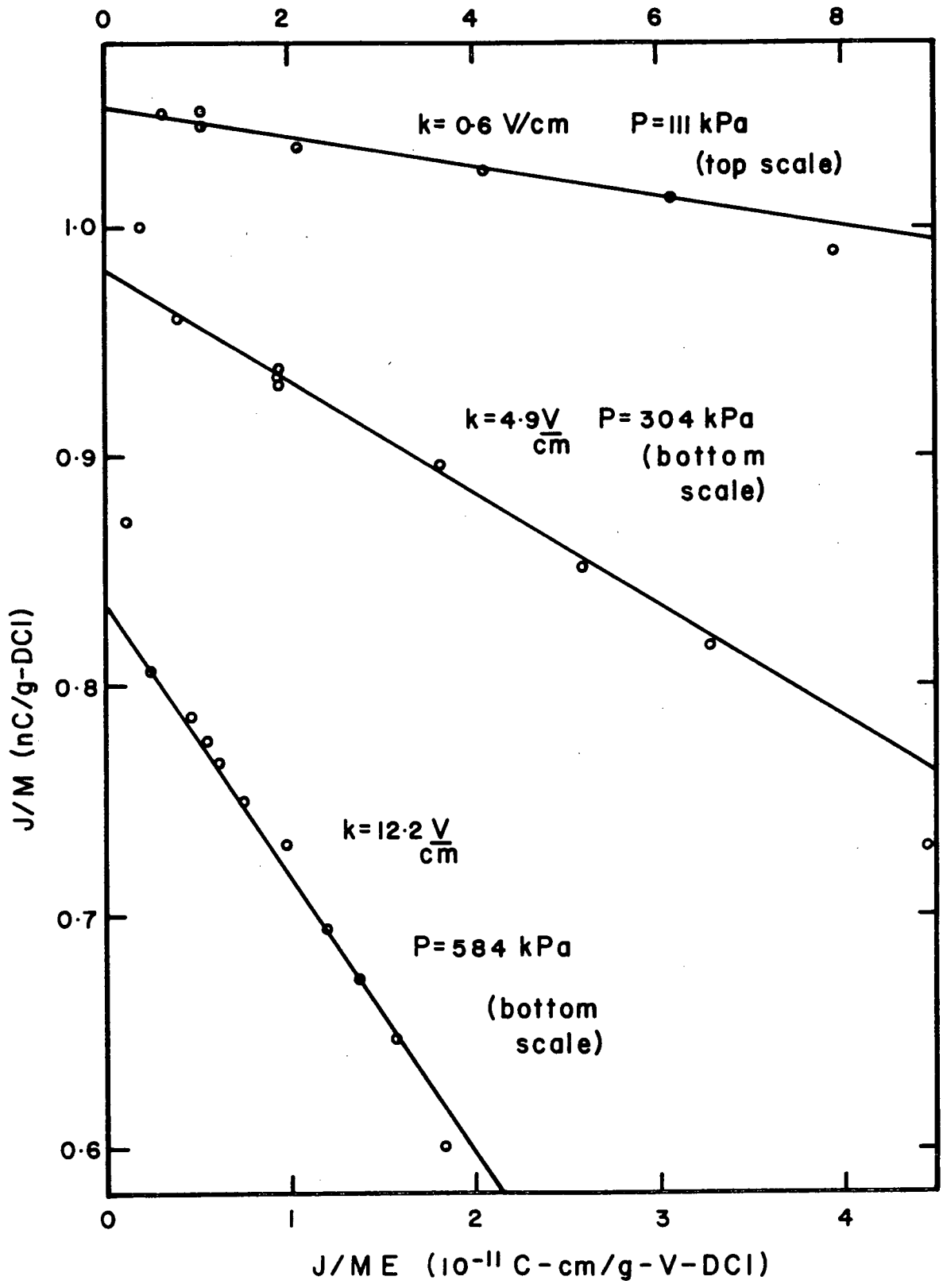


Figure 3.11: Saturation Curves for Carbon Dioxide

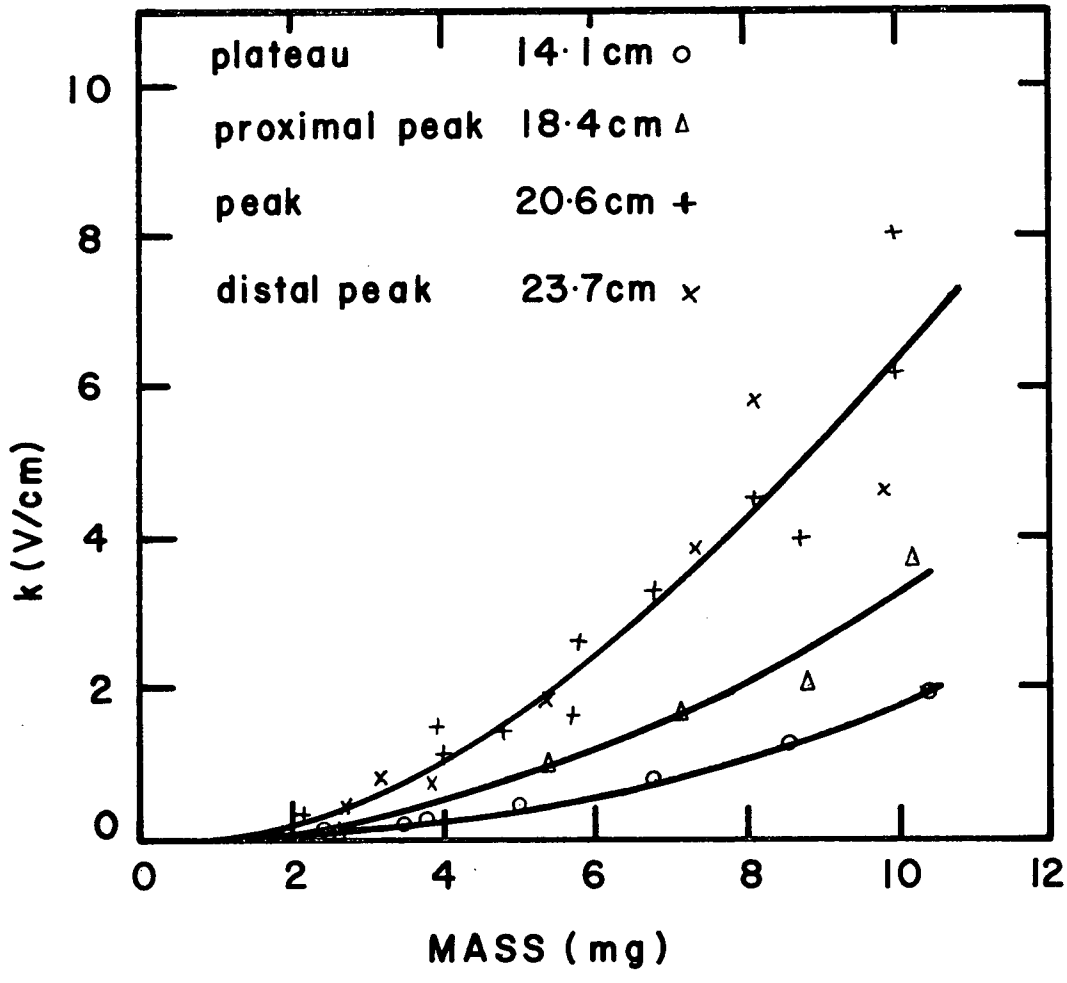


Figure 3.12: k Versus Mass Curves at Different Depths for Methane

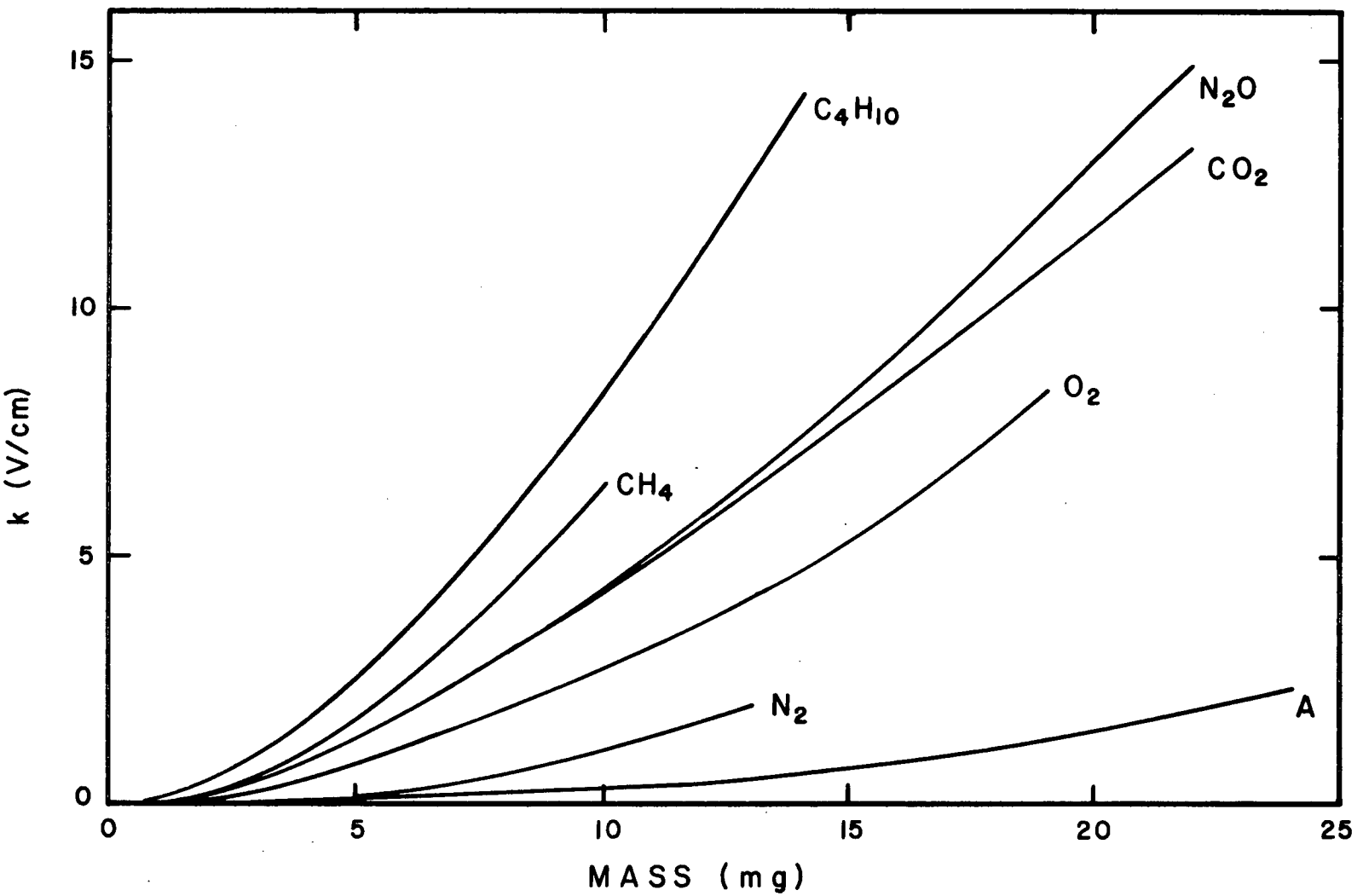


Figure 3.13: k Versus Mass at the Peak

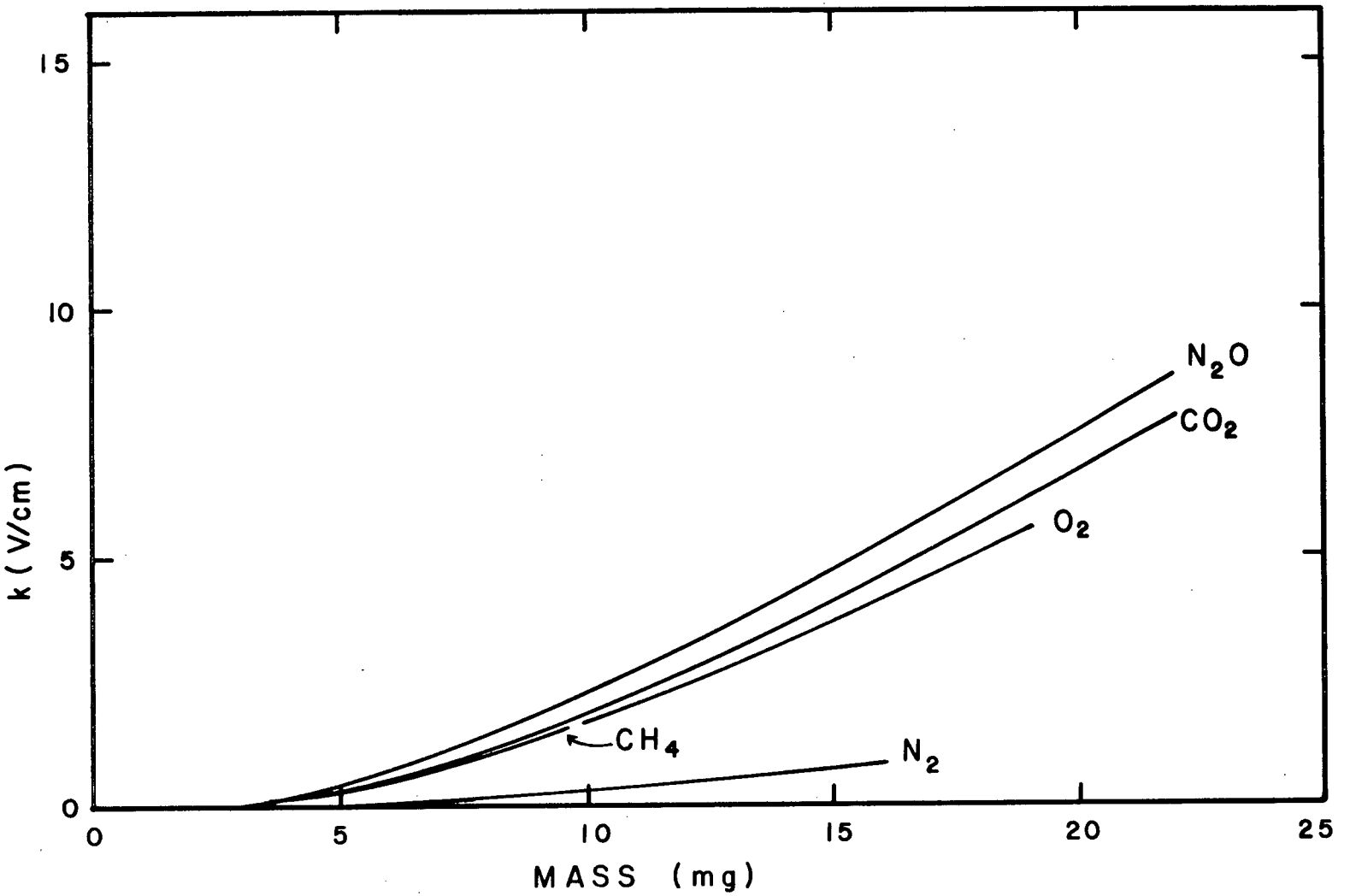


Figure 3.14: k Versus Mass at the Plateau

on these graphs are averages over several runs with different electrodes. For k > 10 V/cm, the uncertainty is ± 1.3 V/cm, between k = 2 and 10 V/cm, it is ± 1.0 V/cm and for k < 2 V/cm, it is ± 0.5 V/cm.

Table 3.4: Lineal Energy at Various Depths

| Position | Depth (cm) | Mean Lineal Energy (128) (MeV/μm) |
|---|---|---|
| plateau | 14.1 | 7 |
| proximal peak | 18.4 | 29 |
| peak | 20.6 | 41 |
| distal peak | 23.7 | 50 |

### 3.3.2 Polarity Effect

The magnitude of the ionization per unit mass is larger for negative polarity than positive. This polarity effect is less than ± 0.8% at pressures greater than one atmosphere. The polarity difference is plotted as a function of mass in figure 3.15. At pressures less than one atmosphere, the difference in J/M increases dramatically because the charge deposited in the electrodes due to the pions stopping there is a significant fraction of the ionization produced in the gas. This effect is larger in the peak than in the plateau as expected. In order to find the true ionization in the gas, the average over positive and negative polarity was taken. For some gases, J/M was measured at negative polarity only and half the average polarity difference was subtracted to yield the true ionization.

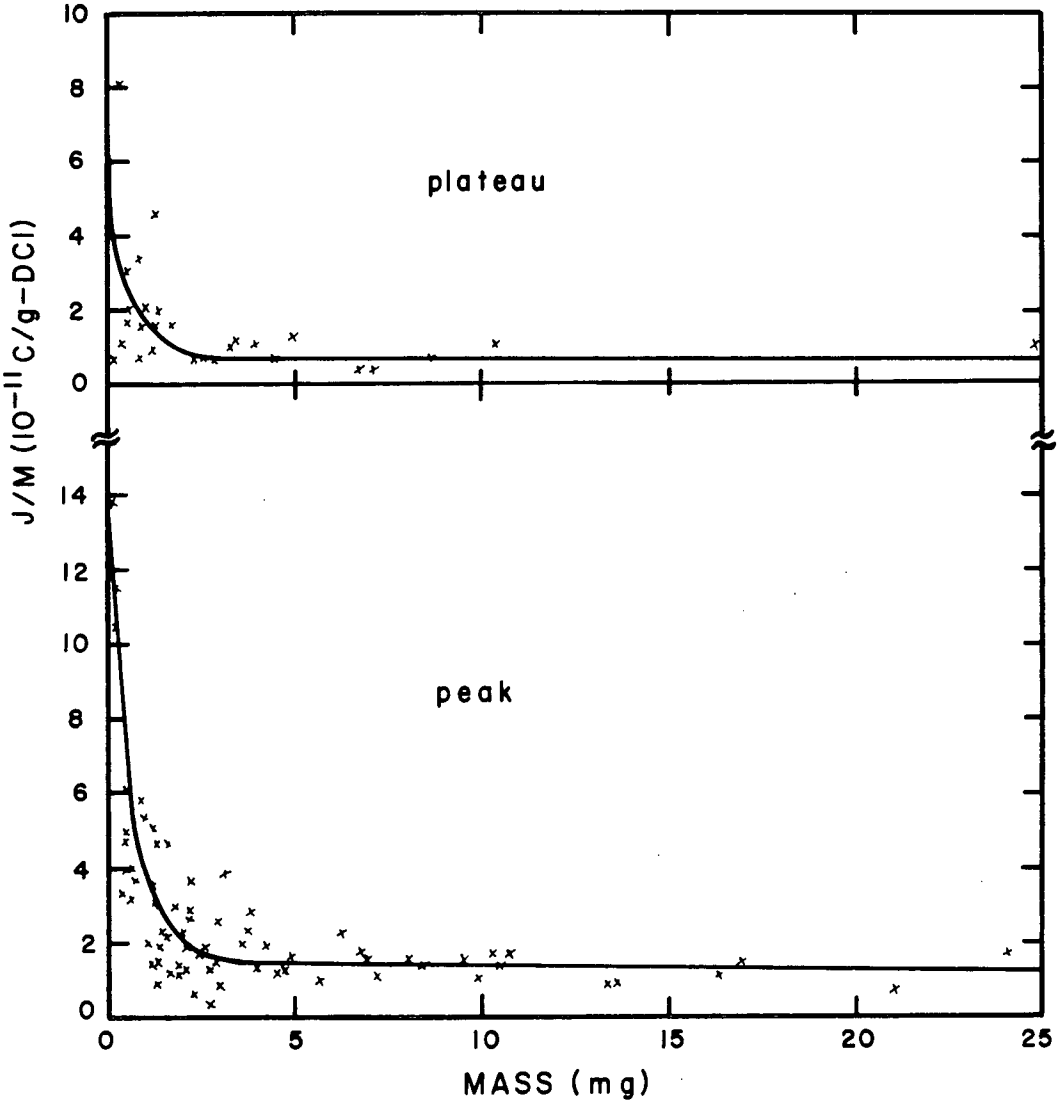


Figure 3.15: Polarity Difference Versus Mass

Data is shown for all the gases measured.

### 3.3.3 J/M Versus Pressure

The saturation value of J/M plotted against pressure is shown for methane and carbon dioxide in figures 3.16 and 3.17 respectively. These data were taken with carbon electrodes at negative polarity. The circles indicate values of J/M made by the extrapolation technique (equation 3.5). The triangles indicate values of J/M made at fixed field strengths (of the order 100 to 200 V/cm) which were subsequently corrected to saturation using k values determined in the first experiment.

The error bars shown in these figures represent the relative uncertainty in J/M. The uncertainties were assigned by considering best and worst fits to the saturation data. At low pressure, the uncertainty is large because of fluctuations in the ion chamber leakage. Typically, the leakage was ± 10 to 20 fA. This is about 1% of the signal available from most gases at atmospheric pressure for a 10 μA proton current from the cyclotron. The uncertainty in J/M passes through a minimum between 1 and 3 atmospheres. At high pressures, the slope of the saturation curves is large and somewhat uncertain because of the effects discussed in section 3.3.1. and this results in increased error bars. For the values measured at fixed voltage, the error bar is the sum in quadrature of the statistical uncertainty in the reading and the error in the k value. The agreement between the circles and triangles for methane at pressures above one atmosphere indicates that the day-to-day reproducibility is about ± 2%, which is within the error bar.

After the average was taken over polarity and random fluctuations were smoothed, the values of J/M for carbon electrodes were plotted for all the gases in figures 3.18 and 3.19 for the peak and plateau respectively. The uncertainty in the average value at zero pressure is typically ± 2%.

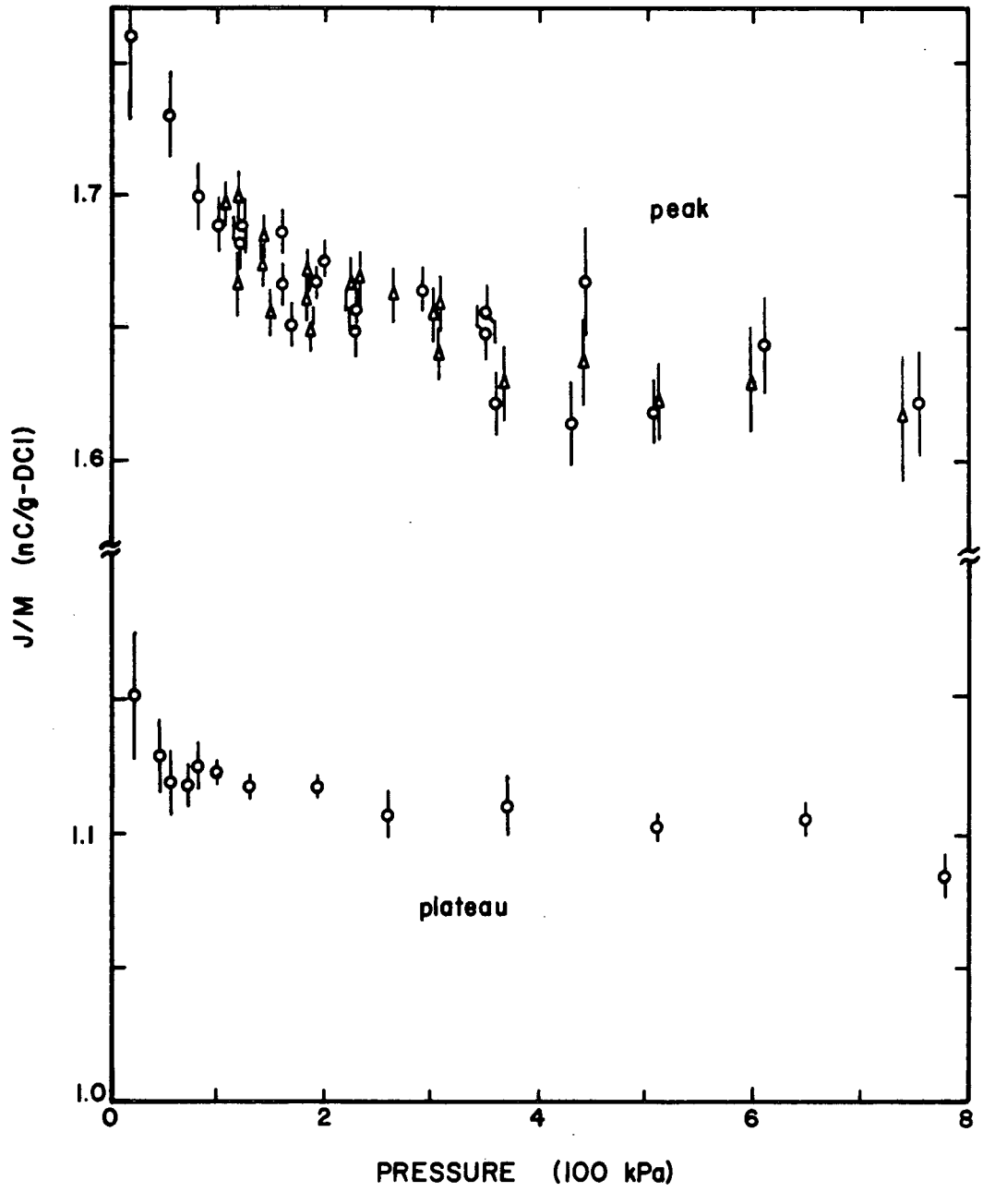


Figure 3.16: J/M Versus Pressure for Methane

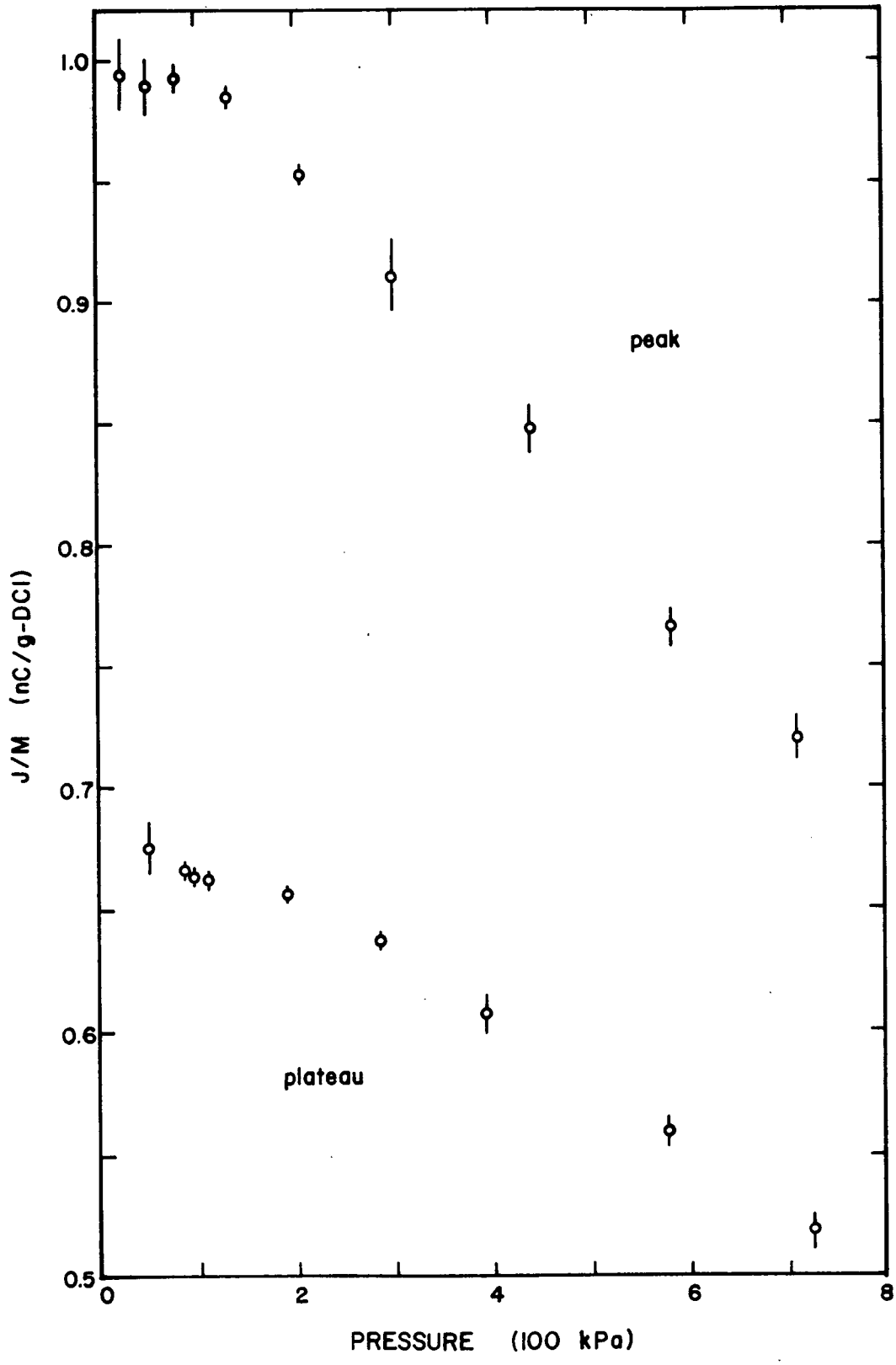


Figure 3.17: J/M Versus Pressure for Carbon Dioxide

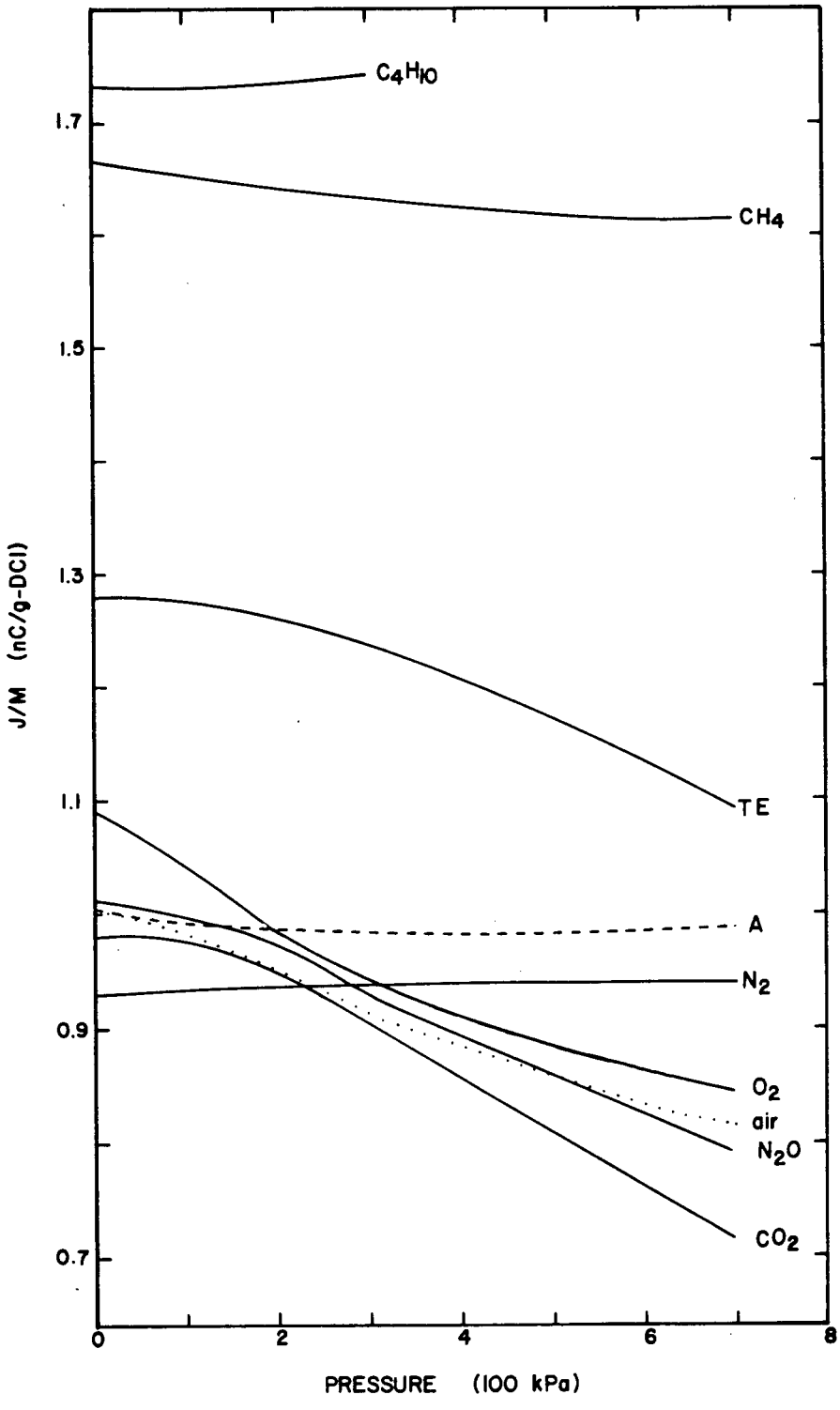


Figure 3.18: J/M Versus Pressure for All the Gases at the Peak with Carbon Electrodes

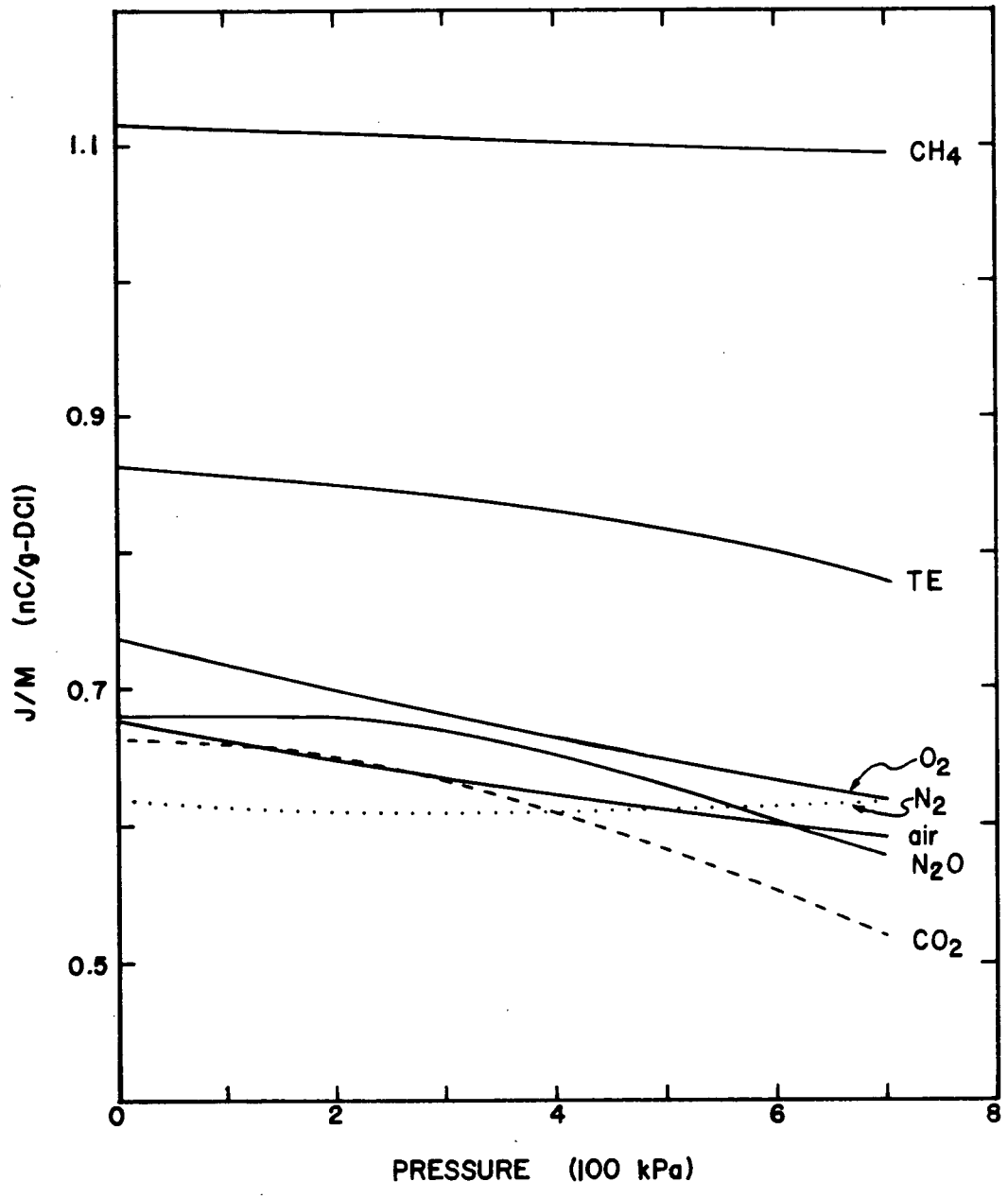


Figure 3.19: J/M Versus Pressure for All the Gases at the Plateau with Carbon Electrodes

The value of J/M for all oxygen bearing gases decreases with pressure in both the peak and plateau. The rate of decrease is faster in the peak than in the plateau as indicated by the value of the pressure at which the curves for oxygen bearing gases cross over the one for nitrogen. This fact can be seen more clearly in figure 3.20 where the ionization in the peak is divided by that in the plateau and the peak to plateau ratio is plotted against pressure for the various gases. At zero pressure, all of the ionization is produced by crossers which originate in the carbon walls. Since there are no gas specific contributions to the ionization, the cavity is an ideal Bragg-Gray cavity and the peak to plateau ratio is a constant independent of the type of gas filling. The spread in values of J/M between the various gases at zero pressure is ± 2% and gives an indication of the uncertainty in the value of the peak/plateau ratio for any particular gas.

After correcting for saturation and polarity, the data for aluminum electrodes are displayed in figures 3.21 and 3.22 for the peak and plateau respectively. In most cases, the shape of the curve for a particular gas is the same whether the data was acquired with carbon electrodes or with aluminum. The peak to plateau ratio is shown in figure 3.23. Once again, the J/M curves for oxygen bearing gases exhibit a dramatic dependence on pressure. The peak to plateau ratio extrapolated to zero pressure is lower for aluminum than carbon. This is related to the kerma factor and will be discussed in section 3.4.3.

Besides the usual measurements in the peak and plateau, a measurement of J/M versus pressure with aluminum electrodes and carbon dioxide was made in the region of the electron tail (35.6 cm depth). The absolute change in J/M is small, but the percentage change is larger than expected

from the Sternheimer density effect. The implication of such a result is discussed in section 3.4.1.

Data for air and TE gas was taken with TE-A150 plastic electrodes. The averaged values after smoothing are plotted in figure 3.24. There is little difference in absolute value for these curves and those with carbon electrodes.

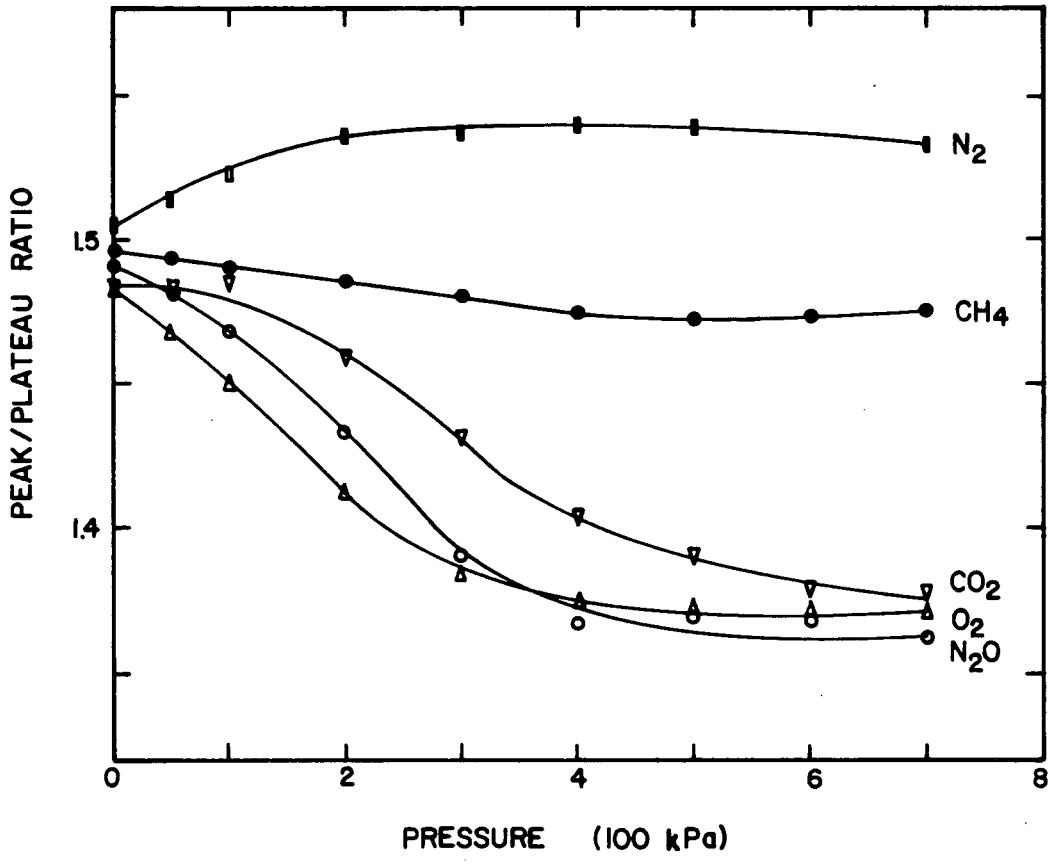


Figure 3.20: Peak to Plateau Ratio Versus Pressure with Carbon Electrodes

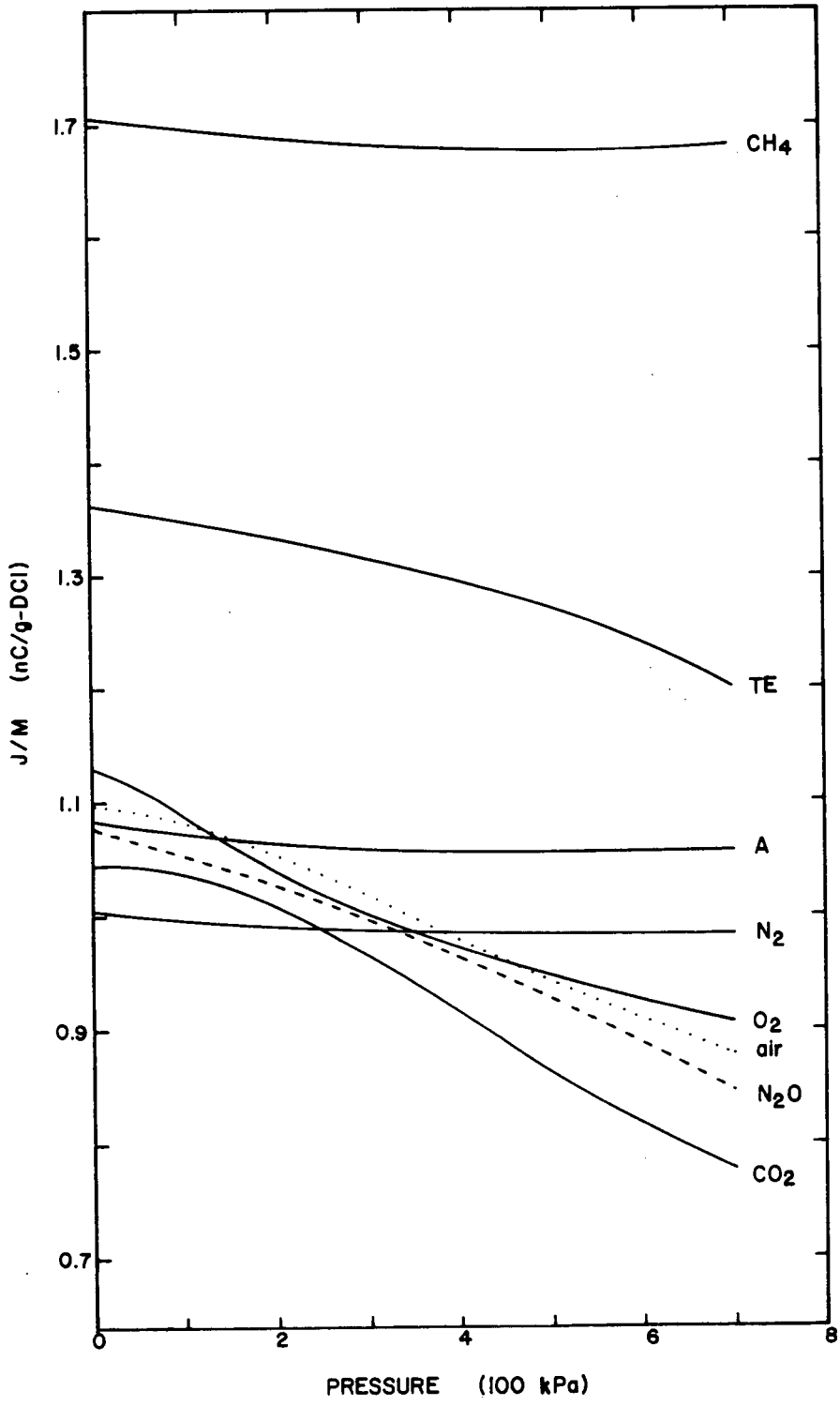


Figure 3.21: J/M Versus Pressure for All the Gases at the Peak with Aluminum Electrodes

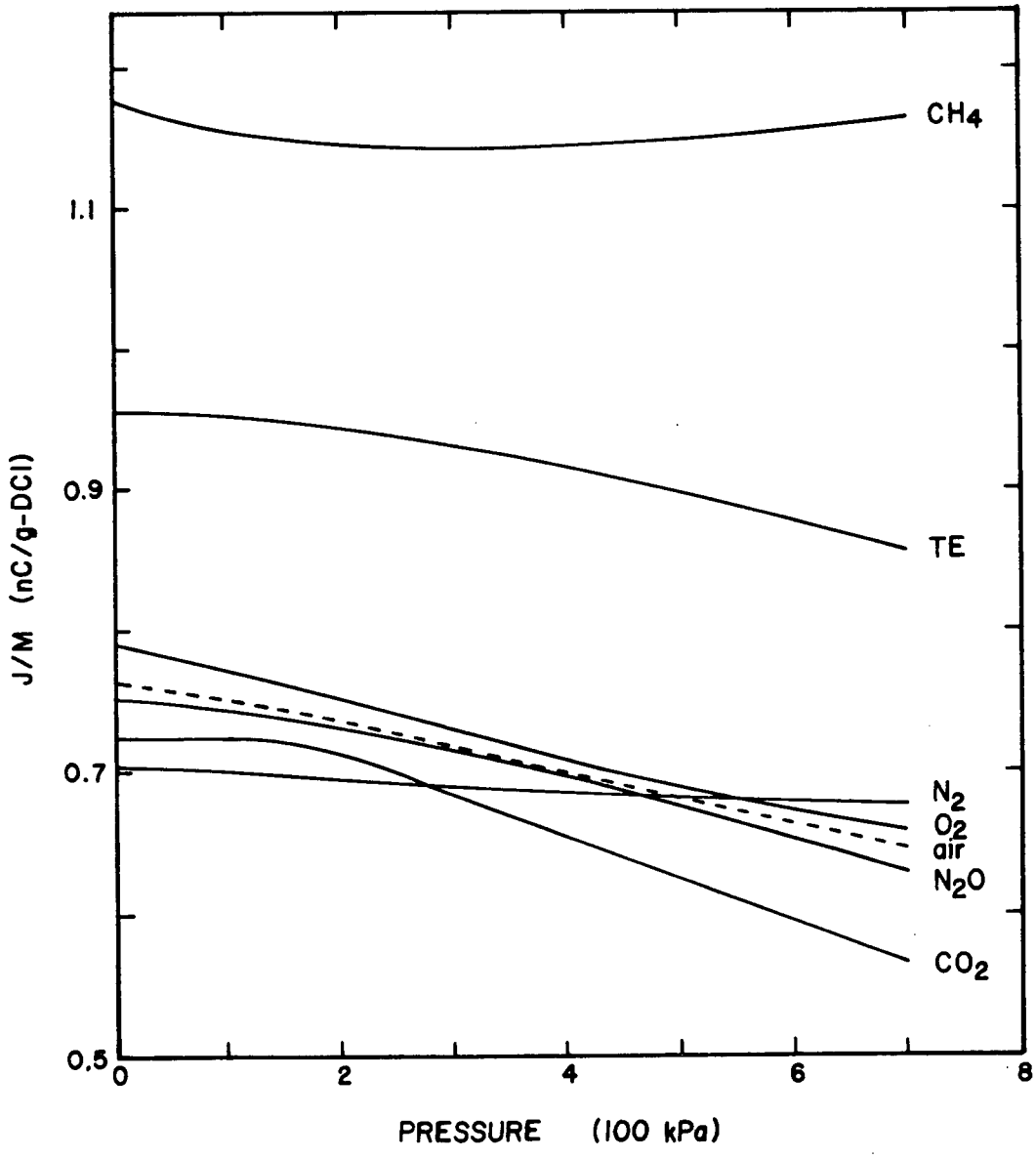


Figure 3.22: J/M Versus Pressure for All the Gases at the Plateau with Aluminum Electrodes

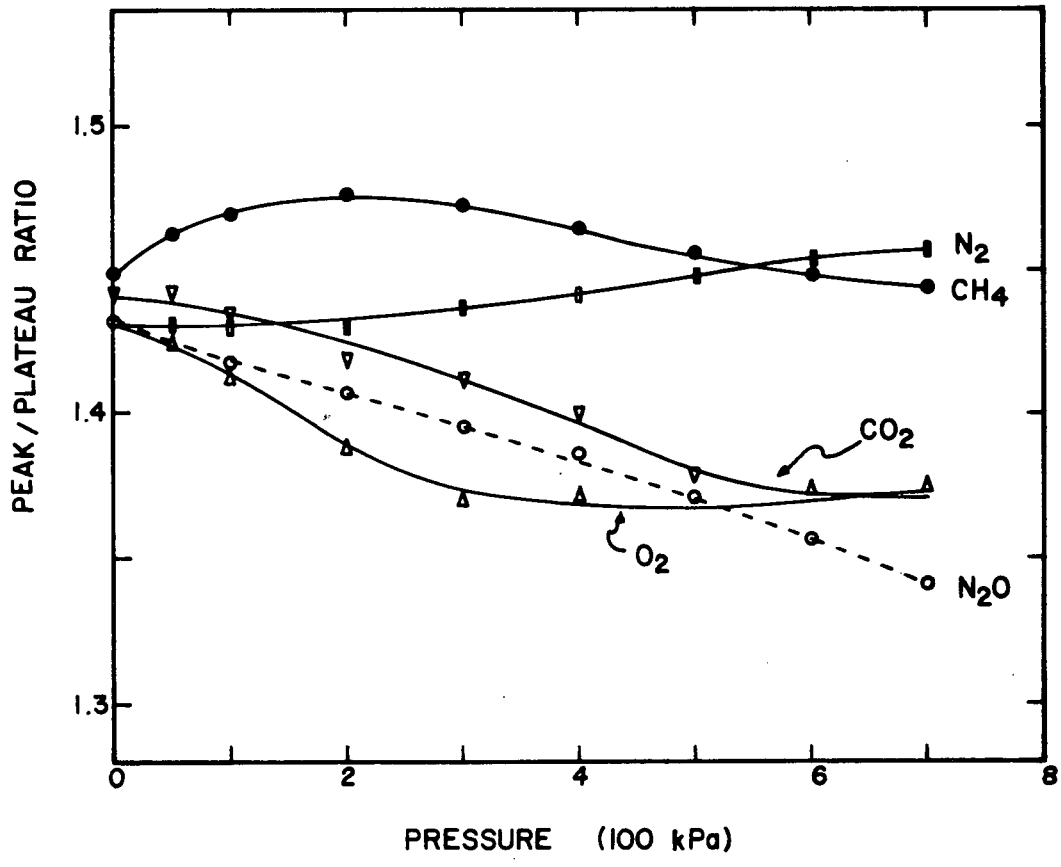


Figure 3.23: Peak to Plateau Ratio Versus Pressure with Aluminum Electrodes

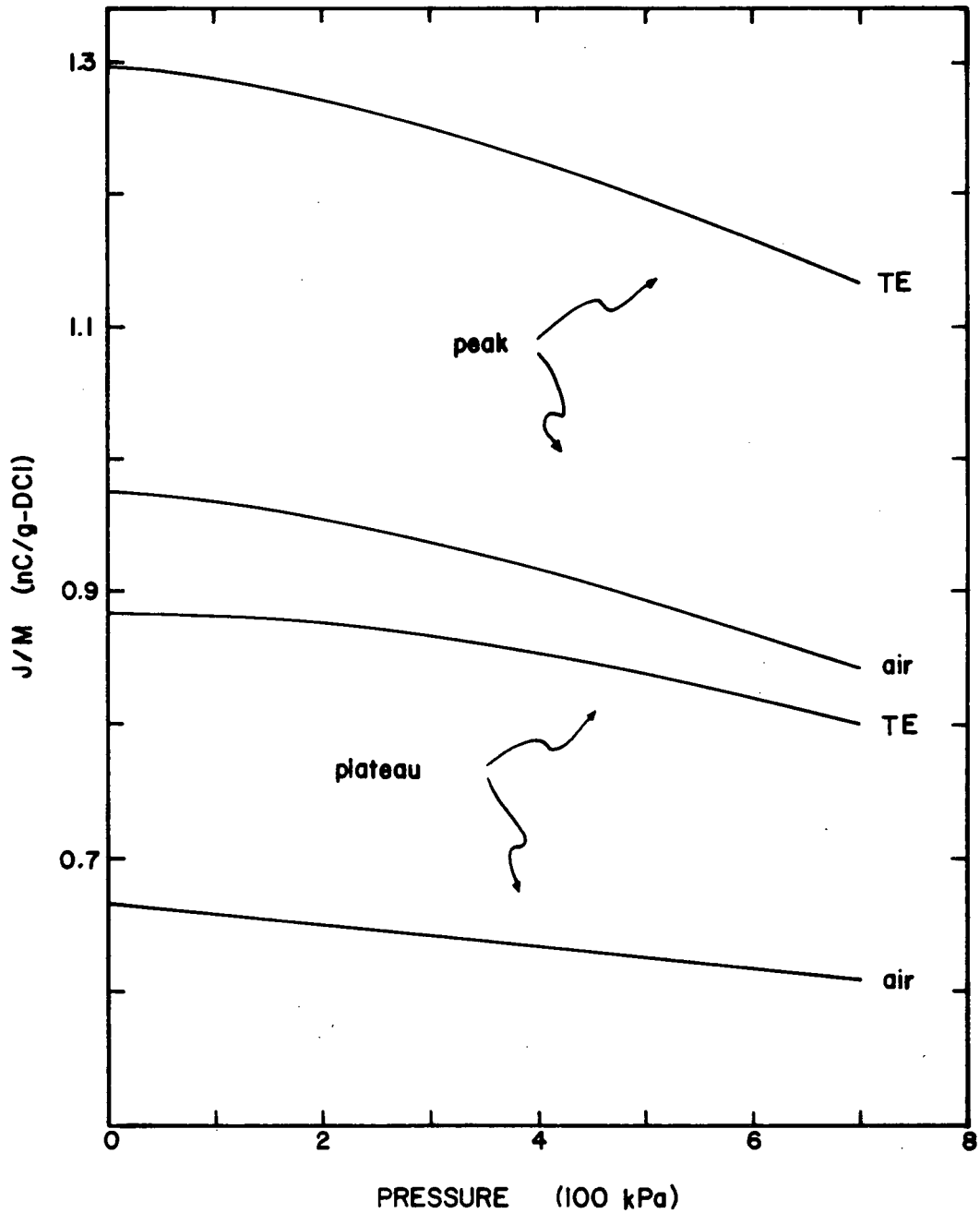


Figure 3.24: J/M Versus Pressure for Air and TE gas with TE-A150 Electrodes

## 3.4 DISCUSSION

### 3.4.1 Comparison Between Calculation and Experiment

This comparison deals with ionization chambers having carbon electrodes and being filled with methane or carbon dioxide gas. For a beam consisting only of the charged secondaries released during pion capture, the calculation of chapter 2 predicts that the ionization per unit mass is a function of pressure due to pion captures in the gas and perturbations of the secondary flux by the cavity. Between 0 and 7 atmospheres, the calculated change is -7% for $CO_2$ (see figure 2.18) and +2% for $CH_4$ (see figure 2.17). The decrease for $CO_2$ is primarily due to the release of less kinetic energy to charged secondaries per pion capture in oxygen than in carbon. In practice, ionization in the chamber gas is produced not only by the charged star secondaries, but also by contaminating electrons and muons, passing pions and star neutrons. Of these other particles, further calculation in chapter 2 indicated that only ionizations by electrons are expected to exhibit a pressure dependence, and this is of the order of -10% for either gas between 0 and 7 atmospheres (see figure 2.19).

The observed change in J/M measured at the peak and plateau respectively is -37% and -27% for $CO_2$ and -3% and -2% for $CH_4$ (see figures 3.18 and 3.19). For $CO_2$, this is about four times as large as calculated. Besides this discrepancy in magnitude for $CO_2$, an experiment in the electron tail revealed a change of -23%. Increasing the magnitude of the Sternheimer effect to account for this would give a percentage change in the plateau which exceeds that in the peak, and so there must be a systematic effect acting on the whole beam which has yet to be discovered.

Consider the equation

$$[U(P)]^{-1} (g_e F_e(P) + g_{\mu,\pi} + g_s F_s(P)) = J/M(P) \qquad 3.6$$

where the $g_i$'s (see tables 3.6 and 3.7) are fractions of the total ionization due to electrons, muons plus passing pions and pion stars; the F's are functions of pressure normalized to unity at P = 0 and represent the pressure dependence of the ionization for electrons, $F_e$, and stars, $F_s$; U(P) is a systematic correction factor under consideration; and J/M(P) is the measured ionization per unit mass also normalized to unity at P = 0. There are equations of this form for measurements in the peak, plateau and electron tail. In principle, since $g_s = 0$ in the electron tail, one could solve this equation for U(P). This was not done because values of $g_e$ and $g_\mu$ are fairly uncertain in the electron tail. Instead, J/M(P) measured in the peak and plateau were used to solve for U(P) and $F_s(P)$ simultaneously. When the value of U(P) is substituted back into the equation for the electron tail, reasonable agreement (± 2%) is obtained.

The values of U(P) are plotted in figure 3.25. For $CH_4$, U(P) is independent of pressure within ± 0.5% indicating that there is no systematic correction factor for this gas. For $CO_2$, U(P) is independent of pressure up to 2 atmospheres, after which it increases to 1.22 at P = 700 kPa. It is interesting to speculate what causes this phenomenon. It has long been recognized that initial recombination is a problem with electronegative gases (76). Failure to collect all the ionization due to initial recombination seems unlikely because sound and careful methods were used to find the saturation current. Another possible explanation is that the electron W-value is a function of pressure for the electronegative gases. Such gases are capable of electron trapping according to the

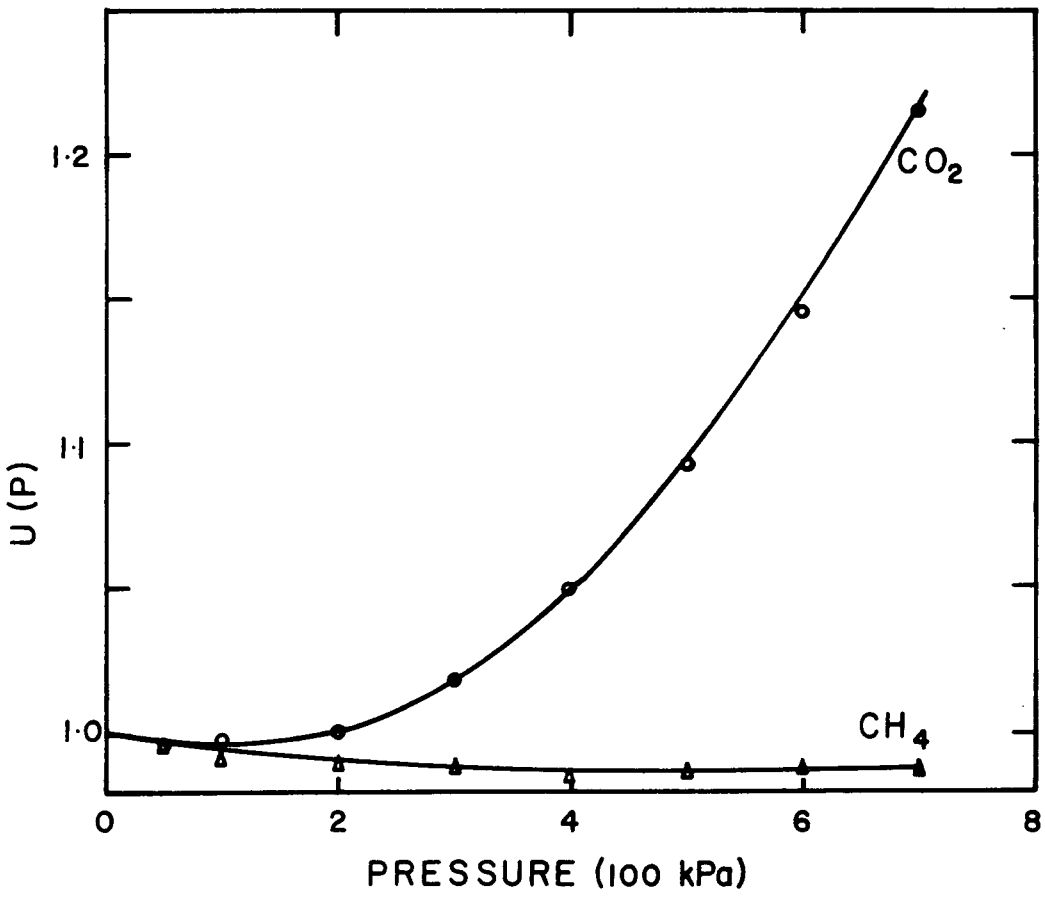


Figure 3.25: Factor U(P) Versus Pressure

process:

$$O_2 + e^- + S \rightleftharpoons O_2^- + S^* + \text{energy} \qquad 3.7$$

In the case of pure oxygen, S is another $O_2$ molecule and the energy appears as translation or internal energy of the molecule. The W-value increases because energy which may have produced ionization ends up as excitation. Since the attachment coefficient increases linearly with pressure for E/P < 3V/cm-torr (91), the W-value would also be pressure dependent. This process is not related to initial recombination, and instead would apply to the delta rays and tertiary electrons liberated by high and low LET particles alike. Whether or not electron trapping causes this systematic scaling factor for $CO_2$ is not crucial to the argument. It is not a significant effect below 200 kPa.

The extracted pressure dependence, $F_s(P)$, and the calculated value, $G_s(P)$, are compared in figure 3.26. Qualitatively the calculation and the experiment yield similar pictures in that the $CH_4$ curve is fairly flat and the $CO_2$ decreases. The percentage difference between $CO_2$ and $CH_4$ at 700 kPa was calculated to be 8%, whereas experimentally it is 16%. The uncertainty in $F_s(P)$ at 700 kPa was estimated to be ± 4% by considering different values for the $g_i$'s and allowing J/M to change by ± 2%. The value for $F_e(P)$ was taken to be correct.

Since the extracted pressure dependence, $F_s(P)$, changes more quickly with pressure than predicted, $G_s(P)$, it is important to consider what aspects of the calculation could be altered and what effect this alteration would have on the agreement. Clearly, the inclusion of dose due to heavy ions would make $G_s(P)$ a stronger function of pressure since the range of the heavier ions is small compared with the size of the chamber. This was illustrated for Li ions and protons in figures 2.15 and 2.16.

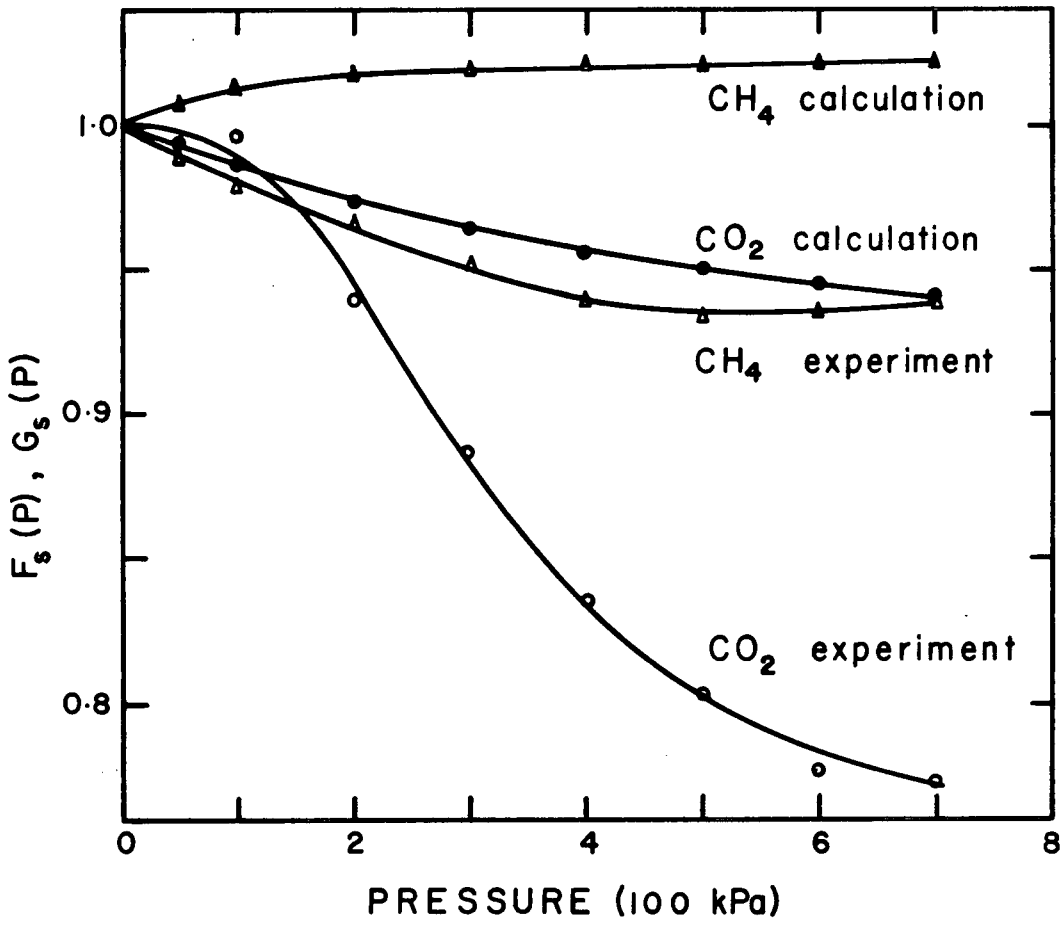


Figure 3.26: Comparison of Calculated Observed Pressure Dependence for J/M

Such an effect would be more important for oxygen, which has 2.4 MeV missing out of 14.4 MeV, than for carbon, which has 1.3 MeV missing out of 28.8 MeV. Since most of these heavy ions will be stoppers or insiders, only their energy is important to the calculation and not their stopping power. The inclusion of the dose due to undetected heavy ions would improve the agreement between $F_s(P)$ and $G_s(P)$.

Star neutrons have not been dealt with explicitly. It is reasonable to assume that high energy neutron interaction will produce a spectrum of charged secondaries similar to that produced by pion capture. Since the number of neutrons released per pion is about the same for both carbon and oxygen, and since the decrease of J/M with pressure calculated for the charged secondaries is due to less energy available per pion capture on oxygen than carbon, inclusion of some neutron dose would tend to make $G_s(P)$ for $CO_2$ less pressure dependent than already calculated, thus increasing the discrepancy between the calculation and experiment. Even if the values for W and r were calculated for the neutrons, there still remains the problem of how to fractionate the dose between neutrons and charged particles.

An increased understanding of pion capture and intra-molecular transfer would be useful to calculate a more accurate value of $G_s(P)$. But, even complete transfer from the C atom to one of the two O atoms within $CO_2$ would make only minor changes in $G_s(P)$.

There remains an unresolved quantitative discrepancy between the calculation and experiment. The qualitative agreement does confirm the physical effects which were included in the calculation of chapter 2. These effects stated that there is significant pion capture in the gas and that pion capture on oxygen yields less kinetic energy to charged secondaries than capture on carbon.

### 3.4.2 Absolute Dose in Carbon

In this section, measured values of J/M for carbon dioxide and methane are used along with calculated values of W and r to determine the dose in carbon. The approach taken was to extrapolate J/M to P = 0 where the non-Bragg-Gray nature of the cavity is insignificant. Alternatively, J/M at P = 100 KPa could have been used with appropriate values for W and r. The former approach suffers because of a larger uncertainty in the extrapolation procedure for J/M. The latter suffers because of the larger discrepancy between the calculated and measured W and r curves. Table 3.5 gives the values of J/M extrapolated to zero pressure for carbon electrodes with all the gases used experimentally.

The total dose is calculated according to

$$D_T = \left(\frac{J}{M}\right)_T W_\beta \left( \sum_i g_i \left(\frac{W}{W_\beta}\right)_i r_i \right) \qquad 3.8$$

where $g_i$ is the fraction of the ionization due to the $i^{th}$ source: electron, muon, passing pion or pion star; r is the ratio of dose in carbon to dose in gas for the pion stars, and it is the stopping power ratio for the electrons, muons and passing pions; and the other terms have been defined previously. The value of $g_i$ was determined for the sake of completeness from the value of $f_i$ in table 3.1 ($f_i$ is the fraction of the dose due to the $i^{th}$ source) according to:

$$\left(\frac{J}{M}\right)_T W_\beta \; g_i \left(\frac{W}{W_\beta}\right)_i r_i = f_i \; D_T \qquad 3.9$$

Values of $(W/W_\beta)_i$, $r_i$ and $g_i$ in peak and plateau taken from various graphs and tables are collected for $CH_4$ and $CO_2$ in tables 3.6 and 3.7 respectively. It has been assumed that the W-value for electrons is not a function of energy, and therefore $W/W_\beta = 1.00$ in both the peak and plateau.

Table 3.5: J/M Extrapolated to Zero Pressure for Carbon Electrodes

| Gas | W* (eV) | J/M (peak) (nC/g - DCI) | J/M (plateau) | Ratio |
|---|---|---|---|---|
| $CH_4$ | 27.10 | 1.666 | 1.114 | 1.496 |
| $CO_2$ | 32.80 | 0.982 | 0.662 | 1.483 |
| $N_2$ | 34.65 | 0.930 | 0.618 | 1.505 |
| $N_2O$ | 32.55 | 1.012 | 0.679 | 1.490 |
| $O_2$ | 30.83 | 1.090 | 0.735 | 1.483 |
| TE | 29.2 | 1.281 | 0.863 | 1.484 |
| air | 33.73 | 1.004 | 0.675 | 1.487 |
| A | 26.3 | 1.005 | | |
| $C_4H_{10}$ | 23.2 | 1.731 | | |

* W-values are from Christophorou (86) except for air (61) and TE gas (62).

Table 3.6: Values Required to Calculate the Dose for $CH_4$

| | | Peak | | Plateau | |
|---|---|---|---|---|---|
| | $W/W_\beta$ | r | $g_i$ | r | $g_i$ |
| electrons | 1.00 | 0.591 | 0.15 | 0.587 | 0.24 |
| muons and passing pions | 1.05 | 0.740 | 0.40 | 0.740 | 0.66 |
| stars | 1.014 | 0.738 | 0.45 | 0.738 | 0.11 |

Table 3.7: Values Required to Calculate the Dose for $CO_2$

| | | Peak | | Plateau | |
|---|---|---|---|---|---|
| | $W/W_\beta$ | r | $g_i$ | r | $g_i$ |
| electrons | 1.00 | 0.768 | 0.16 | 0.762 | 0.25 |
| muons and passing pions | 1.05 | 1.031 | 0.40 | 1.031 | 0.65 |
| stars | 1.013 | 1.035 | 0.45 | 1.035 | 0.10 |

The rather high value of $W/W_\beta = 1.05$ for passing pions is an average made by comparing preliminary measurements of Dicello (55) for 78 MeV pions in air, nitrogen and argon to the accepted values for electrons. The dose in carbon calculated using equation 3.8 is summarized in table 3.8.

Table 3.8: Dose in Carbon (μGy/DCI)

| | Methane | Carbon Dioxide | $\frac{\text{Dose } CH_4}{\text{Dose } CO_2}$ |
|---|---|---|---|
| Peak | 33.2 | 32.8 | 1.012 |
| Plateau | 22.0 | 21.7 | 1.014 |

The agreement between the dose values measured with the different gases is excellent. The relative uncertainty is ± 2% in the measurement of J/M and ± 1% in the electron W-value giving a total of ± 2.2%.

The absolute uncertainty is more difficult to assess:

1.6% systematic uncertainty in determining the absolute normalized current (see section 3.2.5).

1.7% uncertainty in measuring J/M due to daily variation in reproducibility and extrapolation. This is less than the relative uncertainty mentioned above since the monitor chamber reproducibility is already included in the 1.6%.

2.0% uncertainty in the mass determination, about 0.4% for the volume and the remainder for the pressure.

1.0% uncertainty in the absolute value of $W_\beta$.

3.9% (peak)
4.2% (plateau)

uncertainty in the value of $\sum_i g_i \left(\frac{W}{W_\beta}\right)_i r_i$ from equation 3.8. An uncertainty of 3% is assigned to the absolute value of r for both the star products and the passing pions. For the electrons, r is uncertain by 2%. The uncertainty in W-value is 1% for the star products and 4% for the passing pions. Then the product of $\frac{W}{W_\beta}$ r has an uncertainty for the star products of 3.2%, for the passing pions of 5.0% and for the electrons of 2.0%. These are weighted by the respective $g_i$ values to give 1.5 + 2.0 + 0.3 = 3.8% in the peak and 0.3 + 3.3 + 0.5 = 4.1% in the plateau. There is a 1% uncertainty due to the values of $g_i$ which adds in quadrature to give 3.9% in the peak and 4.2% in the plateau.

Therefore the total absolute uncertainty is ± 5.1% in the peak and ± 5.3% in the plateau.

The value of $\overline{\frac{W}{W_\beta} \times r}$ for a particular gas has been evaluated using this dose calibration:

$$\overline{\frac{W}{W_\beta} \times r}_{gas} = \frac{\left\langle \frac{J}{M} \times W_\beta \times \left(\frac{W}{W_\beta} \times r\right) \right\rangle_{CH_4,\ CO_2}}{\frac{J}{M}_{gas} \quad W_{\beta\ gas}} \qquad 3.10$$

These values are found in table 3.9. A carbon walled ionization chamber filled with any one of these gases and used to measure J/M extrapolated to zero pressure will yield the dose in carbon according to:

$$D_{carbon} = \frac{J}{M}_g \times W_{\beta_g} \times \left(\overline{\frac{W}{W_\beta} \times r}\right)_g \qquad 3.11$$

Note that $\overline{\frac{W}{W_\beta} \times r}$ is larger by 1.012 ± 0.005 in the peak than in the plateau. The absolute uncertainty in $\overline{\frac{W}{W_\beta} \times r}$ is about 4% due to the initial calibration. If the chamber is used at atmospheric pressure, there is an additional uncertainty of the order of ± 2% due to the non-Bragg-Gray effects shown graphically in figure 3.26.

Table 3.9: Evaluation of $\overline{\frac{W}{W_\beta} \times r}$ for Carbon Electrodes

| | Peak | Plateau |
|---|---|---|
| $CH_4$ | 0.731 | 0.725 |
| $CO_2$ | 1.025 | 1.008 |
| $N_2$ | 1.024 | 1.022 |
| $N_2O$ | 1.002 | 0.990 |
| $O_2$ | 0.982 | 0.966 |
| TE | 0.882 | 0.869 |
| air | 0.975 | 0.961 |
| A | 1.249 | - |
| $C_4H_{10}$ | 0.822 | - |

### 3.4.3 Kerma Factor

In this section, the problem of determining the dose in a material of interest on the basis of the dose measured in a different material is discussed. Firstly, a comparison of the measurements made with aluminum electrodes to those made with carbon electrodes enables an evaluation of the dose in aluminum to be done. Then a discussion of how to convert the carbon dose to tissue dose is presented. Table 3.10 gives the values of J/M extrapolated to zero pressure for the aluminum electrodes. The average peak to plateau ratio for aluminum is 1.435 ± 0.008 and the corresponding value for carbon (from table 3.5) is 1.490 ± 0.008. The difference between these two ratios indicates that there is a small difference in the kerma factor for these two materials.

Table 3.10: J/M Extrapolated to Zero Pressure for Aluminum Electrodes

| Gas | J/M peak (nC/g - DCI) | J/M plateau | Ratio |
|---|---|---|---|
| $CH_4$ | 1.706 | 1.178 | 1.448 |
| $CO_2$ | 1.045 | 0.725 | 1.441 |
| $N_2$ | 1.005 | 0.703 | 1.430 |
| $N_2O$ | 1.076 | 0.751 | 1.433 |
| $O_2$ | 1.130 | 0.790 | 1.430 |
| TE | 1.362 | 0.955 | 1.426 |
| air | 1.097 | 0.762 | 1.440 |

For the passing pions, muons and electrons, the dose in aluminum is related to the dose in carbon by the stopping power ratio

$$D^{Al}_{\pi,\mu,e} = \frac{S^{Al}_{\pi,\mu,e}}{S^{C}_{\pi,\mu,e}} D^{C}_{\pi,\mu,e} \qquad 3.12$$

For the case of stars due to stopped pions the relationship is

$$D^{Al}_{s} = F D^{C}_{s} = P K D^{C}_{s} \qquad 3.13$$

F is the kerma factor given by the product of P and K. The perturbation factor is $P = S^{Al}_{\pi}/S^{C}_{\pi}$. The ratio of the pion stopping density for aluminum/carbon is the same as the stopping power ratio. This is an approximate relationship which breaks down for very low energy pions stopping in thin gas targets because the stopping power ratio is no longer independent of energy. In such a case, $P = R_{wall}/R_{gas}$ as shown in section 2.3.1.3. The star energy factor is $K = k^{Al}/k^{C}$ where $k^{Al}$ is the energy released to charged secondaries per pion capture in aluminum plus that fraction of the energy released to all neutrons in the stopping field which is deposited at the point of interest. The charged secondaries and neutrons are handled differently because a field which has a diameter of 2 cm is large enough to provide an equilibrium spectrum of charged particles at its centre, but most of the energy given to neutrons will escape.

For the in-flight pion capture, the relevant equation is

$$D^{Al}_{i} = \frac{n^{Al}\,\sigma^{Al}_{\pi}}{n^{C}\,\sigma^{C}_{\pi}} \frac{k^{Al}}{k^{C}} D^{C}_{i} \qquad 3.14$$

where n is the number density of atoms and $\sigma_{\pi}$ is the cross sectional area for pion capture in flight. As a rough estimate, $\sigma$ is taken to be

proportional to the geometric cross section and therefore

$$\frac{n^{Al}\,\sigma_{\pi}^{Al}}{n^{C}\,\sigma_{\pi}^{C}} = \frac{\rho_{Al}}{\rho_{C}}\left(\frac{12}{27}\right)^{\frac{1}{3}} = 1.16$$

The total dose in aluminum at the peak is

$$D_T^{Al} = \left(\frac{J}{M}\right)_g^{Al} W_{\beta_g}\left(\overline{\frac{W}{W_\beta}\,r}\right)_g^{Al}$$

$$= D_e^{Al} + D_\mu^{Al} + D_\pi^{Al} + D_s^{Al}$$

$$= \left(\frac{J}{M}\right)_g^{C} W_{\beta_g}\left(\overline{\frac{W}{W_\beta}\,r}\right)_g^{C}\left(\frac{S_e^{Al}}{S_e^{C}}\,f_e^{C} + \frac{S_\mu^{Al}}{S_\mu^{C}}\,f_\mu^{C} + \frac{S_\pi^{Al}}{S_\pi^{C}}\,f_\pi^{C} + F_C^{Al}\,f_s^{C}\right) \qquad 3.15$$

where the superscript on $f_e^C$ refers to the fraction of the dose in carbon and the subscript refers to dose from electrons. Hence, the ionization per unit mass for aluminum electrodes divided by that for carbon electrodes is

$$\frac{(J/M)_g^{Al}}{(J/M)_g^{C}} = \frac{\left(\overline{\frac{W}{W_\beta}\,r}\right)_g^{C}}{\left(\overline{\frac{W}{W_\beta}\,r}\right)_g^{Al}}\left(\frac{S_e^{Al}}{S_e^{C}}\,f_e^{C} + \frac{S_\mu^{Al}}{S_\mu^{C}}\,f_\mu^{C} + \frac{S_\pi^{Al}}{S_\pi^{C}}\,f_\pi^{C} + F_C^{Al}\,f_s^{C}\right) \qquad 3.16$$

In order to find $F_C^{Al}$, it is necessary to evaluate

$$\left(\overline{\frac{W}{W_\beta}\,r}\right)_g^{Al} = \sum_i g_i^{Al,\,g}\left(\frac{W}{W_\beta}\right)_i^{Al,\,g} r_i^{Al,\,g} \qquad 3.17$$

For the passing pions, muons and electrons, the value of $g_i$ for aluminum is given by

$$g_i^{Al,\,g} = g_i^{C,\,g} \frac{(J/M)_T^{C,\,g}}{(J/M)_T^{Al,\,g}} \qquad 3.18$$

Since only the ionization due to stars is changing, this is simply a remormalization. For stars, g is given by

$$g_s^{Al,\,g} = 1 - g_\pi^{Al,\,g} - g_\mu^{Al,\,g} - g_e^{Al,\,g} \qquad 3.19$$

To complete the evaluation of equation 3.17, it is assumed that the change in secondary spectra from carbon to aluminum does not significantly alter $W/W_\beta$ and that, since $r_{gas}^{Carbon}$ for stars is not significantly different from the stopping power ratio, the value for $r_{gas}^{Aluminum}$ for stars is found by multiplying $r_{gas}^{Carbon}$ by the stopping power ratio $S_\pi^{Aluminum}/S_\pi^{Carbon}$. Then using values of $f_i^C$ from table 3.1, $g_i^C$ from tables 3.6 and 3.7, $\left(\overline{\frac{W}{W_\beta}\,r}\right)_g^C$ from table 3.9,

$$\frac{S_\mu^C}{S_\mu^{Al}} = \frac{S_\pi^C}{S_\pi^{Al}} = 1.14 \pm 0.01 \quad (80)$$

$$\frac{S_e^{Al}}{S_e^C} = 0.948 \pm 0.001 \quad (61)$$

and $$\frac{(J/M)_g^{Al}}{(J/M)_g^C} = \begin{matrix} 1.063 \pm 0.023 \ \text{(peak)} \\ 1.101 \pm 0.028 \ \text{(plateau)} \end{matrix} \quad \text{(tables 3.5 and 3.10)}$$

yields an average value of

$$\frac{\left(\overline{\frac{W}{W_\beta}\,r}\right)^{C}}{\left(\overline{\frac{W}{W_\beta}\,r}\right)^{Al}} = \begin{matrix} 1.128 \pm 0.008 \quad \text{(peak)} \\ 1.122 \pm 0.008 \quad \text{(plateau)} \end{matrix} \qquad 3.20$$

This error bar does not include the uncertainty introduced by the assumptions concerning $W/W_\beta$ and $r_s^{Al}$ above.

For the peak, the kerma factor for the dose due to stars is found by solving 3.16,

$$F_C^{Al} = 1.00 \pm 0.03$$

The error bar is smaller than anticipated because the values of $f_i$ are coupled. The star energy ratio for this field size is found from 3.13 as

$$K = \frac{k^{Al}}{k^{C}} = 1.14 \pm 0.03$$

The total dose in aluminum is given by

$$D_T^{Al} = D_T^{C}\left(\frac{1.063}{1.128}\right)$$

$$= 31.1 \quad \mu Gy/DCI$$

There is a 2.3% uncertainty for the value in brackets which, when added in quadrature with the 5.1% uncertainty in $D_T^C$ yields a total uncertainty for $D_T^{Al}$ of ± 5.5%. The values of

$$\left(\overline{\frac{W}{W_\beta}\,r}\right)_g^{Al} = \frac{D_T^{Al}}{\left(\frac{J}{M}\right)_g^{Al} W_{\beta_g}} \qquad 3.21$$

are found in table 3.11 and have an uncertainty of ± 4.6%.

A similar procedure carried out for the plateau gave

$$F_C^{Al} = \frac{n^{Al}\,\sigma_\pi^{Al}}{n^C\,\sigma_\pi^C}\,\frac{k^{Al}}{k^C} = 1.7 \pm 0.5$$

The error bar is large because of the uncertainty in the value $f_i$ for in-flight interaction. Using the value of $\frac{k^{Al}}{k^C}$ from above, $\frac{n^{Al}\,\sigma_\pi^{Al}}{n^C\,\sigma_\pi^C} = 1.5 \pm 0.5$ which is in agreement with the value 1.2 estimated above. The dose in the plateau is

$$D_T^{Al} = D_T^C \left(\frac{1.101}{1.122}\right) = 21.4 \ \mu Gy/DCI$$

with an estimated uncertainty of ± 5.9%. The values of $\left(\overline{\frac{W}{W_\beta}\,r}\right)_g^{Al}$ are calculated for the plateau according to equation 3.21 and displayed in table 3.11.

Table 3.11: Evaluation of $\overline{\frac{W}{W_\beta}\,r}$ for Aluminum Electrodes

| | Peak | Plateau |
|---|---|---|
| $CH_4$ | 0.673 | 0.672 |
| $CO_2$ | 0.907 | 0.902 |
| $N_2$ | 0.893 | 0.880 |
| $N_2O$ | 0.888 | 0.877 |
| $O_2$ | 0.893 | 0.880 |
| TE | 0.782 | 0.769 |
| air | 0.840 | 0.834 |

For a beam with no contamination, that is $f_e = f_\mu = 0$, then expression 3.20 becomes

$$\frac{\left(\overline{\frac{W}{W_\beta}\, r}\right)^{C}}{\left(\overline{\frac{W}{W_\beta}\, r}\right)^{Al}} = \frac{S_\pi^C}{S_\pi^{Al}}$$

and hence 3.16 simplifies to

$$\frac{(J/M)_g^{Al}}{(J/M)_g^{C}} = f_\pi^C + \frac{k^{Al}}{k^C} f_s^C \qquad 3.22$$

If the ratio of J/M values were experimentally extrapolated to zero field size in order to eliminate the dose due to neutrons, then solving 3.22 for $\frac{k^{Al}}{k^C}$ would give the ratio of the energy released to charged secondaries for pion capture in aluminum compared to carbon.

This completes the discussion of the determination of the dose in aluminum and of the kerma factor required to convert pion star dose in carbon to an equivalent dose in aluminum. Before discussing the conversion of dose in carbon to dose in tissue, a brief discussion of the measurements with TE-A150 plastic will be given.

Consider table 3.12 which indicates the values of J/M extrapolated to zero pressure for TE-A150 plastic electrodes. The peak to plateau ratio for TE plastic falls between the values for carbon and aluminum. As well, the ratios for ionization with TE-A150 plastic compared to carbon are not significantly different from unity: peak value 1.012 (TE gas) and 0.971 (air); plateau value 1.024 (TE gas) and 0.987 (air). Therefore,

the average energy made locally available per incident pion is about the same for TE-A150 plastic as for carbon. This equality arises in spite of the fact that TE-A150 plastic contains 7% oxygen for which a significantly lower energy release to charged secondaries than for carbon has been demonstrated. Consideration of the neutron dose and the other components of TE-A150 plastic may make up the deficit. Since $k^{TE-A150}/k^{C}$ is approximately unity, $F_{C}^{TE-A150}$ is approximately the stopping power ratio for TE-A150 plastic over carbon, and hence the dose in TE-A150 plastic is equal to the dose in carbon multiplied by the stopping power ratio.

The use of TE-A150 plastic for pion dosimetry is a questionable practice. Since it contains five elements, five times the measurements of charged particle spectra must be performed, or alternatively a special effort made to specifically measure the spectra for this material. Furthermore, since it is a mixture, the pion capture process may be difficult to determine due to the effects of mechanical variations (39, 38). This material is improperly labelled "tissue equivalent" for pions because it does not have the correct ratio of carbon to oxygen atoms. Without this special advantage of tissue equivalence there is no reason for its continued use in pion dosimetry.

Table 3.12: J/M Extrapolated to Zero Pressure for TE-A150 Electrodes

| | J/M peak (nC/g - DCI) | J/M Plateau | Ratio |
|---|---|---|---|
| TE | 1.296 | 0.884 | 1.466 |
| air | 0.975 | 0.666 | 1.464 |

The remaining problem to be discussed is how to convert the dose in carbon (or aluminum) to the dose in muscle. Equations 3.12, 3.13 and 3.14 need to be evaluated in order to do this. The crux of the problem is to assign a value to the quantity $k^{tissue}/k^{C}$. There are two aspects of this evaluation about which little is known: the contribution to the star dose by neutrons which may make this ratio field size dependent, and the total energy released to charged particles due to pion capture in tissue. There are two parts of the latter problem: lack of knowledge of the energy released to charged particles per pion capture on the elements composing tissue, and lack of knowledge of the capture process itself.

In order to provide an estimate of the conversion factor, consider tissue to contain only oxygen and carbon. The Z-law gives capture probabilities of 0.86 and 0.14 on oxygen and carbon respectively. Assume that star neutrons deposit 5.75 MeV/pion locally. This is 20% of the energy released to charged secondaries in the case of carbon and is typical of the value expected for the large field sizes required for therapy. Also assume that the same amount of energy is available from neutrons in the case of tissue. Then the star energy ratio is

$$\frac{k^{TE}}{k^{C}} = \frac{(28.77 \times 0.14) + (14.36 \times 0.86) + 5.75}{28.77 + 5.75} = 0.64$$

28.77 MeV and 14.36 MeV are the energies released per pion capture including that which goes to heavy undetected ions for carbon and oxygen respectively (see tables 2.1 and 2.2). The conversion factor for carbon to tissue is the same as for equation 3.15 with $S_e^{TE}/S_e^{C} = 1.12$ (61) and $S_\pi^{TE}/S_\pi^{C} = 1.11$ (80, 63):

$$1.12 \times 0.12 + 1.11 \times 0.42 + 1.11 \times 0.64 \times 0.46 = 0.93$$

By allowing the star energy for oxygen to vary within reasonable limits, the uncertainty was estimated to be ± 0.05.

This concludes the discussion of kerma. The absolute dose in tissue at the peak for this particular beam tune is 30.7 μGy/DCI with an uncertainty of ± 7.4%.

# CHAPTER 4

## CONCLUSION

In order to perform an absolute dose determination for the TRIUMF biomedical negative pion beam, an ionization chamber was used. The ionization in a carbon walled cavity was studied as a function of pressure both theoretically and experimentally. Because the secondaries released by pion capture have ranges of the order of the size of the cavity, the theory used was one which explicitly considers pion stars which originate within the cavity and pion secondaries which emerge from the walls with insufficient energy to cross the cavity. This calculation predicted that because pion capture on an oxygen nucleus yields less energy than capture on carbon, there would be a decrease in the ionization per unit mass as the pressure was increased for carbon dioxide filling, but not for methane. Qualitatively, this picture was confirmed by the experiment.

Due to the lack of quantitative agreement between the theory and experiment for the pressure dependence, the dose was determined by extrapolation of the ionization per unit mass to zero pressure. For this particular tune, the doses in carbon and aluminum are summarized in table 4.1. The error bar estimates the uncertainty of the accuracy. The error in precision is less than half of these values. Tables of factors were

determined to be able to convert an ionization reading to dose for carbon or aluminum walled chambers filled with a number of common gases.

Table 4.1: Dose in Carbon and Aluminum

| | Dose in Carbon $10^{-6}$ Gy/DCI | Dose in Aluminum $10^{-6}$ Gy/DCI |
|---|---|---|
| peak | 33.0 ± 1.7 | 31.1 ± 1.7 |
| plateau | 21.9 ± 1.2 | 21.4 ± 1.2 |

The kerma correction factor required to convert the dose, due to pion stars alone, in carbon to the dose in aluminum was estimated to be 1.00 ± 0.03 for the peak. An estimate of the kerma correction factor required to convert the dose, due to stars and contaminants, in carbon to the dose in tissue was 0.93 ± 0.05. In order to make an accurate evaluation of this factor, there is a need for a detailed knowledge of the pion capture process and for further experiments concerning the spectra of energetic secondaries emitted in pion stars in tissue.

Further dosimetry experiments are recommended in two areas. In order to investigate the non-Bragg-Gray nature of an ionization chamber, the ionization per unit mass should be studied as a function of cavity gap while keeping the pressure fixed. In this way, the Sternheimer density correction for the electron stopping power and the hypothesized dependence of the W-value on pressure would be eliminated. It is expected that the dependence of the ionization per unit mass on chamber size would be less dramatic than was its dependence on pressure.

The second area of needed research concerns the problem of sorting out the star dose into its charged particle and neutron fractions. A careful study of the ratio $k^{Al}/k^{C}$ as a function of field size may enable this to be done. This experiment could yield results more quickly by using a proportional counter which can operate in a time-of-flight mode. In one experiment the response could be studied as a function of field size with the chamber set to look at only those events coincident with pion arrival. The experiment could be repeated in an untimed mode. The timed mode is expected to show the largest change in $k^{Al}/k^{C}$ as the field size is varied.

Another area for research not directly related to dosimetry concerns the electron trapping mechanism for electronegative gases which was hypothesized to be responsible for an apparent increase in W-value with increased pressure. Such an effect would also cause pion trapping to be pressure dependent. It might be possible to use pionic X-rays to learn about the pion capture process and about the electron trapping process by studying gas mixtures containing an electronegative gas at varying pressure.

The understanding of pion dosimetry has been furthered by the work discussed here, but the field of pion dosimetry is still young and much work remains to be done. This thesis has attempted to focus on the principles of measurement. Perhaps in the next decade there will be further improvements in the charged particle spectra, capture probabilities, stopping power values and W-values to enable more accurate dosimetry to be performed.

REFERENCES


1. Fowler, P.H. and Perkins, D.H. The possibility of therapeutic applications of beams of negative π-mesons. Nature (London) 189, 524 (1961)

2. The Division of Cancer Research Resources and Centres, National Cancer Institute (U.S.). Committee for Radiation Oncology Studies Particle Proposal (Revised 10/78)

3. Barendsen, G.W. The importance of microdosimetry for radiation biology and radiation protection. in Proceedings of the First Symposium on Microdosimetry, ed. H.G. Ebert, pp. 1-26. Luxembourg: Euratom (1967)

4. Skarsgard, L.D. et al. Pre-clinical studies of the negative pi-meson beam at TRIUMF. Radiation and Environmental Biophysics (1979) (in press)

5. Shortt, K.R. and Henkelman, R.M. A charge collector to determine the stopping distribution of a pion beam. Phys. Med. Biol. 23, 495 (1978)

6. Skarsgard, L.D. et al. RBE measurements on the π-meson beam at TRIUMF. International Atomic Energy Agency Advisory Group Meeting on Clinical Applications of Particle Radiation and the Role of Radiosensitivity Modifiers, Vienna (1977)

7. U.S. Department of Commerce, National Bureau of Standards, Handbook 79, "Stopping powers for use with cavity chambers." (1961)

8. Bragg, W.H. The consequences of the corpuscular hypothesis of the γ and X-rays, and the range of β rays. Phil. Mag. 20, 385 (1910)

9. Gray, L.H. The absorption of penetrating radiation. Proc. Roy. Soc. (London) A122, 647 (1929)

10. Gray, L.H. An ionization method for the absolute measurement of γ-ray energy. Proc. Roy. Soc. (London) A156, 578 (1936)

11. Rubach, A.H. Calculation of neutron dose absorbed in spherical ionization chambers with finite cavity size. M.Sc. Thesis, University of Washington (1977)

12. Makarewicz, M. and Pszona, S. Theoretical characteristics of a graphite ionization chamber filled with carbon dioxide. Nucl. Inst. Meth. 153, 423 (1978)

13. Henry, M.I. Dose calculations relating to the use of negative pi-mesons for radiotherapy. M.Sc. Thesis, University of British Columbia (1973)

14. Guthrie, M.P., Alsmiller, R.G. and Bertini, H.W. Calculation of the capture of negative pions in light elements and comparison with experiments pertaining to cancer radiotherapy. Nucl. Inst. Meth. 66, 29 (1968)

15. Thwaites, D.I. and Watt, D.E. Similarity treatment of phase effects in stopping power for low energy heavy charged particles. Phys. Med. Biol. 23, 426 (1978)

16. Casewell, R.S. Deposition of energy by neutrons in spherical cavities. Radiation Research 27, 92 (1966)

17. Bichsel, H. and Rubach, A.H. Uncertainty of the determination of absolute neutron dose with ionization chambers. in Proceedings of the Third Symposium on Neutron Dosimetry in Biology and Medicine, ed. G. Burger, pp. 549-563. Luxembourg: Euratom (1977)

18. Fowler, P.H. and Mayes, V.M. The capture of $\pi^-$ mesons in oxygen and in other nuclei. Proc. Phys. Soc. 92, 377 (1967)

19. Larson, D.A., Carruth, R.T. and French, J.D. Investigation of charged secondaries emitted upon absorption of stopped $\pi$-mesons by carbon. Nucl. Inst. Meth. 100, 325 (1972)

20. Perry, D.R. Physical aspects of a radiobiological pion beam. Ph.D. Thesis, Surrey University and Rutherford Laboratory (1976)

21. Dey, W. et al. Measurements of neutrons and charged particles following $\pi^-$ absorption in nuclei. Helvetica Physica Acta 49, 778 (1976)

22. Comiso, J. et al. Measurement of the $\alpha$-particle spectrum resulting from $\pi^-$ capture in $^{12}C$. Phys. Rev. Letters 35, 13 (1975)

23. Perris, A.G., Smith, F.A. and Perry, D.R. Charged particle emission from the capture of negative pions: energy spectra, LET distribution and W-value. Phys. Med. Biol. 23, 217 (1978)

24. Mechtersheimer, G. et al. Measurement of energy spectra of charged particles emitted after the absorption of stopped negative pions in carbon. Phys. Letters 73B, 115 (1978)

25. Mechtersheimer, G. Measurement of the energy spectra of charged secondary particles from the absorption of stopped negative pions in carbon nuclei. Ph.D. Thesis, Karlsruhe University (1978)

26. Buche, G. et al. Measurements of energy spectra of charged particles emitted following the absorption of stopped pions in oxygen containing compounds and in calcium. SIN Newsletter 11 and to be published (1979)

27. Munchmeyer, D. Measurement of energy spectra and correlated charged secondary particles following the absorption of stopped negative pions in oxygen containing compounds. Ph.D. Thesis, Karlsruhe University (1979)

28. Comiso, J., Shlepuetz, F. and Ziock, K. An unfolding procedure for charged particle spectra and its application to the measurement of stopping power. Nucl. Inst. Meth. 133, 121 (1976)

29. Englehardt, H.D., Lewis, C.W. and Ullrich, H. The absorption of $\pi^-$ at rest on complex nuclei. Nucl. Phys. A258, 480 (1976)

30. Kluge, W. personal communication (1979)

31. Fermi, E. and Teller, E. The capture of negative mesotrons in matter. Phys. Rev. 72, 399 (1947)

32. Zinov, V.G., Konin, A.D. and Mukhin, A.I. Atomic capture of negative mesons in chemical compounds. Sov. J. Nucl. Phys. 2, 613 (1965)

33. Au-Yang, M.Y. and Cohen, M.L. Meson captures in solids. Phys. Rev. 174, 468 (1968)

34. Reidy, J.J., Hutson, R.L. and Springer, K. Use of muonic X-rays for tissue analysis. IEEE Trans. on Nucl. Sci. 22, 1780 (1975)

35. Ponomarev, L.I. Molecular structure effects on atomic and nuclear capture of mesons. in Proceedings of the 7th International Conference on High Energy Physics and Nuclear Structure, Zurich, p. 403 (1977) and Mesons in matter. Annual Review of Nuclear Science 23, 395 (1973)

36. Grin. G.A. and Kunselman, R. Solid state effects in pionic atoms. Phys. Lett. 31B, 116 (1976)

37. Tauscher, L. et al. Condensed-state effects in pionic and muonic X-ray spectra. Phys. Lett. 27A, 581 (1968)

38. Abazov, V.M. et al. Negative pion capture in heterogeneous mixtures of elements. Joint Institute for Nuclear Research (Dubna). E15-12013 (1978) submitted to Nuclear Instruments and Methods

39. Daniel, H. Calculation of the coulomb capture of mesonic particles in inhomogeneous matter. Nucl. Inst. Meth. 150, 609 (1978)

40. Barkas, W.H. et al. Range difference between $\pm$ $\pi$'s in emulsion. Proceedings of the 5th International Conference on Nuclear Photography at CERN. Volume II, Session 9, p. 1 (1965)

41. Andersen, H.H. and Ziegler, J.F. "Hydrogen stopping powers and ranges in all elements." Volume 3 of "The stopping and ranges of ions in matter." New York: Pergamon Press (1977)

42. Ziegler, J.F. "Helium: stopping powers and ranges in all elemental matter." Volume 4 of "The stopping and ranges of ions in matter." New York: Pergamon Press (1977)

43. Andersen, H.H. "Bibliography and index of experimental range and stopping power data." Volume 2 of "The stopping and ranges of ions in matter." New York: Pergamon Press (1977)

44. Santry, D.C. and Werner, R.D. Thickness measurements of thin foils using alpha particles from $^{148}Gd$ and $^{241}Am$. Nucl. Inst. Meth. 159, 523 (1979)

45. Santry, D.C. and Werner, R.D. Stopping powers for heavy ions in carbon over the energy region 200 to 2000 keV. IEEE Trans. on Nucl. Sci. 26, 1335 (1979)

46. Johansen, A., Steenstrup, S. and Wohlenberg, T. Energy loss of protons in thin films of carbon, aluminum and silver. Radiation Effects 8, 31 (1971)

47. Bernstein, W., Cole, A.J. and Wax, R.L. Penetration of 1-20 keV ions through thin carbon foils. Nucl. Inst. Meth. 90, 325 (1970)

48. Arkhipov, E. and Gott, Yu. Slowing down of 0.5-30 keV p in some materials. Soviet Physics JETP 29, 615 (1969)

49. Sautter, C.A. and Zimmerman, E.J. Stopping cross sections of carbon and hydrocarbon solids for low energy protons and helium ions. Phys. Rev. 140, 490 (1965)

50. Gorodetzky, S. et al. Mesure des pouvoirs d'arrêt de C, Ca, Au et $CaF_2$ pour des protons d'énergie comprise entre 0.4 et 6 MeV. Nucl. Phys. A91, 133 (1967)

51. Van Wijngaarden, A. and Duckworth, H.E. Energy loss in condensed matter of $^{1}H$ and $^{4}He$ in the energy range $4 < E < 30$ keV. Can. J. of Phys. 40, 1749 (1962)

52. Ormrod, J.H., MacDonald, J.R. and Duckworth, H.E. Some low energy atomic stopping cross sections. Can. J. of Phys. 43, 275 (1965)

53. Moorhead, R.D. Stopping cross section of low atomic number materials for $He^{+}$ 65-180 keV. J. of Applied Phys. 36, 391 (1965)

54. Fastrup, B., Hvelplund, P. and Sautter, C. Stopping cross section in carbon of .1 to 1.0 MeV atoms with $6 \leqslant Z_{1} \leqslant 20$. Det Konelige Danske Videnskabernes Selskab Matematisk-fysiske Meddelelser 35 #10, 1 (1966)

55. Dicello, J. LAMPF Progress Report LA-6819-PR p. 99 (1977)

56. Porat, D.I. and Ramavataram, K. Differential energy loss and ranges of Ne, N, and He ions. Proc. Phys. Soc. 78, 1135 (1961)

57. Matteson, S., Chau, E. and Powers, D. Stopping cross section of bulk graphite for α particles. Phys. Rev. A 14, 169 (1976)

58. Chu, W.K. and Powers, D. α particle stopping cross section in solids from 400 keV to 2 MeV. Phys. Rev. 187, 478 (1969)

59. Ormrod, J.H. and Duckworth, H.E. Stopping cross sections in carbon for low energy atoms with $Z \leqslant 12$. Can. J. of Phys. 41, 1424 (1963)

60. Krieger, G.L. et al. Relative determination of W-values for alpha particles in tissue equivalent and other gases. Phys. Med. Biol. 24, 286 (1979)

61. International Commission on Radiation Units and Measurements. ICRU Report 21, "Radiation dosimetry: electrons with initial energies between 1 and 50 MeV." Washington (1972)

62. Smith, A.R. et al. Dosimetry intercomparisons between fast neutron radiotherapy facilities. Med. Phys. 2, 195 (1975)

63. International Commission on Radiation Units and Measurements. ICRU Report 28, "Basic aspects of high energy particle interactions and radiation dosimetry." Washington (1978)

64. Bragg, W.H. and Kleeman, R. On the α particles of radium and their loss of range in passing through various atoms and molecules. Phil. Mag. 10, 318 (1905)

65. Williamson, J. and Watt, D.E. The influence of molecular binding on the stopping power of alpha particles in hydrocarbons. Phys. Med. Biol. 17, 486 (1972)

66. Feng, J.S.Y., Chu, W.K. and Nicolet, M.A. Bragg's rule in binary metal alloys and metal oxides for MeV $^4He^+$ ions. Thin Solid Films 19, 227 (1973)

67. Palmer, R.B.J. The stopping power of hydrogen and hydrocarbon vapours for alpha particles over the energy range 1 to 8 MeV. Proc. Phys. Soc. 87, 681 (1966)

68. Park, J.T. Stopping cross sections of some hydrocarbon gases for 40-200 keV helium ions. Phys. Rev. 138, A1317 (1965)

69. Rotondi, E. Bragg's additivity law of stopping power for 5 MeV α particles in $O_2$, $N_2$, $CO_2$, CO, $NH_3$ and hydrocarbon gases. National Research Council of Canada, NRC 9076 (1966)

70. Bourland, P. and Powers, D. Bragg-rule applicability to stopping cross sections of gases for α particles of energy .3 to 2 MeV. Phys. Rev. B 3, 3635 (1971)

71. Park, J.T. and Zimmerman, E.J. Stopping cross sections of some hydrocarbon gases for 40-250 keV protons and helium ions. Phys. Rev. 131, 1611 (1963)

72. Neuwirth, W. et al. Electronic stopping cross sections of elements and compounds for swift Li ions. Zeutschrift für Physik A275, 209 (1975)

73. Neuwirth, W. et al. On the invalidity of Bragg's rule in stopping cross sections of molecules for swift Li ions. Zeutschrift für Physik A275, 215 (1975)

74. Powers, D. et al. Molecular effects in energy loss of alpha particles in gaseous media. Thin Solid Films 19, 205 (1973)

75. Reynolds, H.K. et al. The stopping cross section of gases for protons, 30-600 keV. Phys. Rev. 92, 742 (1953)

76. Christophorou, L.G. "Atomic and molecular radiation physics." London: Wiley Interscience p. 34 (1971)

77. Swint, J.B., Prior, R.M. and Ramirez, J.J. Energy loss of protons in gases. Nucl. Inst. Meth. 80, 134 (1970)

78. Brolley, J.E. and Ribe, F.L. Energy loss by 8.86 MeV deuterons and 4.43 MeV protons. Phys. Rev. 98, 1112 (1955)

79. Phillips, J.A. The energy loss of low energy protons in some gases. Phys. Rev. 90, 532 (1953)

80. Bichsel, H. Charged-particle interactions. Chapter 4 of "Radiation dosimetry, Volume 1 Fundamentals," ed. F.H. Attix and W.C. Roesch. New York: Academic Press (1968)

81. Sullivan, A.H. "An ionization chamber for the direct measurement of dose equivalent." CERN 71-16 p. 415 (1971)

82. Hughes, S. The range of 5-50 keV heavy ions in various gases. Phys. Med. Biol. 12, 565 (1967)

83. Bourland, P., Chu, W. and Powers, D. Stopping cross sections of gases for $\alpha$ particles from .3 to 2 MeV. Phys. Rev. B 3, 3625 (1971)

84. Kerr, G.D. et al. Molecular stopping cross sections of air, $N_2$, Kr, $CO_2$ and $CH_4$ for alpha particles. Health Physics 12, 1475 (1966)

85. Rotondi, E. Energy loss of alpha particles in tissue. Radiation Research 33, 1 (1968)

86. Christophorou, L.G. "Atomic and molecular radiation physics." London: Wiley Interscience pp. 35-40 (1971)

87. Whillock, M.J. and Edwards, A.A. Determination of the stopping cross sections of $N_2$, $H_2$, $CH_4$, $C_4H_{10}$ and $C_3H_6$ using alpha particles in the range 1.3-4.2 MeV. Phys. Med. Biol. 24, 518 (1979)

88. Allison, S.K., Auton, D. and Morrison, R.A. Stopping power of gases for lithium ions. Phys. Rev. 138, A688 (1965)

89. Sidenius, G. Systematic stopping cross section measurements with low energy ions in gases. Det Kongelige Danske Videnskabernes Selskab Matematisk-fysiske Meddelelser 39 #4, 1 (1974)

90. Teplova, Ya. A. et al. Slowing down of multicharged ions in solids and gases. Soviet Physics JETP 15, 31 (1962)

106. Boag, J.W. and Seelentag, W.W. A general saturation curve for an ionization chamber filled with nitrogen at pressures up to 8 atmospheres. Phys. Med. Biol. 20, 624 (1975)

107. Varma, M.N. and Baum, J.W. Energy dependence of $\bar{W}$ for alpha particles in $N_2$, $CO_2$, $CH_4$, Ar, $H_2$ and Rossi-type tissue-equivalent gases. Phys. Med. Biol. 23, 1162 (1978)

108. Bortner, T.E. and Hurst, G.S. Ionization of pure gases and mixtures of gases by 5 MeV alpha particles. Phys. Rev. 93, 1236 (1954)

109. Kuhn, H. and Werba, T. Measurements of the energy expenditure for the production of an ion pair in tissue equivalent gas for heavy particles. in Proceedings of the Third Symposium on Neutron Dosimetry in Biology and Medicine, ed. G. Burger, pp. 85-96. Luxembourg: Euratom (1977)

110. Jesse, W.P. Alpha particle ionization in argon-methane mixtures and the energy dependence of the ion pair formation energy. Phys. Rev. 174, 173 (1968)

111. Rohrig, N. and Colvett, R.D. Measurements of $\bar{W}$ for protons, helium-4 ions and carbon ions in tissue equivalent gas. Brookhaven National Laboratory Report 23691 to be published in Radiation Research (1979)

112. Boring, J.W., Strohl, G.E. and Woods, F.R. Total ionization in nitrogen by heavy ions of energies 25 to 50 keV. Phys. Rev. 140, A1065 (1965)

113. Wapstra, A.H. and Bos, K. Atomic Data and Nuclear Data Tables 19, 177 (1977)

114. Whyte, G.N. Energy per ion pair for charged particles in gases. Radiation Research 18, 265 (1963)

115. Kellerer, A.M. Considerations on the random traversal of convex bodies and solutions for general cylinders. Radiation Research 47, 359 (1971)

116. Birkhoff, R.D. et al. The determination of LET spectra from energy proportional pulse height measurements. I: Track length distributions in cavities. Health Physics 18, 1 (1970)

117. Sternheimer, R.M. and Peierls, R.F. General expression for the density effect for the ionization loss of charged particles. Phys. Rev. B 3, 3681 (1971)

118. Kim, Y.S. Density effect in dE/dx of fast charged particles traversing various biological materials. Radiation Research 56, 21 (1973)

119. Schillaci, M. and Roeder, D. Dose distribution due to n and $\gamma$ resulting from $\pi^-$ capture in tissue. Phys. Med. Biol. 18, 821 (1973)

91. Christophorou, L.G. "Atomic and molecular radiation physics." London: Wiley Interscience p. 492-500 (1971)

92. Ziegler, J.F. personal communication concerning "Heavy ions: stopping powers and ranges." Volume 5 of "The stopping and ranges of ions in matter." New York: Pergamon Press to be published (1979)

93. Högberg, G. Electronic and nuclear stopping cross sections in carbon for light mass ions of 4.5 to 46 keV energy. Phys. Stat. Sol. (b) 48, 829 (1971)

94. Pivovar, L.I., Nikolaichuk, L.I. and Rashkovan, V.M. Passage of lithium ions through condensed targets. Soviet Physics JETP 20, 825 (1965)

95. Bernhard, F. et al. Stopping cross sections of $Li^+$ ions with energies from 30 to 100 keV in various target materials. Phys. Stat. Sol. 35, 285 (1969)

96. Stocker, H. and Berkowitz, E.H. Atomic charge state ratios of $^6Li$ ions from 5.8-16.4 MeV. Can. J. of Phys. 49, 480 (1971)

97. Marion, J.B. and Young, F.C. "Nuclear reaction analysis graphs and tables." Amsterdam: North Holland (1968)

98. MacDonald, J.R. and Sidenius, G. The total ionization in methane of ions with $1 \leqslant z \leqslant 22$ at energies from 10 to 120 keV. Phys. Lett. 28A, 543 (1969)

99. Dennis, J.A. Computed ionization and kerma values in neutron irradiated gases. Phys. Med. Biol. 18, 379 (1973)

100. Turner, J.E., Wright, H.A. and Hamm, R.N. Estimated W-values for negative pions in $N_2$ and Ar. Health Phys. 29, 792 (1975)

101. Turner, J.E. et al. Estimated W-values for negative pions in tissue-equivalent gas, $CO_2$ and $N_2$. Health Physics 32, 300 (1977)

102. Delafield, H.J. and Harrison, K.G. Ionization measurements and the derivation of $W_n$ in acetylene and carbon dioxide irradiated with neutrons. Phys. Med. Biol. 24, 271 (1979)

103. Edwards, A.A. and Dennis, J.A. The calculation of charged particle fluence and LET spectra for the irradiation of biologically significant materials by neutrons. Phys. Med. Biol. 20, 395 (1975)

104. Loosemore, W.R. and Knill, G. The collection efficiency of a mean current fission ionisation chamber. Atomic Energy Research Establishment at Harwell Report AERE-R3677 (1961)

105. Dennis, J.A. and Edwards, A.A. National Radiological Protection Board Report M20 (1975)

120. Brenner, D.J. and Smith, F.A. Dose and LET distributions due to n and $\gamma$ emitted from stopped $\pi^-$. Phys. Med. Biol. 22, 451 (1977)

121. Lang, H. and Harrison, R.W. The biomedical beam line control system at TRIUMF. TRIUMF Report TRI-I-75-2 (1975)

122. Henkelman, R.M. et al. Tuning of the biomedical negative pion beam line at TRIUMF. Nucl. Inst. Meth. 155, 317 (1978)

123. Poon, M.N.C. Optimization studies of the TRIUMF biomedical pion beam. M.Sc. Thesis, University of British Columbia (1977)

124. Skarsgard, L.D. et al. Physical and radiobiological properties of the negative pi-meson beam at TRIUMF. IAEA-SM-212/65 (1977)

125. Nordell, B. et al. Determination of some parameters for pion radiobiology studies. Phys. Med. Biol. 22, 466 (1977)

126. Turner, J.E. et al. The computation of pion depth dose curves in water and comparison with experiment. Radiation Research 52, 229 (1972)

127. Alsmiller, R.G., Barish, J. and Dodge, S.R. Energy deposition by high energy electrons (50 to 200 MeV) in water. Preprint ORNL-TM-4419 (1974)

128. Ito, A. and Henkelman, R.M. Microdosimetry of the pion beam at TRIUMF. submitted to Radiation Research (1979)

129. Goodman, L. Density and composition uniformity of A-150 tissue-equivalent plastic. Phys. Med. Biol. 23, 753 (1978)

130. Personal communication with Canadian Stackpole regarding graphite grade SR-30

131. Personal communication with Wilkinson regarding aluminum grade Alcan 2S #1100

132. American Institute of Physics Handbook, ed. D.E. Gray. New York: McGraw-Hill (1972)

133. Boag, J.W. Ionization chambers. Chapter 1 of "Radiation dosimetry, Volume II Instrumentation," ed. F.H. Attix and W.C. Roesch. New York: Academic Press (1966)

134. Jaffé, G. Zur Theorie der Ionisation in Kolonnen I. Annalen der Physik 42, 303 (1913)

135. Xanstra, H. A short method for determining the saturation current according to Jaffé's theory of column ionisation. AERE-TRANS 876 translator J.B. Sykes (1961)

136. Delafield, H.J. personal communication (1978)

137. Mustafa, S.M. and Mahesh, K. Criterion for determining saturation current in parallel plate ionization chambers. Nucl. Inst. Meth. 150, 549 (1978)

138. International Commission on Radiation Units and Measurements. ICRU Report 16, "Linear Energy Transfer." Washington (1970)

139. Lam, G.K.Y., Henkelman, R.M. and Harrison, R.W. An automated dose mapping system for the TRIUMF biomedical pion beam. Phys. Med. Biol. 23, 768 (1978)

140. Klein, U. Measurement of neutrons emitted following the absorption of stopped negative pions in the biologically relevant nuclei $^{12}C$, $^{14}N$ and $^{16}O$. Ph.D. Thesis, Karlsruhe University (1978)

DO NOT COPY

APPENDIX A:

PHYS. MED. BIOL., 1978, Vol. 23, No. 3, 495–498. Printed in Great Britain

*Scientific Note*

# A Charge Collector to Determine the Stopping Distribution of a Pion Beam

K. R. SHORTT, M.SC. and R. M. HENKELMAN, PH.D.

Batho Biomedical Facility, TRIUMF, University of British Columbia, Vancouver, Canada V6T 1W5

*Received* 31 *October* 1977, *in final form* 15 *December* 1977

## 1. Introduction

Because of the variation in quality throughout the radiation field produced by a beam of negative $\pi$ mesons, the specification of the field by dose alone is not adequate for a determination of the biological effectiveness of the radiation. Microdosimetric measurements of various types have been used to provide supplementary information about the quality of pion radiation fields (Lucas, Quam and Raju 1969, Amols, Dicello and Lane 1976, Richman 1976). It is anticipated that such measurements will be useful for the prediction of the variable biological effectiveness of the pion radiation.

In a pion radiation field most of the densely ionising radiation is generated by the charged secondary particles from the pion stars and by the pions at the extreme ends of their tracks. The energy from the charged-particle secondaries is deposited close to the pion star; 50% within 0·3 mm of the star (Henry 1973). It is therefore expected that the spatial distribution of the densely ionising component of a pion radiation field will be well represented by the spatial distribution of the pion stars. We have therefore investigated the use of a charge collector as a means of measuring the depth distribution of pion stars.

## 2. The detectors and measurements

Charge collectors have been used to measure the net charge deposition pattern in electron beams (Laughlin 1965, Van Dyk and MacDonald 1972). A detector of the type used by Van Dyk and MacDonald (1972) is shown in fig. 1. It consists of a polystyrene disc 100 mm in diameter by 1 mm thick which is coated with Aquadag and connected to the central lead of a coaxial cable. The complete assembly is covered with a close fitting 1 mm thick polystyrene insulator which is itself coated with Aquadag and connected to the sheath of the coaxial cable. The complete assembly is housed in a polystyrene water-proof housing. Charge which is deposited in the inner collector or out to a thickness half way through the 1 mm insulating layer will either leak to the innermost Aquadag surface or will induce a charge of opposite sign onto that surface and thus, in either case, produce a current of one unit charge on the

0031-9155/78/0003-0495 $01.00 © 1978 The Institute of Physics

DO NOT COPY



central lead of the coaxial cable. This geometry results in an effective collection volume of 101 mm diameter by 2 mm thick.

The detector was suspended in a water phantom by a remote controlled three-dimensional scanner. Measurements at shallow depths were made in air with various thickness of polystyrene absorber in front of the charge collector. The depths in polystyrene were converted to the equivalent depths in water

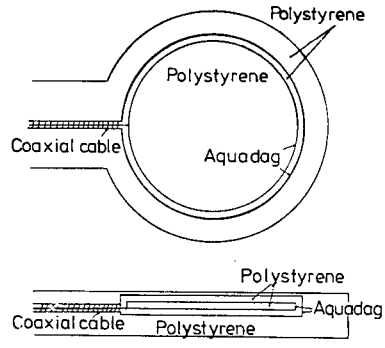


Fig. 1. The construction of the polystyrene charge collector showing the two conducting layers and the cable connections.

using density and stopping power corrections. The detector was irradiated in the TRIUMF biomedical pion beam (Harrison and Lobb 1973, Henkelman, Skarsgard, Lam, Harrison and Palcic 1977) with a 148 MeV/$c$ beam which was composed by number of 50% pions, 10% muons and 40% electrons. The momentum acceptance of the beam was measured to be $\pm 7\%$ $\Delta p/p$ FWHM. The beam had lateral dimensions of 4 cm × 4 cm FWHM and so was completely intercepted by the charge collector. The flux of the incident beam was monitored with a transmission ionisation chamber which had been calibrated to measure particle flux at low flux rates. The experiment was performed using an incident flux of $10^7$ particles $s^{-1}$.

The charge from the collector was integrated using a Keithley Model 610C electrometer. The electrometer was zeroed to give a null reading when the beam was off. Multiple readings were made at each depth and the mean and standard error were calculated.

### 3. Results

The amount of charge collected per incident particle as a function of the effective depth in water to the centre of the collector is shown in fig. 2. The error bars are the standard deviations of 10 measurements. A subsequent experiment showed a similar distribution of measured values. The measurements show a collection of positive charge at depths which are less than 1 cm corresponding to the knock out of negative electrons from the medium by the incident pions. The mean energy of δ-rays from fast pions is expected to be of the order of 1 MeV.

There is then little net charge deposition until a depth of 10 cm where a net deposition of negative charge is observed extending to approximately 17 cm. This corresponds to the charge deposited by the stopping pions. The solid curve in fig. 2 is a differential range curve measured with a plastic scintillator range telescope at low beam intensity for the same pion beam tune. The differential range curve is arbitrarily normalised and the baseline is adjusted to

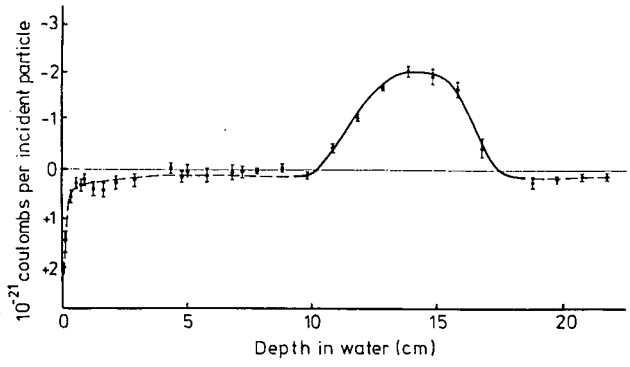


Fig. 2. The net charge collected as a function of depth in a phantom irradiated in the pion beam. The solid curve is a differential range curve measured for the same tune which has been scaled to pass through the data. Data points are shown with standard errors of the mean.

match the charge collection curve. However, the agreement in shape and range between the two measurements confirms that the charge collector is measuring the pion stopping distribution. Furthermore, the area under this stopping peak above the interpolated background corresponds to $-0{\cdot}9 \pm 0{\cdot}2$ elementary charges per stopping pion.

The net collection of positive charge before and after the stopping peak may not be significant. The dashed line which has been drawn through the data points has no statistical significance. In the region between 1 and 10 cm in depth there will be deposition of negative charge by in flight capture of pions and depletion of negative charge by the knock out of secondary electrons by the incident 148 MeV electrons of the beam. Delta rays from these high energy electrons could have ranges comparable to the dimensions of the phantom. Depending on the relative magnitude of these two effects, a net charge collected of either sign could be explained. Since very few of the electrons are expected to stop in a range of up to 25 cm, they are not generally detected by this type of measurement.

## 4. Discussion

It has been possible using a charge collector to measure the stopping distribution of negative pions even in the presence of a large electron contamination. It is anticipated that measurements made in a pion beam with low electron contamination would show a reduced background which would in turn improve the ability to localise the pion stars even where the stopping distribution is

DO NOT COPY



extended in depth. An electron knock on region at shallow depths has also been detected, although it is unlikely that this will correspond to any significant dose build-up since most of the entrance dose is directly deposited by the incident charged particles. It is anticipated that the ability to measure the stopping distribution in high intensity pion beams will provide another means of characterising the high LET component of the pion radiation field and thus be of predictive value for biological isoeffect.

We wish to thank Dr. J. C. F. MacDonald for the loan of the charge collector used in this experiment.

K. R. S. is a research student of the National Cancer Institute of Canada.

## References

Amols, H., Dicello, J., and Lane, T., 1976, in *Proc. Fifth Symp. on Midrodosimetry*, EUR5452 d–e–f (Euratom) pp. 911–928.

Harrison, R. W., and Lobb, D. E., 1973, *IEEE Trans. Nucl. Sci.*, **NS-20**, 1029–1031.

Henkelman, R. M., Skarsgard, L. D., Lam, K. Y., Harrison, R. W., and Palcic, B., 1977, *Int. J. Radiat. Oncol. Biol. Phys.*, **2**, 123–127.

Henry, M. I., 1973, *M.Sc. Thesis*, University of British Columbia.

Laughlin, J. S., 1965, in *Symp. on High-energy Electrons, Montreux*, Ed. A. Zuppinger and G. Poretti (Berlin: Springer-Verlag) pp. 11–16.

Lucas, A. C., Quam, W. M., and Raju, M., 1969, *EG & G Technical Paper* No. S–54–TP.

Richman, C., 1976, *Radiat. Res.*, **66**, 453–471.

Van Dyk, J., and MacDonald, J. C. F., 1972, *Radiat. Res.* **50**, 20–32.

## APPENDIX B: DEFINITIONS OF QUANTITIES, EQUATIONS AND CONSISTENCY CHECKS

This appendix is a collection of various terms and relationships required by the calculation discussed in chapter 2.

stopping power:

$$S(\varepsilon) = \frac{d\varepsilon}{\rho dx} \quad \text{with units MeV-cm}^2/\text{g}$$

range:

$$R(E) = \int_0^E \frac{1}{S(\varepsilon)} \, d\varepsilon \quad \text{with units g/cm}^2$$

production spectrum:

$$Np(E) = \Pi \; Kp(\varepsilon) \quad \text{with units} \quad \frac{\text{secondaries}}{\text{MeV-g}}$$

where $\Pi$ is the pion stopping density with units pion stops/g and $K_p(\varepsilon)$ is the number of secondaries per pion stop with energy between $\varepsilon$ and $\varepsilon + d\varepsilon$ with units $\frac{\text{secondaries}}{\text{pion stop-MeV}}$

slowing down spectrum:
(equilibrium spectrum)

$$Nr(E) = \frac{1}{S(E)} \int_{\varepsilon=E}^{E_{max}} Np(\varepsilon) \, d\varepsilon \quad \text{with units} \quad \frac{\text{secondaries}}{\text{MeV-cm}^2}$$

The total number of secondaries crossing unit area is given by

$$\int_{E=0}^{\varepsilon_m} Nr(E) \, dE = \int_{E=0}^{\varepsilon_m} R(\varepsilon) \; Np(\varepsilon) \, d\varepsilon$$

Check #1 tests the value of the ratio of these two integrals, R, and is found in column 5 of table B.1.

Bragg-Gray integral:

$$BG = \int_0^{\varepsilon_{max}} S(E)\ Nr(E)\ dE \quad \text{with units MeV/g}$$

For an infinitesimal cavity, the dose deposited is given by the stopping power of the cavity medium averaged over the spectrum of secondaries crossing the cavity from the wall. If the cavity is filled with wall, that is it has the same spectrum of secondaries and same stopping power as the wall, then Fano's theorem concludes that the dose deposited in all cavities regardless of their size or pressure is the same as given by the Bragg-Gray integral, or alternatively, the kerma. Check #2 tests the ratio $D_{total}/K$ and is found in column 6 of table B.1. The total dose in column 3 is the mean over eight different areal densities and the fact that the rms deviation is small is another test of check #2.

kerma:

$$K = \int_0^{\varepsilon_{max}} \varepsilon\ Np(\varepsilon)\ d\varepsilon \quad \text{with units MeV/g}$$

In the calculation, kerma has been restricted to the energy deposited by charged secondaries released by the pion-nucleus interaction. In this case, kerma is the value of the dose that would be deposited at the centre of a large block of material which is exposed to a stopping density of 1 pion/g where K MeV are released per pion stop. The total dose in the slowing down spectrum is given by the Bragg-Gray integral which equals the kerma for wall filling the cavity. Check #3 tests the ratio BG/K and is found in column 7 of table B.1.

Table B.1 illustrates the result of the calculation for a spherical cavity containing wall material. The averages are taken over eight different areal densities increasing by factors of two from 2.44 mg/cm$^2$ to 312 mg/cm$^2$. This is equivalent to a 2 cm diameter sphere when filled with carbon dioxide at pressures between 0.25 and 32 (x100 kPa).

Table B.1: Checks of Internal Consistency

| Secondary | Kerma (MeV/g) | Total Dose (MeV/g) | BG Integral (MeV/g) | #1 R (%) | #2 $D_{total}/K$ (%) | #3 BG/K (%) |
|---|---|---|---|---|---|---|
| P | 10.505 | 10.501 ± .004 | 10.544 ± .006 | -.00 | -.04 | .38 |
| d | 6.383 | 6.379 ± .002 | 6.411 ± .006 | .01 | -.06 | .43 |
| t | 3.074 | 3.071 ± .001 | 3.091 ± .006 | .05 | -.10 | .56 |
| $He^3$ | .640 | 0.638 ± .001 | 0.643 ± .002 | .15 | -.22 | .44 |
| $He^4$ | 5.510 | 5.491 ± .009 | 5.525 ± .013 | .26 | -.35 | .26 |
| Li | 1.337 | 1.330 ± .005 | 1.338 ± .002 | .28 | -.56 | .09 |

The table indicates that systematic errors are less than ½% and are therefore negligible.

## APPENDIX C: EXTRACTION OF OXYGEN SPECTRA

The secondary spectra for pion capture in oxygen can be extracted from the data for mylar and acetate which exhibit different capture ratios for carbon to oxygen. Independent measurement of the secondary spectra for carbon led to the adoption of the following extraction procedure for oxygen.

For each particle type and each energy, let the true yields be $a_C$, $a_O$, $a_A$ and $a_M$ for capture on carbon, oxygen, acetate and mylar respectively. Let the measured yields be

$$b_C = a_C + \alpha \quad \text{for carbon} \tag{C.1}$$

$$b_A = a_A + \beta \quad \text{for acetate} \tag{C.2}$$

$$\text{and} \quad b_M = a_M + \gamma \quad \text{for mylar} \tag{C.3}$$

where $\alpha$, $\beta$, and $\gamma$ are errors in the measurement. Since the capture ratio (carbon: oxygen) is 1.1:1 for acetate and 1.7:1 for mylar (27),

$$1.1\, a_C + 1.0\, a_O = 2.1\, a_A \tag{C.4}$$

$$\text{and} \quad 1.7\, a_C + 1.0\, a_O = 2.7\, a_M \tag{C.5}$$

$$\text{Eliminating } a_O, \quad 2.1\, a_A - 1.1\, a_C = 2.7\, a_M - 1.7\, a_C \tag{C.6}$$

Substituting C.1, C.2 and C.3 into C.6 and rearranging gives

$$D = 0.6\, b_C + 2.1\, b_A - 2.7\, b_M = 0.6\, \alpha + 2.1\, \beta - 2.7\, \gamma$$

Minimizing the sum of the squares of the errors ($\alpha$, $\beta$, and $\gamma$) is achieved by assigning

$$\alpha = \frac{0.6\, D}{(0.6)^2 + (2.1)^2 + (2.7)^2}$$

and so on. Then $a_O$ can be obtained from either C.4 or C.5 as

$$a_O = 2.1\,(b_A - \beta) - 1.1\,(b_C - \alpha) \tag{C.7}$$

$$\text{or} \quad a_O = 2.7\,(b_M - \gamma) - 1.7\,(b_C - \alpha) \tag{C.8}$$

The values obtained for the yields from carbon by this extraction procedure were approximately 1% higher than the values measured in the experiment by Mechtersheimer (25). Therefore, both the carbon and oxygen yields as extracted by the above procedure were normalized by this ratio to maintain consistency with the carbon data which had been used extensively in earlier calculations.

## APPENDIX D: STERNHEIMER DENSITY CORRECTION TO THE STOPPING POWER OF ELECTRONS

The calculation of the Sternheimer density correction is based on reference (117) and the notation is from reference (118). The Bethe-Bloch formula for electrons is given by:

$$\frac{dE}{dx} = \frac{0.1535}{(v/c)^2} \left\langle \frac{Z}{A} \right\rangle \left[ \ell n\{(2\tau + 4)m^2\} + F - \delta - 2\, \ell n \langle I \rangle + 27.631 \right]$$

$m$ = .511 MeV/$c^2$

$v$ = electron speed

$c$ = photon speed

$\tau$ = reduced kinetic energy = $T/M$

$\left\langle \frac{Z}{A} \right\rangle = \sum_{i=1} W_i\, Z_i/A_i$ where $W_i$ is the fractional weight of the $i^{th}$ element

$$F = \text{kinematics term} = 1 - (v/c)^2 + 2\, \ell n(\tau/2) + \frac{\frac{\tau^2}{8} - (2\tau + 1)\, \ell n 2}{(\tau + 1)^2}$$

$\langle I \rangle$ = adjusted mean excitation energy (eV) given by

$$\ell n \langle I \rangle = \left( \sum_i W_i \frac{Z_i}{A_i} \ell n\, I_i \right) \Big/ \left\langle \frac{Z}{A} \right\rangle$$

$\delta$ = density correction = $4.606\, X + C$

$X = \log_{10} (\beta/(1 - \beta^2)^{\frac{1}{2}}) = \log_{10} (P/MC)$

$C = -2\, \ell n\{ \langle I \rangle / (28.804 \sqrt{\rho \langle Z/A \rangle}) \} - 1$

$\rho$ = density ($g/cm^3$)

Values of I for hydrogen, carbon and oxygen were taken to be 18.7, 78.0 and 89.0 eV respectively (138).

Table D.1: Parameters Required to Calculate the Density Correction

| Parameter | Carbon Dioxide | Methane | Carbon |
|---|---|---|---|
| $\langle Z/A \rangle$ | 1/2 | 5/8 | 1/2 |
| log $\langle I \rangle$ | 4.453 | 3.785 | 4.357 |
| $\langle I \rangle$ (eV) | 85.85 | 44.05 | 78.0 |
| $\rho$ (g/cm$^3$) at 1 atmosphere and 22% C | $1.8296 \times 10^{-3}$ | $.6633 \times 10^{-3}$ | 1.77 |

Electrons of momentum 180 MeV/c, have kinetic energy of 179.5 MeV and a range in water of roughly 93 cm (61). In the plateau (depth $\sim$15 cm) the residual energy is about 150 MeV and in the peak (depth $\sim$ 22 cm) it is about 130 MeV. Using this to evaluate $\tau$, F and X gives

$$\frac{dE}{dx} = .1535 \langle Z/A \rangle \left[K - \delta - 2 \ell n \langle I \rangle\right]$$

and $$\delta = 4.606\, X - 2\, \ell n\{ \langle I \rangle / (28.804 \sqrt{\rho \langle Z/A \rangle}\,)\} - 1$$

where K = 42.350 and X = 2.407 in the peak

and K = 42.778 and X = 2.469 in the plateau.

This has been used to calculate the stopping powers shown below.

Table D.2: Electron Stopping Powers ($MeV\text{-}cm^2/g$)

| Pressure (atmospheres) | Carbon Dioxide | | Methane | |
|---|---|---|---|---|
| | Peak | Plateau | Peak | Plateau |
| 0 | 2.566 | 2.599 | 3.336 | 3.377 |
| 1 | 2.496 | 2.508 | 3.196 | 3.210 |
| 2 | 2.443 | 2.454 | 3.130 | 3.144 |
| 4 | 2.390 | 2.401 | 3.063 | 3.077 |
| 8 | 2.337 | 2.348 | 2.997 | 3.011 |

These can be converted to stopping power ratios with respect to carbon by noting that the stopping powers for carbon in the peak and plateau are 1.970 and 1.981 $MeV\text{-}cm^2/g$ respectively.